# A Study of Charm Production by Neutrinos in the NOMAD-STAR Detector

Malcolm Ellis

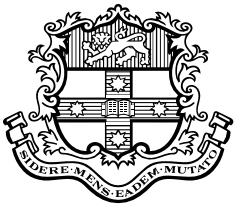


*A thesis*
*submitted for the degree of*
*Doctor of Philosophy*
*at the*
*University of Sydney*

March, 2001

# Abstract

The NOMAD neutrino experiment at the CERN SPS is described and the silicon tracking detector (STAR) that was placed in NOMAD is discussed in detail.

An algorithm for the reconstruction of hits, tracks and vertices with the silicon tracker and utilising the Kalman filter method was developed and is also described.

The vertex position resolution is determined to be $19\mu m$ in the Y direction and $78\mu m$ in the Z direction from Monte Carlo.

The impact parameter resolution of STAR is determined to be $28\mu m$.

From the sample of charged current neutrino interactions, a search is performed for the production and decay of $D^0, D^+, D_S^+, D^{0^*}$ and $D^{+^*}$ mesons.

From this analysis, the masses and lifetimes of the D mesons and resonances are determined to be:

$$\begin{aligned} m_{D^0} &= 1.875 \pm 0.075\text{GeV} \\ < c\tau_{D^0} > &= 145^{+39}_{-25}\mu m \\ m_{D^+} &= 1.880 \pm 0.088\text{GeV} \\ < c\tau_{D^+} > &= 213^{+183}_{-67}\mu m \\ m_{D_s^+} &= 1.973 \pm 0.061\text{GeV} \\ < c\tau_{D_s^+} > &= 199^{+132}_{-56}\mu m \\ m_{D^{0*}} &= 1.973 \pm 0.046\text{GeV} \\ m_{D^{+*}} &= 2.072 \pm 0.031\text{GeV} \end{aligned}$$

The production rates (R) per $\nu_\mu$ charged current deep inelastic interaction of D mesons are determined to be:

$$\begin{aligned} R(D^0) &= 4.2 \pm 2.0\% \\ R(D^+) &= 2.4 \pm 1.3\% \\ R(D_s^+) &= 0.64 \pm 0.36\% \\ R(D^{0^*}) &= 3.3 \pm 6.2\% \\ R(D^{+^*}) &= 1.7 \pm 2.6\% \end{aligned}$$

The inclusive production rate of charmed mesons is determined to be $7.2 \pm 2.4$ %.

# Acknowledgements

It has been my privilege to work with many wonderful people during the course of this project. Firstly, my supervisors, Professor Lawrence Peak and Dr Paul Soler, who made me welcome to the Falkiner High Energy Physics Department as an undergraduate summer student and have helped, encouraged and supported me ever since. Although not one of my supervisors, Dr Kevin Varvell was always available for assistance and discussions on any number of topics, from neutrino physics to the mysteries of the NOMAD collaboration.

While in Sydney, I was lucky to be working within an energetic and friendly department that included Drs Andy Bakich, Grant Gorfine, Reza Hashemi-Nezhad and Juris Ulrichs.

There are many people at CERN who I would like to thank. Firstly Dr Juan Jose Gomez-Cadenas for welcoming me to the STAR group and for his encouragement, support and sense of humour. Dr Valentin Kouznetsov introduced me to the beginnings of the STAR reconstruction and it was a pleasure to work with him, even with the missing " 's "! I would like to thank Anselmo Cervera-Villanueva for his friendship and assistance with the Kalman Filter.

I would particularly like to thank Jukka Kokkonen, who has worked with me on STAR since I first arrived and who introduced me to many delights including the secret life of Reindeer and the "international language" to name but two!

Both at CERN and in Sydney, I was fortunate to spend time with many friendly students. Andrew Godley and Joe Seisdedos were officemates and friends who were always available for a chat, help or mischief. Bruce Canu, Aldo Saavedra and Jaime Varas provided regular distractions and entertainment.

I must also thank Drs Steven Boyd and Bruce Yabsley, former Falkiner students who were both extremely helpful.

# Author's Contribution

The construction, survey and installation of the STAR detector was carried out by the STAR collaboration [14].

The analysis of the data collected in the survey was performed by the author and Dr F.J.P Soler.

The algorithm used for the reconstruction of silicon hits was devised in [1] and implemented by the author.

The Kalman track filter for STAR was devised by members of the STAR collaboration (including the author) and implemented by the author.

The definition and implementation of the Kalman vertex fit was the sole responsibility of the author.

The modifications to the Monte Carlo event generator to incorporate STAR were made by the author with assistance from Drs Steven Boyd and Bruce Yabsley.

The calculation of the neutrino spectrum at STAR was made using data provided by Andrew Godley.

The implementation of STAR in the Monte Carlo was performed by Jukka Kokkonen, the author used this program to produce all the Monte Carlo used in this analysis.

The extraction (or filtering) of good neutrino interactions in STAR from the NOMAD data was performed by the author.

The modification of the NOMAD event display program "matchgraph" to include the STAR detector and reconstructed hits, tracks and vertices was performed by the author.

The charm analysis was the sole responsibility of the author.

# Contents

# List of Figures

# List of Tables

# Chapter 1

# Theory and Motivation

## 1.1 Introduction

On the most fundamental level, matter is thought to consist of two types of particles, leptons and quarks (see Table 1.1). The four forces through which interactions can take place are the electromagnetic, weak, strong and gravitational (See Table 1.2). Particles "feel" a force through the exchange of mediating particles called bosons. The boson mediating the electromagnetic force is the photon. The gravitational force only dominates on cosmological scales and is thus neglected in high-energy physics. Only the quarks see the strong force which binds them into either baryons of three quarks (such as the proton and neutron) or mesons which are quark anti-quark pairs (such as pions and kaons). Particles with a charge can interact through the electromagnetic force. Both quarks and leptons can interact via the weak force which is responsible for $\beta$-decay.

In 1967-1968 Weinberg and Salam proposed a theory to unify the weak and electromagnetic interactions [38]. This model started with the SU(2) group of weak isospin and a U(1) group called the weak hypercharge. Invoking a process called spontaneous symmetry breaking, they gave three of the bosons ($W^+, W^-$ and $Z^0$) mass leaving one (the photon) massless. The interaction energy, represented by the Lagrangian energy density $\mathcal{L}$ is:

$$\mathcal{L} = \frac{g}{\sqrt{2}}(J_\mu^- W_\mu^+ + J_\mu^+ W_\mu^-) + \frac{g}{\cos\theta_W}(J_\mu^{(3)} - \sin^2\theta_W J_\mu^{em}) + g\sin\theta_W J_\mu^{em} A_\mu \quad (1.1)$$

The first term describes the weak charged current, the second term the weak neutral current and the final term the electromagnetic neutral current. The coupling of the electromagnetic interaction is known to be $e$, the electric

| Quarks | | |
|---|---|---|
| Flavour | Electric Charge (e) | Mass (MeV/$c^2$) |
| Up (u) | +2/3 | $\approx 4$ |
| Down (d) | -1/3 | $\approx 7$ |
| Charm (c) | +2/3 | $\approx 1,500$ |
| Strange (s) | -1/3 | $\approx 200$ |
| Top (t) | +2/3 | $\approx 180,000$ |
| Bottom (b) | -1/3 | $\approx 4,700$ |
| Leptons | | |
| Flavour | Electric Charge (e) | Mass (MeV/$c^2$) |
| e-neutrino ($\nu_e$) | 0 | $< 0.000003$ |
| Electron (e) | -1 | 0.511 |
| $\mu$-neutrino ($\nu_\mu$) | 0 | $< 0.19$ |
| Muon ($\mu$ ) | -1 | 105 |
| $\tau$-neutrino ($\nu_\tau$) | 0 | $< 18.2$ |
| Tau ($\tau$) | -1 | 1777 |

Table 1.1: Properties of the Quarks and Leptons

| Interaction | Relative Strength | Mediator | Range (m) |
|---|---|---|---|
| strong | 1 | gluon | $\leq 10^{-15}$ |
| electromagnetic | $10^{-2}$ | photon | $\infty$ |
| weak | $10^{-5}$ | $Z^0$ and $W^{\pm}$ | $10^{-18}$ |
| gravity | $10^{-42}$ | graviton | $\infty$ |

Table 1.2: Properties of the Gauge Bosons

charge of the positron, so from equation 1.1 the coupling of the electromagnetic interaction compared to that of the weak interaction is:

$$e = g \sin \theta_W \tag{1.2}$$

In the Standard Model, the quark mass eigenstates are not the same as the weak eigenstates. The matrix relating these bases was defined and parameterised by Kobayashi and Maskawa [32] in 1973. The conventional description leaves the three charge $\frac{2}{3}$ quarks (up, charm and top) unmixed and the mixing is expressed in terms of a $3 \times 3$ unitary matrix operating on the $-\frac{1}{3}$ quarks (down,strange and bottom).

$$\begin{pmatrix} d' \\ s' \\ b' \end{pmatrix} = \begin{pmatrix} V_{ud} & V_{us} & V_{ub} \\ V_{cd} & V_{cs} & V_{cb} \\ V_{td} & V_{ts} & V_{tb} \end{pmatrix} \begin{pmatrix} d \\ s \\ b \end{pmatrix} \tag{1.3}$$

The 90% confidence limits on each of these elements are currently determined ( [32]) to be:

$$\begin{pmatrix} 0.9742 - 0.9757 & 0.219 - 0.226 & 0.002 - 0.005 \\ 0.219 - 0.225 & 0.9734 - 0.9749 & 0.037 - 0.043 \\ 0.004 - 0.014 & 0.035 - 0.043 & 0.9990 - 0.9993 \end{pmatrix} \tag{1.4}$$

There are currently three main areas under study, to find predictions made by the Standard Model or evidence for physics beyond the Standard Model.

- **Higgs Boson :** The Higgs mechanism has been suggested as the means by which fundamental particles acquire a mass. The Large Hadron Collider at CERN will, when completed in 2005, allow a search for the Higgs Boson predicted by this theory.

- **CP Violation :** The symmetries C (particle/anti-particle exchange) and P (inversion of all three axes) have been found to hold for all strong and electromagnetic interactions. Large C and P violations have been discovered in weak interactions, however, so it was suggested that the product CP (that is the operation of C followed by the operation of P) would be a good symmetry. In 1964, CP violation was discovered in the decay of the $K^0$. This asymmetry may explain why the matter and anti-matter in the very early universe did not completely annihilate. Several different experiments are currently looking for further evidence of CP violation in the decay of B mesons.

- **Neutrino Oscillations :** In the Standard Model, the masses of the neutrinos are assumed to be exactly zero, however, there is growing evidence to suggest that this is not the case. If neutrinos do possess some small mass, then it can be shown that a neutrino of one type, after travelling some distance, may "oscillate" into a different flavour. This will be discussed in more detail in Section 1.6.

## 1.2 Neutrino-Nucleon Scattering

Neutrinos hold a special place in the Standard Model. Being neutral leptons, they only experience the weak interaction. A common method of studying the structure of hadrons is through the interactions of neutrinos in a fixed target.

In section 1.1 it was shown that the electro-weak Lagrangian allows for two different neutrino interactions, the charged and neutral current.

The charged current interaction involves the exchange of a $W^{\pm}$ boson and the resultant transformation of the incoming neutrino into the charged lepton from the same generation.

$$\nu_\mu + N \longrightarrow \mu^- + X \tag{1.5}$$

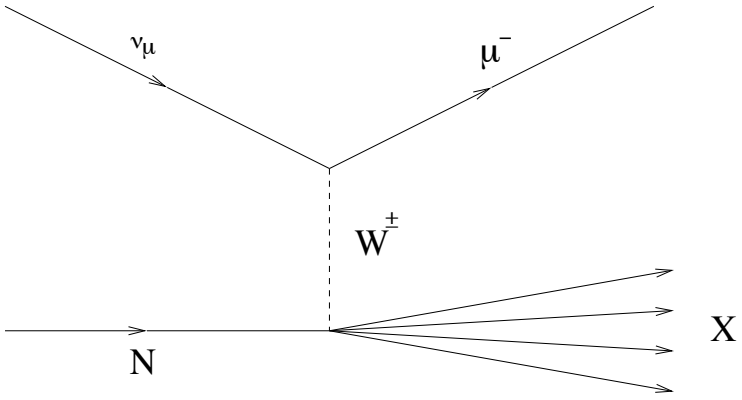


Figure 1.1: A $\nu_\mu$ Charged Current Interaction

In the neutral current, a $Z^0$ boson is exchanged (see Figure 1.2).

$$\nu_\mu + N \longrightarrow \nu_\mu + X \tag{1.6}$$

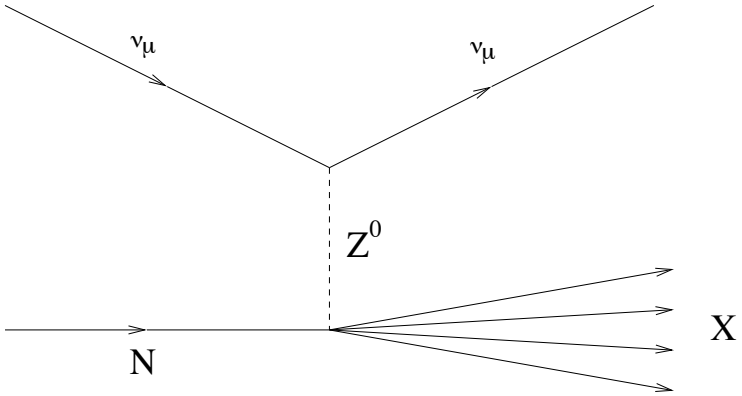


Figure 1.2: A $\nu_\mu$ Neutral Current Interaction

For the purposes of the analysis described in this thesis, we will assume that the event involves the interaction of a muon neutrino. In the following discussion, natural units are used, for which

$$c = \hbar = 1 \tag{1.7}$$

Figure 1.3 shows the lowest order Feynman diagram of the neutrino-nucleon scattering process. In the diagram $k^\mu$ and $l^\mu$ are the four-momenta of the incoming neutrino and outgoing lepton respectively, $q^\mu$ is the four-momentum transferred to the hadronic system, $P^\mu$ is the 4-momentum of the nucleon, $x$ is Bjorken x (see below) and $W^\mu$ is the four momentum of the outgoing hadronic system.

Measurement of these 4-vectors allows the determination of all the kinematic quantities of the $\nu_\mu - \mathrm{N}$ scattering process:

The square of the energy in the centre of mass is a Lorentz invariant quantity which can be calculated from the energy of the neutrino and the assumption that the neutrino scatters off a nucleon.

$$s = (k + P)^2 = 2M_N E_\nu + M_N^2 \approx 2M_N E_\nu \tag{1.8}$$

The nucleon mass has only been retained to first order and the calculation of the dot-product $(k + P)^2$ has been carried out in the laboratory frame.

The energy transferred from the neutrino to the hadronic system is given the symbol $\nu$:

$$\nu = \frac{P \cdot q}{M} = \mathrm{E}_\nu - \mathrm{E}_\mu \quad \text{(in the laboratory frame.)} \tag{1.9}$$

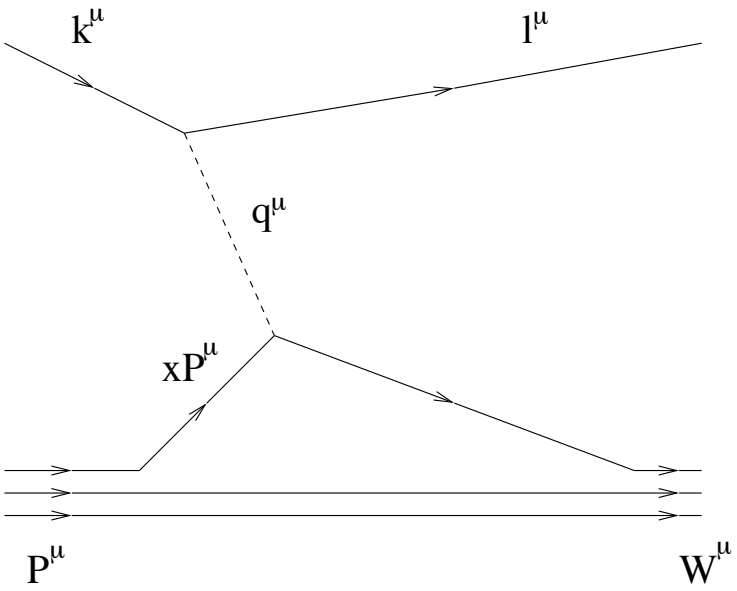


Figure 1.3: Definitions of kinematic variables in neutrino-nucleon deep-inelastic scattering

The square of the 4-momentum that is transferred to the hadronic jet can be calculated from the energy of the outgoing muon $E_l$ and the angle $\theta$ between the incoming neutrino and the outgoing muon.

$$-q^2 = Q^2 = -(k-l)^2 = 2\left(E_l E_\nu - |p_l| E_\nu cos\theta\right) - m_l^2 \tag{1.10}$$

Neglecting the mass of the muon, the energy of the lepton can be approximated by the measured momentum of the muon and the expression can be simplified to:

$$Q^2 = 4E_\nu E_l sin^2\left(\frac{\theta}{2}\right) \tag{1.11}$$

The Bjorken variable $x_{Bj}$ measures the fraction of the total nucleon momentum that was carried by the quark that was struck by the neutrino.

$$x_{Bj} = \frac{Q^2}{2P \cdot q} = \frac{Q^2}{2M_N \nu} \tag{1.12}$$

The Bjorken variable $y_{Bj}$ measures the degree of inelasticity of the interaction.

$$y_{Bj} = \frac{P \cdot q}{P \cdot k} \tag{1.13}$$

In the laboratory frame this can be expressed as:

$$y_{Bj} = \frac{\nu}{E_\nu} \tag{1.14}$$

The square of the invariant mass of the hadronic system can be determined from:

$$W^2 = (q + P)^2 = M_N^2 + Q^2 \left( \frac{1}{x_{Bj}} - 1 \right) \tag{1.15}$$

## 1.3 The Charged Current Interaction

The inclusive cross section for neutrino-nucleon scattering may be expressed as

$$\frac{d^2\sigma^{\nu(\overline{\nu})\mathcal{N}}}{d\Omega_\mu dE_\mu} = \frac{G_F^2}{(2\pi)^2} \left( \frac{M_W^2}{M_W^2 + Q^2} \right)^2 \frac{E_\mu}{E_\nu} L_{\mu\nu} W^{\mu\nu} \tag{1.16}$$

In this expression $G_F$ is the Fermi constant and $M_W$ is the mass of the W boson. $E_\nu$ is the energy of the neutrino and $E_\mu$ is the energy of the muon. The solid angle element into which the muon scatters is represented by $\mathrm{d}\Omega_\mu$.

It is possible to calculate the lepton tensor:

$$L^{\mu\nu} = k^\mu k'^\nu - g^{\mu\nu} k \cdot k' + k'^\mu k^\nu \pm i\epsilon^{\mu\nu\rho\sigma} k_\rho k'_\sigma \tag{1.17}$$

The last term is positive for neutrino interactions and negative for anti-neutrinos.

In [5] it was shown that the tensor $\mathrm{W}^{\mu\nu}$, which describes the interaction between the nucleon and the W boson, cannot be determined analytically. It was shown, however, that the term could be expressed in terms of the 4-vectors $P^\mu$, $E_\nu$ and $q^\mu$ and that the resulting differential cross-section could then be expressed in terms of the quantities which were defined in Equations 1.8-1.13.

$$\frac{d^2\sigma^{\nu(\overline{\nu})\mathcal{N}}}{dxdy} = \frac{G^2 M E_\nu}{\pi}\left(\frac{M_W^2}{M_W^2+Q^2}\right)^2\Bigg\{2x\frac{y^2}{2}F_1^{\nu(\overline{\nu})}(x,Q^2)+ F_2^{\nu(\overline{\nu})}(x,Q^2)\left(1-y-\frac{Mxy}{2E_\nu}\right) \pm xF_3^{\nu(\overline{\nu})}(x,Q^2)y\left(1-\frac{y}{2}\right)\Bigg\} \quad (1.18)$$

It would seem that Equation 1.18 contains twelve structure functions, three for each of the possible interactions of neutrinos or anti-neutrinos with protons and neutrons in the target material.

This number can be significantly reduced by using a model of the structure of the target nucleon known as the Quark-Parton Model which is the basis for Quantum Chromo Dynamics (QCD).

## 1.4 The Quark-Parton Model

When using QCD, we assume that the incoming neutrino scatters incoherently off point-like partons within the nucleon. These partons are the spin-$\frac{1}{2}$ quarks introduced in Table 1.1. A proton would consist of a $(UUD)$ configuration of "valence" quarks and the neutron consists of $(UDD)$. There is also a continuum of "sea" quarks which are just $q\overline{q}$ pairs in the nucleon.

Under the assumption that the neutrino is scattering off spin $\frac{1}{2}$ constituents of the target nucleon, the ratio between $F_1$ and $F_2$ in the scaling region (high $Q^2$) is determined to be:

$$\frac{2xF_1(x)}{F_2(x)} = 1 \quad (1.19)$$

This relationship is known as the Callan-Gross relationship and has been verified experimentally [38].

In order to visualise the neutrino-quark interaction, it is convenient to operate in the so-called "infinite momentum" frame in which the nucleon 3-momentum is very large and so the masses of the quarks and leptons as well as the Fermi motion are neglected.

When operating in the infinite momentum frame, the transverse momentum of the quarks in the struck nucleon are essentially zero and so the neutrino scatters off only one quark leaving the other "spectator" quarks untouched.

As quarks are not allowed to be free, the struck quark must recombine with the spectator quarks after the collision. It is assumed that this process occurs over a time scale which is significantly greater than that of the neutrino-quark interaction.

The predictions made by this model have been tested and found to be in good agreement with experiment.

In order to calculate the rates of different neutrino-quark scattering processes, the quark and anti-quark probability densities are written in terms of the individual densities for each quark flavour. These densities as a function of the fraction of the nucleon momentum carried by the quark ($x$) are denoted by $u(x)$, $d(x)$, $s(x)$ and $c(x)$ for the up, down, strange and charm quarks.

Using these defintions, the momentum distributions for neutrino and anti-neutrino scattering off a proton can be written in terms of the densities defined above:

$$\begin{aligned} xq^{\nu P}(x) &= xd^P(x) + xs^P(x) \\ x\overline{q}^{\nu P}(x) &= x\overline{u}^P(x) + x\overline{c}^P(x) \\ xq^{\overline{\nu} P}(x) &= xu^P(x) + xc^P(x) \\ x\overline{q}^{\overline{\nu} P}(x) &= x\overline{d}^P(x) + x\overline{s}^P(x) \end{aligned} \tag{1.20}$$

where the $\nu(\overline{\nu})$ superscripts refer to the quark or antiquark content seen by a neutrino (antineutrino) probe.

It is possible to assume that the sea quark momentum distributions are the same as those for the sea antiquarks as they are produced as particle anti-particle pairs. Also, according to isospin symmetry between the proton and neutron:

$$u^P = d^N \tag{1.21}$$

$$d^P = u^N \tag{1.22}$$

The distributions for neutron scattering can therefore be determined from those for the proton:

$$\begin{aligned} xq^{\nu N}(x) &= xu^P(x) + xs^P(x) \\ x\overline{q}^{\nu N}(x) &= x\overline{d}^P(x) + x\overline{c}^P(x) \\ xq^{\overline{\nu} N}(x) &= xd^P(x) + xc^P(x) \\ x\overline{q}^{\overline{\nu} N}(x) &= x\overline{u}^P(x) + x\overline{s}^P(x) \end{aligned} \tag{1.23}$$

It is now possible to express the differential cross section for neutrino scattering in terms of the quark and anti-quark momentum distributions.

$$\frac{d^2\sigma^{\nu P(N)}}{dxdy} = \frac{2G^2ME_\nu}{\pi}\left(\frac{M_W^2}{M_W^2+Q^2}\right)^2\left[\left((1-y)^2-\frac{Mxy}{2E_\nu}\right)x\overline{q}^{P(N)}(x) + \left(1-\frac{Mxy}{2E_\nu}\right)xq^{P(N)}(x)\right] \quad (1.24)$$

The target used in this thesis contained a slight excess of neutrons over protons, so the cross-section must be weighted according to the relative quantities of neutrons and protons:

$$\frac{d^2\sigma^{\nu(\overline{\nu})}}{dxdy} = \frac{1}{Z+N}\left(Z\frac{d^2\sigma^{\nu(\overline{\nu})P}}{dxdy} + N\frac{d^2\sigma^{\nu(\overline{\nu})N}}{dxdy}\right) \quad (1.25)$$

where Z is the number of protons and N the number of neutrons in the target.

## 1.5 Charm Quark Production

In the first approximation, charm production by neutrino deep inelastic scattering is a special case of Equation 1.24.

According to the Standard Model, the presence of a charm quark in the final state requires that the struck quark be a $d$ or an $s$ quark. In neutrino interactions this implies that the structure functions take the form

$$F_2^{\nu P} = xF_3^{\nu P} = x(|V_{cd}|^2 d(x) + |V_{cs}|^2 s(x)) \quad (1.26)$$

where the Cabibbo flavour mixing has been made explicit by the inclusion of the Cabibbo-Kobayashi-Maskawa (CKM) matrix elements $|V_{cd}|$ and $|V_{cs}|$. Inserting these structure functions into Equation 1.24 and assuming an isoscalar target, massless charm quarks and neglecting the mass of the proton the double differential cross section for charm production is :

$$\frac{d^2\sigma^{\nu P}}{dxdy} = \frac{G^2ME_\nu}{\pi}\left(\frac{M_W^2}{M_W^2+Q^2}\right)^2\left[|V_{cd}|^2(xd(x)+xu(x)) + 2|V_{cs}|^2 xs(x)\right] \quad (1.27)$$

If charm quarks were massless this would be the final cross section. However, the correct inclusion of massive quark effects introduces complications into the treatment outlined above. At leading order in QCD, the mechanism used to account for heavy quark effects is referred to as "slow rescaling".

The slow rescaling mechanism was developed by Georgi and Politzer [37] in order to present a correct account of kinematic effects arising from non-negligible masses in perturbative QCD. Their proposition was that the structure functions do not scale with $x_{Bj}$ but rather with

$$\xi = \frac{Q'^2}{2M_p\nu}\left(\frac{2}{1+\sqrt{(1+Q'^2/\nu^2)}}\right) \tag{1.28}$$

where

$$2Q'^2 = Q^2 + m_F^2 - m_I^2 + \sqrt{\left(Q^4 + 2Q^2(m_F^2+m_I^2) + (m_F^2-m_I^2)^2\right)} \tag{1.29}$$

The struck quark mass is $m_I$, the produced quark is $m_F$, the proton mass is $M_p$ and $Q^2$ and $\nu$ have been introduced in Section 1.2. In the case of charm production $m_I$ can be set to zero and so, in the limit that $Q^2 \gg M_p$, Equation 1.28 reduces to

$$\xi = x + \frac{m_F^2}{2M_p\nu} \tag{1.30}$$

It is also possible to come to the same result by looking at the momentum of the W boson and that momentum carried by the struck quark and requiring energy and momentum conservation, one obtains:

$$(\xi P + q)^2 = m_F^2 \tag{1.31}$$

When Equation 1.31 is expanded one finds that

$$\begin{aligned}\xi &= -\frac{\nu}{M_p}\left(1-\sqrt{\left(1+\frac{Q^2+m_F^2}{\nu^2}\right)}\right)\\ &\approx \frac{Q^2}{2M_p\nu} + \frac{m_F^2}{2M_p\nu}\\ &= x + \frac{m_F^2}{2M_p\nu}\end{aligned} \tag{1.32}$$

and so, in the case of heavy quark production, Equation 1.28 may be seen as arising from 4-momentum conservation at the quark-boson vertex.

Slow rescaling may now be used to introduce the proper treatment of the charm quark mass threshold into the charm production cross section. The

procedure mainly consists of replacing $x$ by $\xi$ in the structure functions and parton densities,

$$\begin{aligned} F_2(x,Q^2) &\longrightarrow F_2(\xi,Q^2) \\ xF_3(x,Q^2) &\longrightarrow \frac{x}{\xi}\xi F_3(\xi,Q^2) \end{aligned} \tag{1.33}$$

These are inserted into the charged current cross section to yield

$$\begin{aligned} \frac{d^2\sigma^{\nu(\overline{\nu})\mathcal{N}}}{dxdy} = \frac{G^2 M E_\nu}{\pi}\left(\frac{M_W^2}{M_W^2+Q^2}\right)^2 \Bigg\{ \frac{2x}{2\xi}\frac{y^2}{2} 2\xi F_1^{\nu(\overline{\nu})\mathcal{N}}(\xi,Q^2) + \\ F_2^{\nu(\overline{\nu})\mathcal{N}}(\xi,Q^2)\left(1-y-\frac{Mxy}{2E_\nu}\right) \pm \frac{x}{\xi}\xi F_3^{\nu(\overline{\nu})\mathcal{N}}(\xi,Q^2) y\left(1-\frac{y}{2}\right)\Bigg\} \end{aligned} \tag{1.34}$$

Writing the structure functions as linear combinations of the quark densities as before and changing variables from $(x,Q^2)$ to $(\xi,Q^2)$ allows the charm production cross section to be expressed as

$$\begin{aligned} \frac{d^2\sigma^{\nu\mathcal{N}}}{d\xi dy} = \frac{G^2 M E_\nu \xi}{\pi}\left[\left(u(\xi,Q^2)+d(\xi,Q^2)\right)|V_{cd}|^2 + 2s(\xi,Q^2)|V_{cs}|^2\right] \\ \left(1-y+\frac{xy}{\xi}+\Gamma(1-y-\frac{Mxy}{2E_\nu})-\frac{Mxy}{2E_\nu}\right) \end{aligned} \tag{1.35}$$

for neutrino interactions and

$$\begin{aligned} \frac{d^2\sigma^{\overline{\nu}\mathcal{N}}}{d\xi dy} = \frac{G^2 M E_\nu \xi}{\pi}\left[\left(\overline{u}(\xi,Q^2)+\overline{d}(\xi,Q^2)\right)|V_{cd}|^2 + 2\overline{s}(\xi,Q^2)|V_{cs}|^2\right] \\ \left(1-y+\frac{xy}{\xi}+\Gamma(1-y-\frac{Mxy}{2E_\nu})-\frac{Mxy}{2E_\nu}\right) \end{aligned} \tag{1.36}$$

for antineutrino events.

In Equations 1.35 and 1.36 the variable $\Gamma$ is introduced to take the exact Callan-Gross relationship into account and is written as

$$\Gamma = \left(\frac{1+R}{1+\frac{4M^2\xi^2}{Q^2}}\right) - 1 \tag{1.37}$$

where $R$ is defined as the ratio of the longitudinal to transverse W boson absorption cross sections.

Kinematic limits for $\xi$ and $y$ may be derived from the requirement that $Q^2$ be greater than zero and that the invariant hadronic mass, $W^2$, be larger than the square of the sum of the charm mass and the nucleon mass :

$$\begin{aligned} Q^2 &> 0 \\ W^2 &> (m_c + M_N)^2 \end{aligned} \tag{1.38}$$

These limits are

$$\begin{aligned} \frac{m_c^2}{2ME_\nu} &\leq \xi \leq 1 \\ \frac{(m_c+M)^2 - M^2}{2ME_\nu} &\leq y \leq 1 \end{aligned} \tag{1.39}$$

## 1.6 Neutrino Oscillations

As mentioned in the Introduction, neutrino oscillations are the most promising method of determining if neutrinos have non zero mass.

If we assume that the states of neutrinos that are detected, $|\nu_\alpha\rangle$ where $\alpha = e, \mu, \tau$, only have definite flavour, but not mass, then due to mixing, they must be superpositions of some other mass eigenstates $|\nu_i\rangle$. The neutrino flavour eigenstates may then be expressed:

$$|\nu_\alpha\rangle = \sum_i U_{\alpha i} \ |\nu_i\rangle \tag{1.40}$$

where $U_{\alpha i}$ is a $3 \times 3$ unitary mixing matrix.

In order to see the "oscillation", it is necessary to follow the time evolution of the neutrino eigenstates:

$$|\nu_\alpha(t)\rangle = \sum_i e^{i(\vec{p}_i\vec{x} - E_i t)} U_{\alpha i} \, |\nu_i\rangle \tag{1.41}$$

At a later time, the relative mixtures of the 3 mass eigenstates may be different, and thus the flavour state observed if the neutrino is observed through an interaction may have oscillated.The probability that the neutrino has oscillated from flavour $\alpha$ into flavour $\beta$ at some time $t$ is therefore given by:

$$P(\nu_\alpha \to \nu_\beta) = |\langle \nu_\beta | \nu_\alpha(t) \rangle|^2 \tag{1.42}$$

$$= |\sum_i e^{i(\vec{p}_i\vec{x} - E_i t)} U_{\alpha i} U^*_{i\beta}|^2 \tag{1.43}$$

$$= \sum_i \sum_j U_{\alpha i} U^*_{\beta i} U^*_{\alpha j} U_{\beta j} \ e^{i(\vec{p}_i - \vec{p}_j)\vec{x}} e^{-i(E_i - E_j)t} \tag{1.44}$$

This can be simplified using $\langle \nu_i | \nu_j \rangle = \delta_{ij}$. Given current upper limits on neutrino masses, it is safe to also assume that the neutrinos are relativistic, and therefore $|\vec{p}| \gg m_i$ hence:

$$E_i = \sqrt{p^2 + m_i^2} \;\approx\; p + \frac{m_i^2}{2p} \;\approx\; p + \frac{m_i^2}{2E} \tag{1.45}$$

Substituting this approximation into equation 1.44, and choosing the x-axis for the direction of propagation of the neutrino gives:

$$P(\nu_\alpha \to \nu_\beta) \;=\; \sum_i \sum_j U_{\alpha i} U^*_{\beta i} U^*_{\alpha j} U_{\beta j}\; e^{-i\frac{\Delta m^2_{ij}}{2E}t} \tag{1.46}$$

where $\Delta m^2_{ij} = m^2_i - m^2_j$ is the difference between the squares of the mass eigenvalues of the two mass eigenstates. It can be seen, therefore, that it is necessary for the neutrino mass eigenstates to have different eigenvalues before oscillations can occur. It is for this reason that experimental evidence for neutrino oscillation would demonstrate a massive neutrino as at least one neutrino would have to have a non-zero mass for this mass difference to occur.

A simplification that is often used in order to appreciate the characteristics of neutrino oscillations and to make predictions for a particular experimental arrangement is that of two neutrino mixing. This reduces the mixing matrix to:

$$U = U^* = \begin{pmatrix} \cos\theta & \sin\theta \\ -\sin\theta & \cos\theta \end{pmatrix} \tag{1.47}$$

where $\theta$ is the mixing angle and determines the degree to which the flavour states are mixtures of the mass states. Equation 1.46 can then be expressed:

$$P(\nu_1 \to \nu_2) = \sin^2(2\theta)\;\sin^2\left(\frac{\Delta m^2_{21} t}{4E}\right) \tag{1.48}$$

If we then use $L = ct$ and define $L_{osc}$:

$$L_{osc} \;\equiv\; \frac{4\pi E}{\Delta m^2_{21}} \;=\; \frac{2.48(E/\mathrm{GeV})}{(\Delta m^2_{21}/eV^2)}[km] \tag{1.49}$$

the probability can be found in terms of the distance the neutrino has travelled:

$$P(\nu_1 \to \nu_2) = \sin^2(2\theta)\;\sin^2\left(\frac{\pi L}{L_{osc}}\right) \tag{1.50}$$

It can be seen that $L_{osc}$ is the length at which the oscillation probability returns to zero. Depending on the value of $L$ compared to that of $L_{osc}$, the observed oscillation will range between a prominent oscillation and an

apparent absence as the oscillations become so quick that they average to a half.

When a search is conducted for neutrino oscillations, it is described in terms of a region of the $\Delta m^2$ versus $sin^2(2\theta)$ phase space. The region that can be probed by a given experiment is determined by the average energy of the neutrino beam and the distance between neutrino source and the detector.

If no signal is observed, an exclusion plot can be calculated showing the region in phase space covered by the experiment.

An exclusion plot for $\nu_\mu \longrightarrow \nu_\tau$ oscillation determined by the NOMAD experiment as well as that for $\nu_e \longrightarrow \nu_\tau$ is shown in figure 1.4.

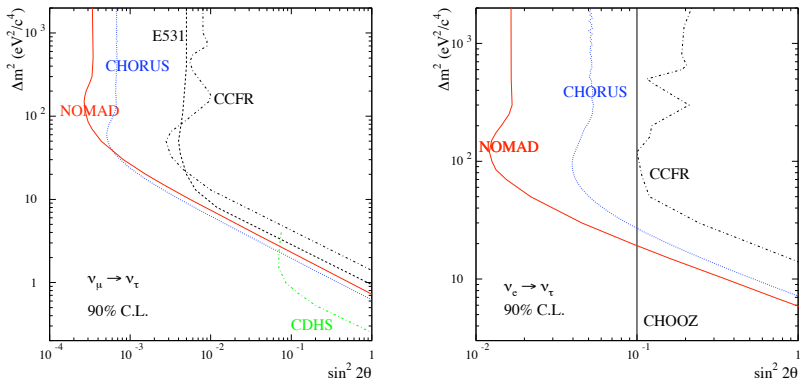


(a) $\nu_\mu \longrightarrow \nu_\tau$ Oscillation (b) $\nu_e \longrightarrow \nu_\tau$ Oscillation

Figure 1.4: NOMAD exclusion plots for $\nu_\mu \longrightarrow \nu_\tau$ [3] and $\nu_e \longrightarrow \nu_\tau$ [4] oscillations

If, however neutrino oscillations are observed, then given the known beam energy and distance a region in phase space can be identified for the two particular flavours of neutrinos involved.

The Super Kamiokande experiment [51] has observed an up-down assymetry in the observed rates of muon neutrinos. It has been suggested that this is due to the muon neutrino oscillating to either a tau or a theoretical sterile neutrino. The 60%, 90% and 99% confidence intervals in the $\Delta m^2$ versus $sin^2(2\theta)$ plane corresponding to this signal are shown in figure 1.5.

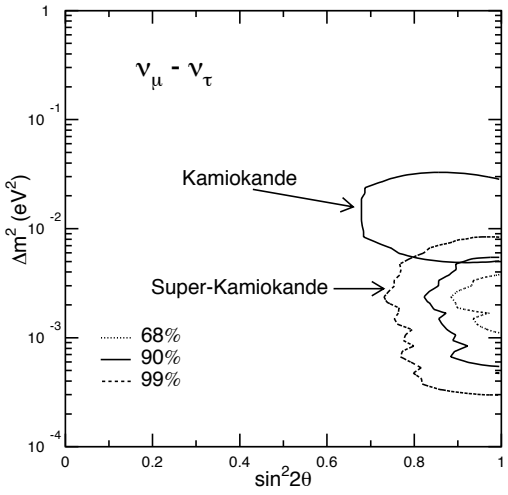


Figure 1.5: The 60%, 90% and 99% confidence intervals for $\Delta m^2$ versus $sin^2(2\theta)$ for $\nu_\mu \longrightarrow \nu_\tau$ oscillation based on the Super Kamiokande data. The 90% confidence interval determined previously by the Kamiokande experiment is shown for comparison [51]

## 1.7 NAUSICAA

There have been two main techniques used in the search for $\nu_\mu \longrightarrow \nu_\tau$ oscillation through the production of $\tau^-$ by $\nu_\tau$. The first technique utilises a large tracker with good momentum resolution as well as particle identification and calorimetry to identify the $\tau^-$ indirectly by locating the decay products of the $\tau^-$ and using kinematic cuts to remove background. This technique requires the accurate measurement of the missing transverse momentum in the event and was used in the NOMAD [8] experiment. The second technique requires the direct identification of the $\tau^-$ on an emulsion stack and was used in the CHORUS [7] experiment.

A proposal has been made in [9] and [10] to design a different experiment that would combine the best features of both techniques described above. This proposed design for A Neutrino ApparatUS with Improved CApAbilities (NAUSICAA) contains a tracker, calorimeter and muon identification similar to the NOMAD experiment but also has an instrumented target consisting of emulsion stacks separated by silicon detectors to enable an accurate extrapolation from the large tracker into the emulsion.

The NAUSICAA design would allow the analysis to use both kinematical criteria (such as missing momentum) and topological criteria (such as

displaced vertices or impact parameter measurements) to identify the $\tau^-$ produced by the charged current interaction of a $\nu_\tau$.

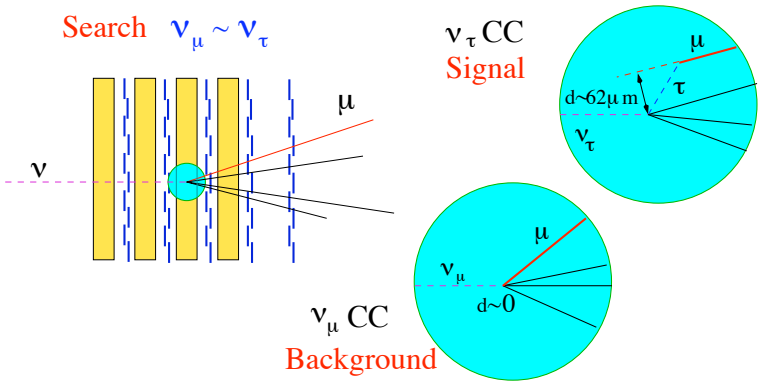


Figure 1.6: Definition of Impact Parameter

Figure 1.6 shows the definition of Impact Parameter. It can be seen that when looking for $\tau^-$ through the decay $\tau^- \longrightarrow \mu^- \nu_\tau \overline{\nu_\mu}$ the main background will be due to $\nu_\mu$ charged current interactions. This background will have a very small impact parameter however, compared to that of a $\mu^-$ resulting from the decay of a $\tau^-$.

A comparison of the impact parameter distribution and that of the impact parameter significance for $\mu^-$ produced in $\nu_\mu$ charged current interactions and those as a result of the decay of a $\tau^-$ is shown in figure 1.7. This comparison was made using a Monte Carlo simulation of the NAUSICAA design.

## 1.8 Past Experiments

The phenomenon of charm production by neutrinos had been investigated by a number of experiments since 1974 [52].

Three different methods have been used to study the production of charmed hadrons:

- **Dilepton :** Dilepton studies look for the semi-leptonic decays of the charmed hadrons. Because a $\nu_\mu$ charged current interaction will produce charm while $\overline{\nu_\mu}$ produces anti-charm, there is a simple signature for the semi-leptonic decay. A charmed hadron produced by a $\nu_\mu$ interaction can decay semi-leptonically to a $\mu^+$ or $e^+$ and so the dilepton signature results from the leading $\mu^-$ produced by the neutrino interaction and the opposite signed lepton produced in the charm decay.

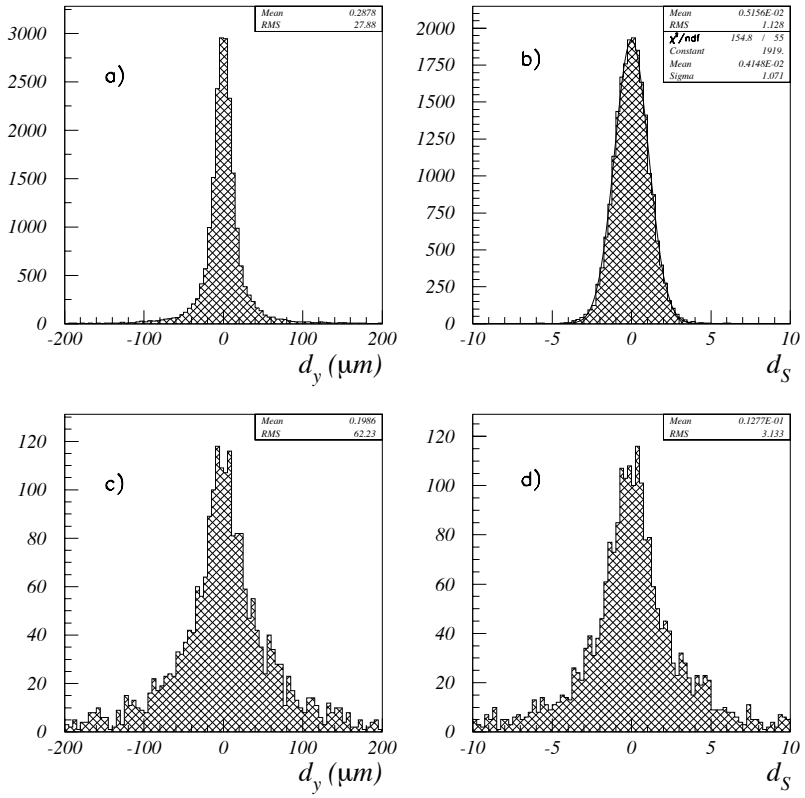


Figure 1.7: Projected impact parameter ($d_y$) and impact parameter significance ($d_s \equiv d_y/\sigma_y$ for $\nu_\mu$ CC interactions (a and b) and for $\nu_\tau$ CC interactions (c and d).

The most common studies of charm production by neutrinos have been through the analysis of dilepton events. The different analyses can be further categorised by the type of detector used:

- **Counter Experiments :**
  - **FMMF Collaboration :** This detector was a low density sand-steel calorimeter which used flash chambers for particle tracking. It ran in the Quad-Triplet beam at the Fermilab Tevatron [53]. This experiment looked for dimuons and required that both muons have a reconstructed momentum in excess of 10 GeV.
  - **CDHS Collaboration :** Running at the CERN SPS, the CERN-Dortmund-Heidelberg-Saclay detector accumulated the largest sample of opposite sign dimuons to date [54]. The experiment was a calorimeter using a magnetized steel target with drift chamber tracking and required that both muons have a momentum greater than 5 GeV.
  - **CCFR Collaboration :** The CCFR group also used a high density target calorimeter, this one made of iron plates interleaved with scintillator planes, and drift chambers for tracking. It ran in the Quad-Triplet beam at the Fermilab Tevatron and has presented many results on opposite sign dimuons, including the first analysis using Next-to-Leading order QCD.
  - **CHARM II Collaboration :** The CHARM II detector was a massive, fine-grained and low density detector designed for the study of muon neutrino scattering on electrons. It used glass as the neutrino target and streamer tubes instrumented with cathode strips as both the calorimeter and tracking detector. A dimuon analysis was performed, imposing a 6 GeVcut in the momentum of both muons.
  - **NOMAD FCAL :** The forward calorimeter (see Section 2.4.2) of the NOMAD experiment was used to measure dimuons produced in the iron/scintillator target of the FCAL and subsequently tracked and identified in NOMAD. The charm mass, strange sea content of the nucleon and the average semileptonic branching ratio of charm were determined [5], [6].
- **Bubble Chamber Experiments :**
  - **Columbia-BNL-Rutgers :** The highest statistics dilepton ($\mu^- e^+$) sample from a bubble chamber experiment was gath-

ered by the Columbia-BNL-Rutgers collaboration. The experiment used the Fermilab 15-ft bubble chamber filled with a Ne-$H_2$ mixture [56] and accepted events in which the momentum of the secondary positron was above 300 MeV/c.

  * **E632 :** This experiment also used the 15-ft bubble chamber at Fermilab with a Ne-$H_2$ mix [57]. Their dimuon sample required both muons to have greater than 4 GeV/c of momentum.

- **Invariant mass reconstruction without a secondary vertex:** A different method of studying charm production is to attempt to fully reconstruct one or more decay modes using accurately measured momenta from bubble-chamber-like experiments [50]. This method suffers from a large combinatorial background and a commonly used modification is to look for a chain of decays such as:

$$D^{+^*} \rightarrow D^0 \pi^+ \tag{1.51}$$
$$D^0 \rightarrow K^- \pi^+ \tag{1.52}$$

  This technique allows a stronger rejection of background, but suffers from a low rate due to the branching fractions of the decays and reconstruction efficiencies.

- **Invariant mass reconstruction with a secondary vertex:** This method also requires the accurate determination of the momenta of the charm decay products, however extra information is available in the form of a reconstructed secondary vertex. This extra information can be used to perform a constrained fit on a candidate charm decay to more strongly reject background. Before CHORUS and NOMAD-STAR, the only experiment to perform this type of analysis was E531:

  – **E531 :** Although only accumulating a small number of events, the Fermilab E531 experiment is unique in being an emulsion experiment [58, 65]. This detector measured charm particle production directly by identifying and reconstructing the charm particle decay in the emulsions. Much of the information used in Monte Carlo simulations of charm production by neutrinos comes from this experiment.

| Counter Experiments | | | |
|---|---|---|---|
| Experiment | $E_\nu$ (GeV) | $\mu^-\mu^+$ | $\mu^+\mu^-$ |
| FMMF | 30-600 | 393 | |
| CDHS | 0-300 | 11041 | 3685 |
| CCFR | 30-600 | 5030 | 1060 |
| CHARM II | 30-300 | 3100 | 700 |
| NOMAD | 0-300 | 3116 | 112 |
| Bubble Chamber Experiments | | | |
| Experiment | $E_\nu$ (GeV) | $\mu^-l^+$ | $\mu^+l^-$ |
| Col-BNL | 0-200 | 461 ($\mu^-e^+$) | |
| E632 | 10-450 | 40 ($\mu^-\mu^+$) | 8($\mu^+\mu^-$) |
| NOMAD | 0-300 | 320 ($\mu^-e^+$) | |
| Emulsion Experiment | | | |
| Experiment | $E_\nu$ (GeV) | Charmed Hadron Events | |
| E531 | 0-250 | 122 | |

Table 1.3: Summary of data samples from previous neutrino charm production experiments from [5].

A summary of the results obtained from these experiments is given in Table 1.3. It can be seen that although there exist high statistics of dilepton events, there are very few events where the charmed hadron was reconstructed as a separate vertex.

## 1.9 Summary and Motivation

In this thesis, the construction and operation of a prototype detector (STAR) will be described. This detector was designed to test the NAUSICAA concept and operated inside the NOMAD experiment at CERN during 1997 and 1998.

Chapter 2 describes the NOMAD experiment, which was one of two experiments in the CERN west area looking for $\nu_\mu \longrightarrow \nu_\tau$ oscillations.

Chapter 3 describes the construction and alignment of the STAR detector.

In Chapter 4, the reconstruction of hits in the silicon detectors of STAR is detailed.

An implementation of the Kalman track fit specific to STAR is described in chapter 5.

Chapter 6 defines the implementation of the Kalman vertex fit for STAR.

Using the STAR detector, it will be possible to test the impact parameter

resolution of the design and thus the feasability of the NAUSICAA design for a future $\nu_\mu \longrightarrow \nu_\tau$ oscillation experiment.

Given the limits on $\nu_\mu \longrightarrow \nu_\tau$ oscillation already set by the NOMAD and CHORUS experiments, it is extremely unlikely that a $\nu_\tau$ would be observed in the STAR detector. However it has been shown in section 1.5 that charmed mesons are expected to be produced in charged current $\nu_\mu$ interactions and these have similar masses and lifetimes to that of the $\tau^-$. If STAR is able to directly reconstruct the decay vertices of charmed mesons, it will be able to demonstrate the ability to identify a $\nu_\tau$ interaction as well as adding to the very small number of charm mesons produced by neutrinos and observed through the reconstruction of a secondary vertex.

In chapter 7, the method used to search for the production and decay of $D^0$, $D^+$, $D_S^+$, $D^{0^*}$ and $D^{+^*}$ is described.

Chapter 8 lists the results obtained by the STAR detector, including impact parameter resolution, single and double vertex resolution as well as the charm search.

Appendix A contains images from the NOMAD event display program as modified for STAR for a Monte Carlo charm event as well as a typical reconstructed $\nu_\mu$ charged current interaction from the data.

Appendix B contains the cuts used in the silicon hit reconstruction as described in chapter 4.

# Chapter 2

# The NOMAD Experiment

## 2.1 Introduction

In this chapter the NOMAD experiment and the neutrino beam will be described. The results of a simulation of the neutrino beam will be presented with a discussion of the types of neutrino interactions that are expected to be observed in NOMAD.

## 2.2 Aim of the NOMAD Experiment

The NOMAD (Neutrino Oscillation MAgnetic Detector) experiment is looking for the appearance of neutrino oscillations [8]. It is assumed in the standard model that the neutrino has no mass. However there is no theoretical reason why neutrinos should be massless, but experiments so far have only been capable of putting upper limits on the masses of neutrinos. It was shown in Chapter 1 that if at least one neutrino has a non-zero mass then as a consequence of the difference in the masses of the neutrinos it is theoretically possible for one species to oscillate into another as the neutrinos propagate through space. The neutrino beam that NOMAD is exposed to is composed of mainly muon-neutrinos ($\nu_\mu$). The NOMAD experiment is looking for the appearance (and interaction) of tau-neutrinos ($\nu_\tau$) indicating an oscillation $\nu_\mu \rightarrow \nu_\tau$ [2], [3]. In order to detect the presence of the tau neutrino, NOMAD has been designed to be very good at identifying electrons and muons. It also needs to be able to make accurate measurements of the momentum of each particle produced in an event. The small component of electron neutrinos in the beam, has allowed a search for $\nu_e \rightarrow \nu_\tau$ oscillations [4].

## 2.3 The CERN West Area Neutrino Beam Facility

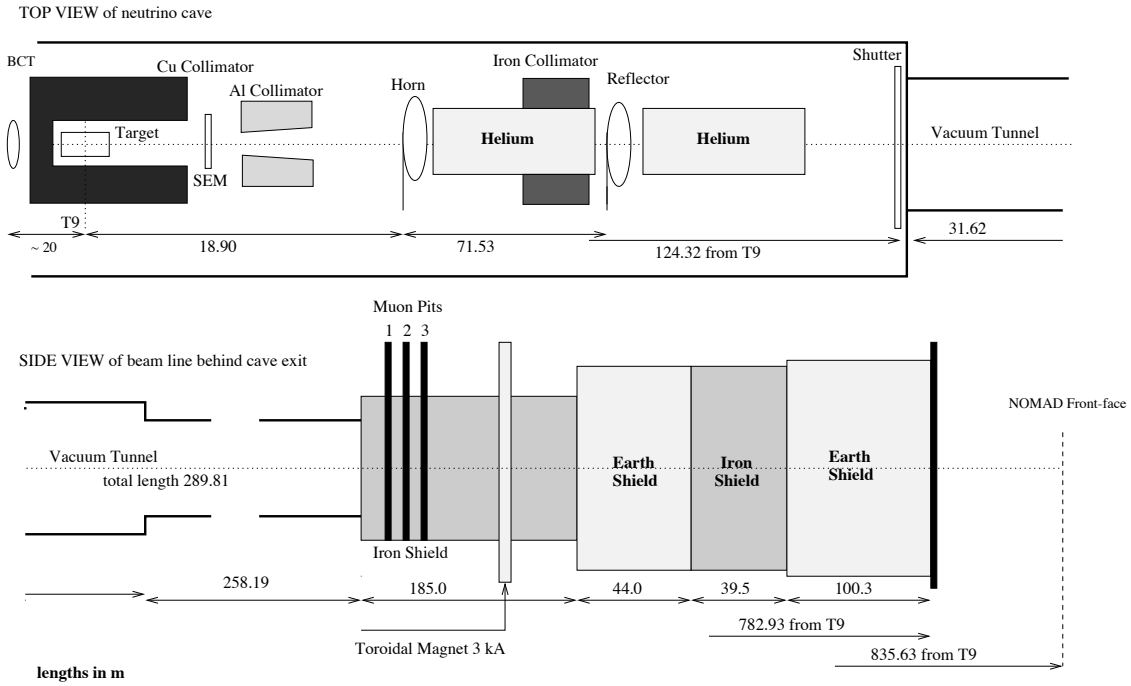


Figure 2.1: The West Area Neutrino Facility (WANF)

Neutrinos are produced at CERN through several stages. The process starts with the Super Proton Synchrotron (SPS) which accelerates protons to 450 GeV. The accelerator cycles every 14.4 seconds and during that cycle, protons are directed onto a beryllium target during two separate extractions (known as neutrino spills). In order to calculate how many neutrinos to expect at NOMAD, it is necessary to follow the production starting with the protons hitting the Be target (the number of protons on target is abbreviated POT). The interaction of the protons in the Be target produces secondary particles (mainly pions and kaons) which are focussed with two magnetic focussing devices known as the horn and reflector, into a collimated beam. The pions and kaons are then allowed to decay in a vacuum chamber 290m long producing neutrinos. Shielding of 225m of iron and 140m of earth prevents everything except the neutrinos and all but the high energy muons from making it to the NOMAD detector 835m from the beryllium target.

Muons of both signs and hence $\nu_\mu$ and $\overline{\nu_\mu}$ are produced through the following decays:

$$\pi^+ \rightarrow \quad \mu^+\nu_\mu \quad \sim 100\% \tag{2.1}$$
$$K^+ \rightarrow \quad \mu^+\nu_\mu \quad \sim 64\% \tag{2.2}$$
$$K^+ \rightarrow \quad \pi^o\pi^+(\rightarrow \mu^+\nu_\mu) \quad \sim 21\% \tag{2.3}$$
$$K^+ \rightarrow \quad \pi^o\pi^o\pi^+(\rightarrow \mu^+\nu_\mu) \quad \sim 1.7\% \tag{2.4}$$
$$K^+ \rightarrow \quad \pi^o\mu^+\nu_\mu \quad \sim 3\% \tag{2.5}$$
$$K^0_L \rightarrow \quad \pi^\pm\mu^\mp\nu_\mu \quad \sim 27\% \tag{2.6}$$
$$K^0_L \rightarrow \quad \pi^o\pi^+(\longrightarrow \mu^+\nu_\mu)\pi^-(\longrightarrow \mu^-\overline{\nu_\mu}) \quad \sim 12.6\% \tag{2.7}$$
$$K^0_S \rightarrow \quad \pi^+(\longrightarrow \mu^+\nu_\mu)\pi^-(\longrightarrow \mu^-\overline{\nu_\mu}) \quad \sim 69\% \tag{2.8}$$

Electrons, positrons and the corresponding neutrinos ($\nu_e$ and $\overline{\nu_e}$) are also produced through the decays:

$$K^+ \rightarrow \quad \pi^o e^+\nu_e \quad \sim 5\% \tag{2.9}$$
$$K^0_L \rightarrow \quad \pi^\pm e^\mp\nu_e \quad \sim 39\% \tag{2.10}$$

Anti-neutrinos are produced through the charge-conjugate of the decays above. The values listed are the relative branching fractions of the individual decay modes.

In order to understand the neutrino beam at NOMAD, simulation programs have been developed to predict what types of neutrino will pass through NOMAD and what the distribution of their energies will be. The NUBEAM (version 6.00) simulation starts at the beginning with the protons interacting in the beryllium target and follows the decay products until they reach NOMAD. The resulting predictions show the energy spectra of each of the four types of neutrino that pass through NOMAD.

Results from Nubeam 6.00 are presented in figure 3.9 and table 3.1. NUBEAM is discussed in more detail in section 2.6.1.

The STAR detector (see Chapter 3) became operational in 1997, however shortly after some data acquisition problems were fixed, a fire brought the SPS to a halt for over 2 months while repairs were effected. This break can be seen in Figure 2.2 which shows the daily and cumulative protons on the neutrino target for 1997.

Figure 2.3 shows the daily and cumulative protons on the neutrino target for 1998.

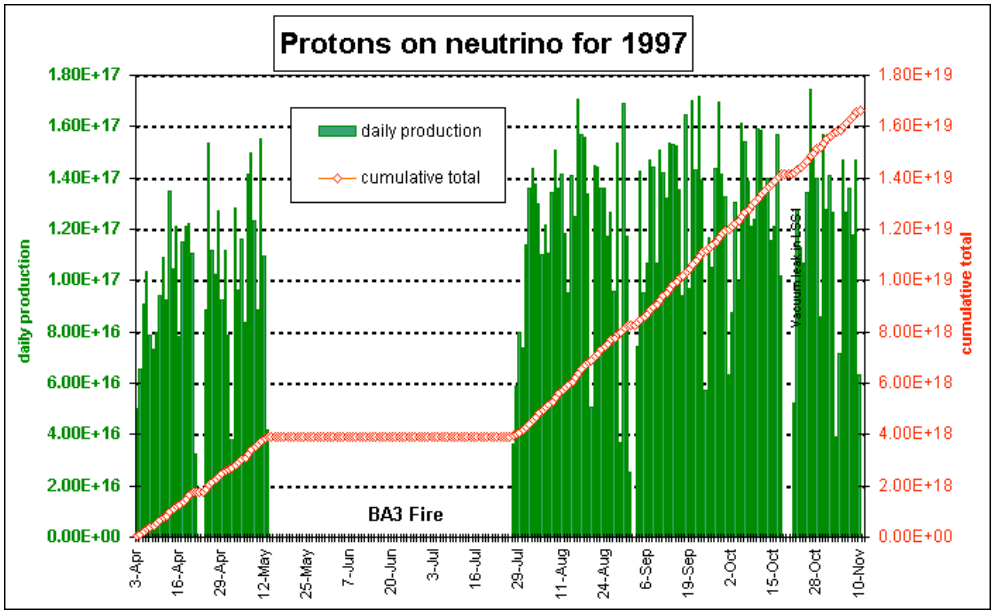


Figure 2.2: Protons on Target for 1997

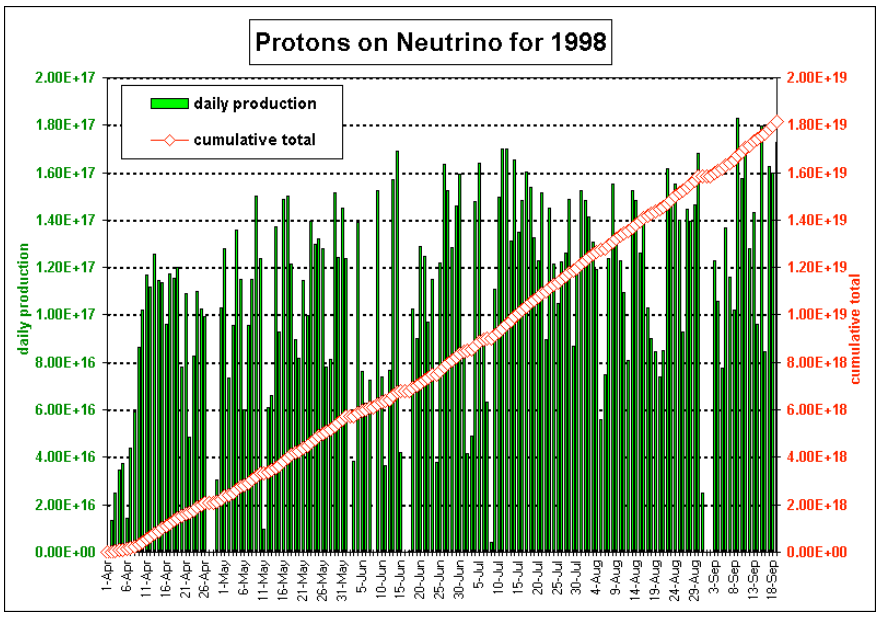


Figure 2.3: Protons on Target for 1998

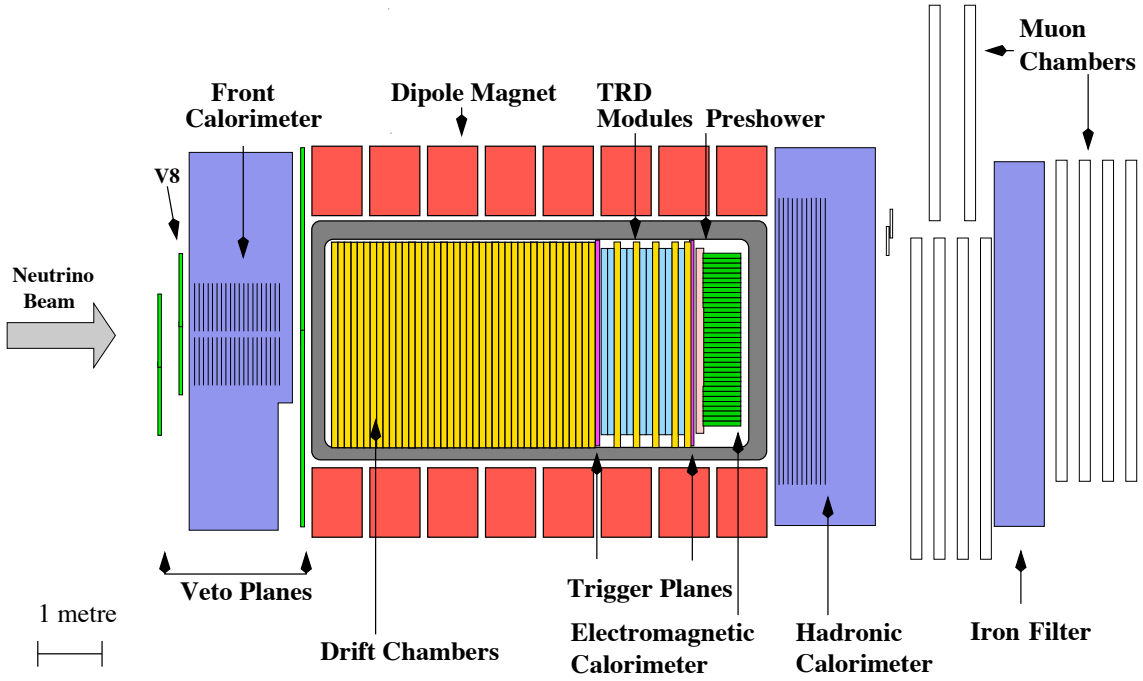


(a) Side View

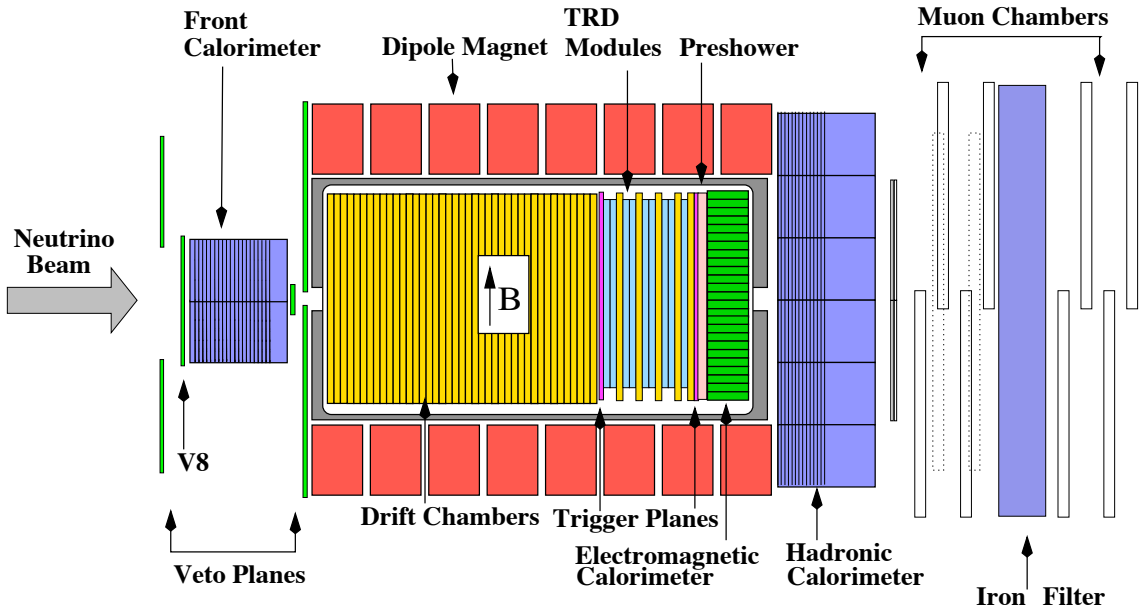


(b) Top View

Figure 2.4: The NOMAD detector

## 2.4 The NOMAD Detector

The NOMAD detector (Figure 2.4) consists of a number of subdetectors, most of which are located in a dipole horizontal magnetic field of 0.4T, perpendicular to the neutrino beam. The magnet was utilised previously in the UA1 experiment and has a volume $7.5 \times 3.5 \times 3.5\, m^3$

### 2.4.1 Veto

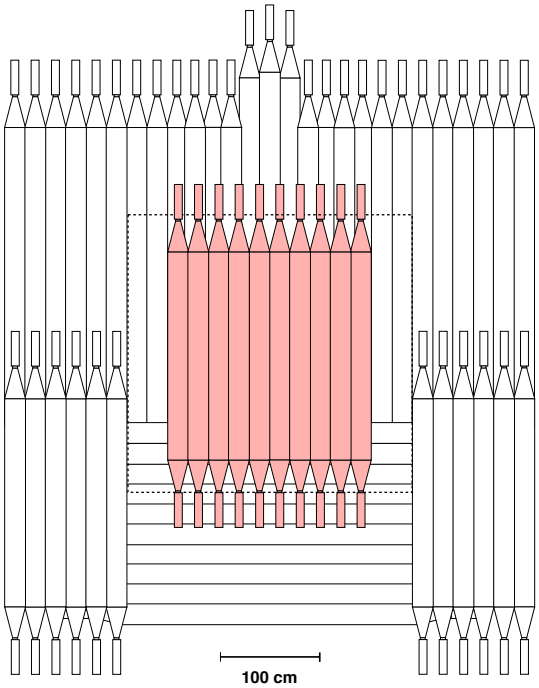


Figure 2.5: The Veto looking along the neutrino beam

The neutrino beam encounters the veto planes first. The veto planes are a collection of 59 scintillation counters covering an area $5 \times 5\, m^2$ (Figure 2.5) which respond to the passage of any charged particles. The aim of the veto is to reject the passage of charged particles that are produced upstream of NOMAD. The NOMAD data acquisition will not record an event if the veto has fired.

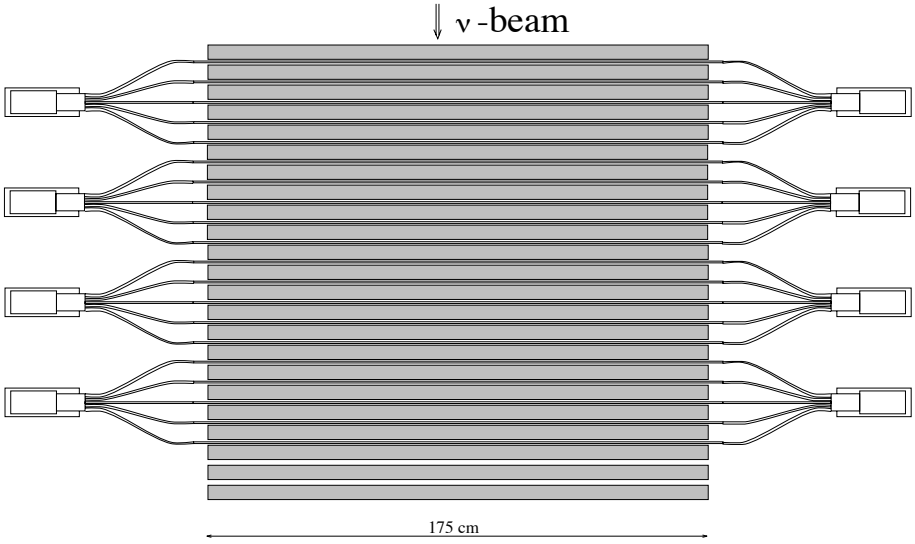


Figure 2.6: The FCAL viewed from above

### 2.4.2 Front Calorimeter

The front calorimeter (FCAL) sits at the upstream end of the magnet. The calorimeter consists of 23 iron plates 4.9cm thick. Twenty of the 23 gaps are instrumented with scintillation counters to measure the energy loss of the secondary particles produced in the iron. This calorimeter provides an additional heavy target for neutrino interactions for a search for neutral heavy leptons and for multi-muon studies, including the opposite-sign dimuon search published in [5] and [6].

### 2.4.3 Drift Chambers

Drift chambers measure the accurate position and tracking of charged particles. An argon (40%) - ethane (60%) mixture sits between potential strips and sensing wires. If a charged particle passes through the chamber, it will ionise the gas mixture. The 1kV/cm electric field produced by the potential strips causes the electrons produced in the ionisation to drift towards the sense wires with an average velocity of 50mm/$\mu$s. By measuring the time of arrival of the signals with respect to a reference time, the position can be determined to an accuracy of 180 $\mu$m.

The walls and support of the drift chambers act as the target material where the neutrinos interact with a total mass of 3 tonnes. Each drift chamber covers an area of $3 \times 3m^2$ and has sense wires running horizontally and

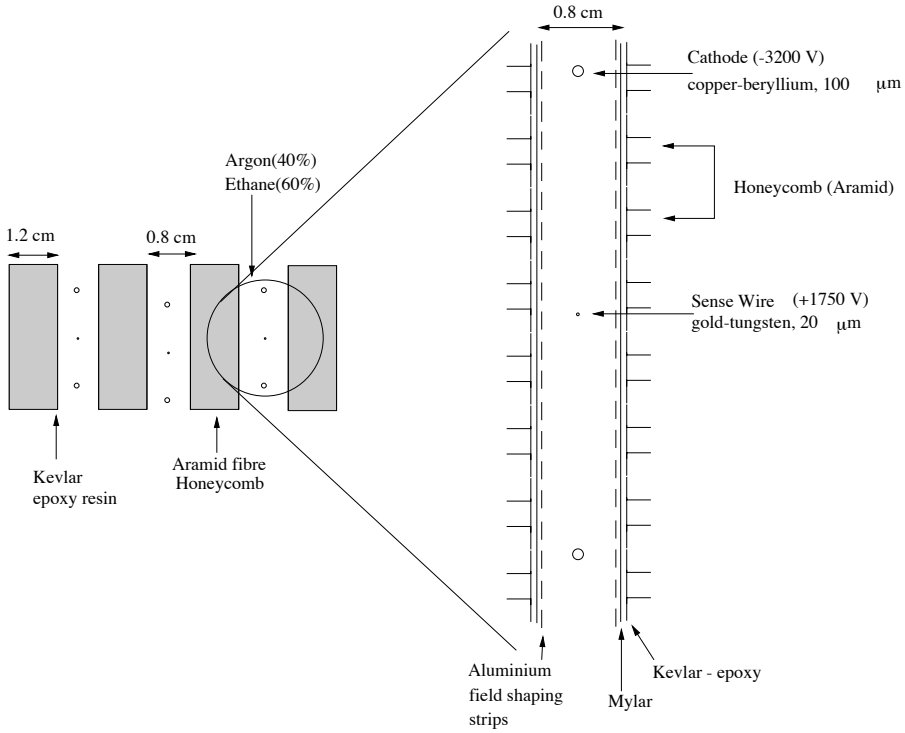


Figure 2.7: Detail of a NOMAD Drift Chamber

at two other planes $\pm 5^\circ$ to the magnetic field (Figure 2.7). There are 11 modules of four chambers each comprising the main target. The Transition Radiation Detector (TRD) region contains 5 additional chambers. Because the magnetic field causes the directly detectable charged particles to move in a curved path, sign and momentum can be determined as well as position.

### 2.4.4 Trigger

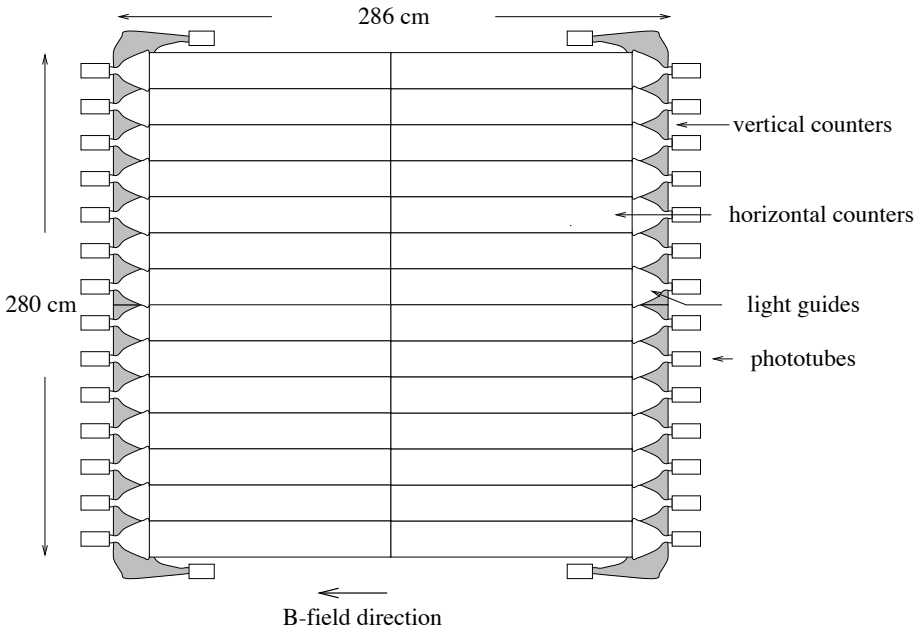


Figure 2.8: One of the two trigger planes

There are two trigger planes of scintillators inside the magnetic field of NOMAD (Figure 2.8). The first trigger plane is situated at the back of the target with the second trigger plane behind the TRD region. The trigger condition that flags a neutrino interaction in the target is $\overline{V}T_1T_2$, meaning that the veto must not have fired and there must have been a coincidence between the two trigger planes. This condition corresponds to a neutral particle (the neutrino) interacting inside the drift chambers and producing charged particles which are detected by the trigger. From looking at the various possible interactions it can be seen that while the charged current interaction always produces a muon which should fire the trigger, the neutral current interaction must rely on the secondary particles to fire the trigger. This results in a slightly lower trigger efficiency for neutral current events than for charged currents.

### 2.4.5 Transition Radiation Detector

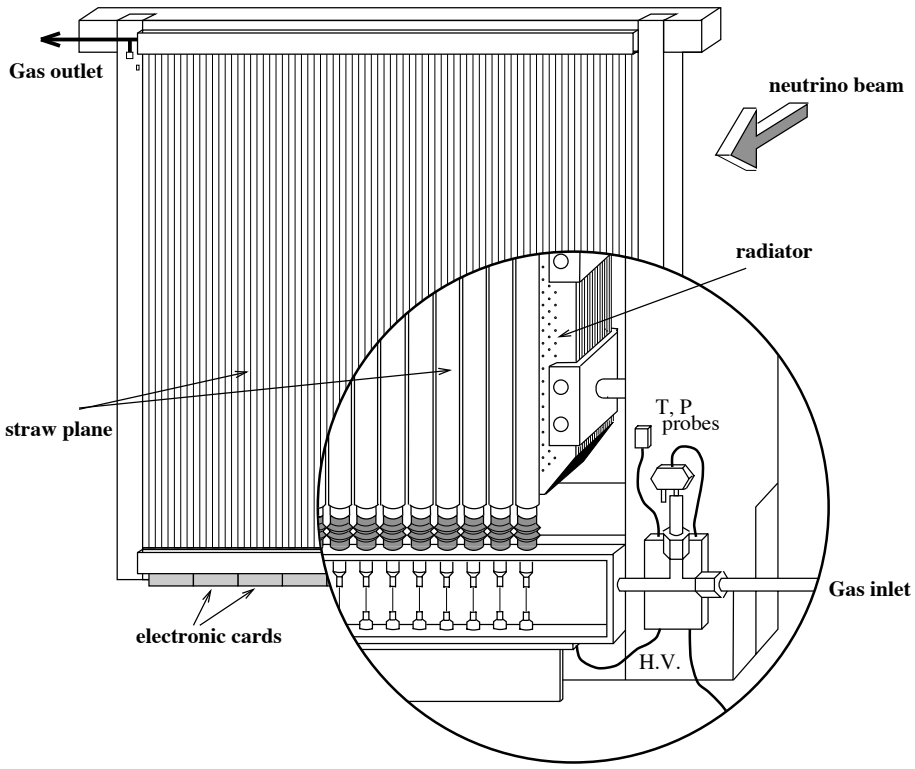


Figure 2.9: The Transition Radiation Detector

The Transition Radiation Detector (TRD) consists of 9 modules (Figure 2.9), each module made up of 315 plastic foils (the radiator) and a detection plane of 176 vertical proportional tubes (called straw tubes). The purpose of the TRD is to differentiate between electrons and strongly interacting particles such as pions. Electrons crossing the radiator planes emit transition radiation, due to the rapid change of refractive index as the particle crosses planes of plastic and air. This radiation is emitted in the form of X-rays that are measured with the straw tubes. The X-ray energy depends on the Lorentz factor $\gamma = \frac{E}{m}$ of the particle. This property is used to differentiate between electrons and hadrons. The TRD achieves a $\pi$ to electron rejection of $10^3$ for a 90 % electron efficiency ( [60] [61]).

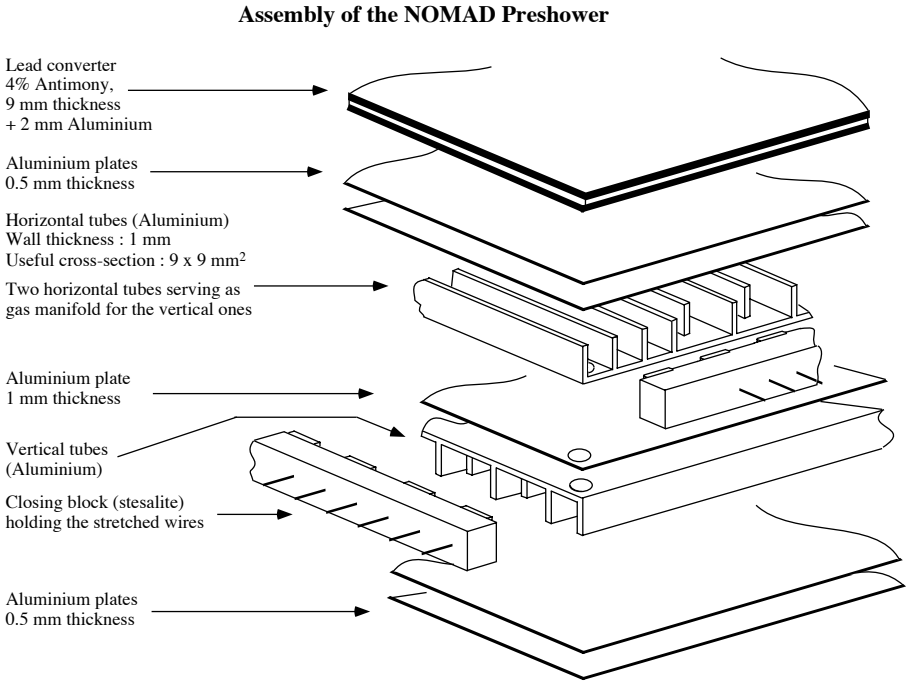


Figure 2.10: The Preshower

### 2.4.6 Preshower

The preshower (PRS) starts with a lead converter which causes photons and electrons to start an electromagnetic shower (Figure 2.10). Behind the converter are a plane of horizontal proportional tubes followed by a plane of vertical tubes. Each proportional tube has a useful cross-section of $9 \times 9mm^2$ and records the electromagnetic energy deposited. The preshower is also useful because it has a higher spatial resolution than the Electromagnetic Calorimeter. Tracks from the drift chambers can be matched to first the preshower and then to the relatively coarse spatial information in the electromagnetic calorimeter.

### 2.4.7 Electromagnetic Calorimeter

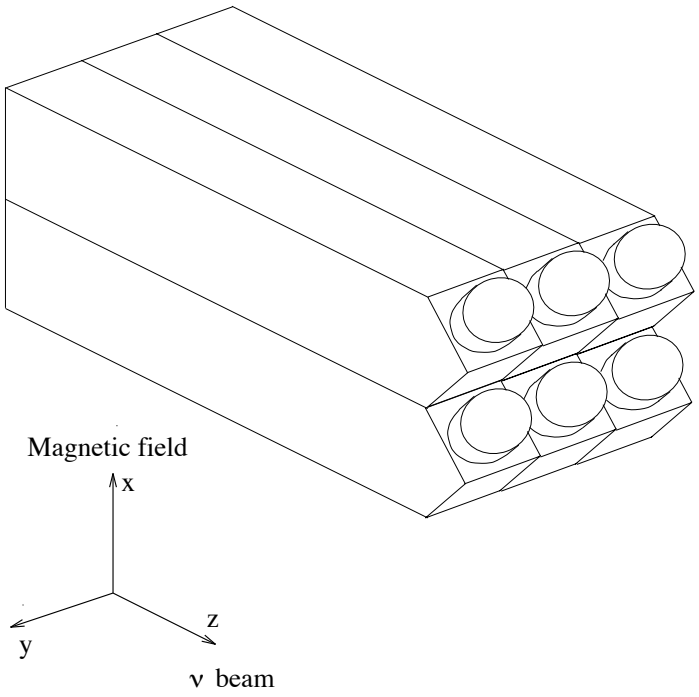


Figure 2.11: Glass counters of the Electromagnetic Calorimeter

The measurement of the electromagnetic energy deposition is performed in the Electromagnetic Calorimeter (ECAL [62]). It consists of 875 lead glass counters (Figure 2.11) with cross sectional area $8 \times 11cm^2$ and 19 radiation lengths deep (ensuring that all of the electromagnetic component is contained). The counters are read out by two stage photomultiplier tubes

(tetrodes). The energy resolution of the electromagnetic calorimeter has been measured to be:

$$\frac{\sigma(E)}{E} \sim 0.0104 + \frac{0.0322}{\sqrt{E}} \tag{2.11}$$

Where the energy E is in GeV. The preshower, in combination with the electromagnetic calorimeter, can be used to identify electrons from hadrons. A pion rejection factor of 100 can be obtained for a 90% electron efficiency. Electrons and photons with energies between about 100MeV and 100 GeVwill shower their energy into lead-glass detectors. Muons and strongly interacting particles only lose a small amount of energy due to ionisation in the calorimeter.

### 2.4.8 Hadron Calorimeter

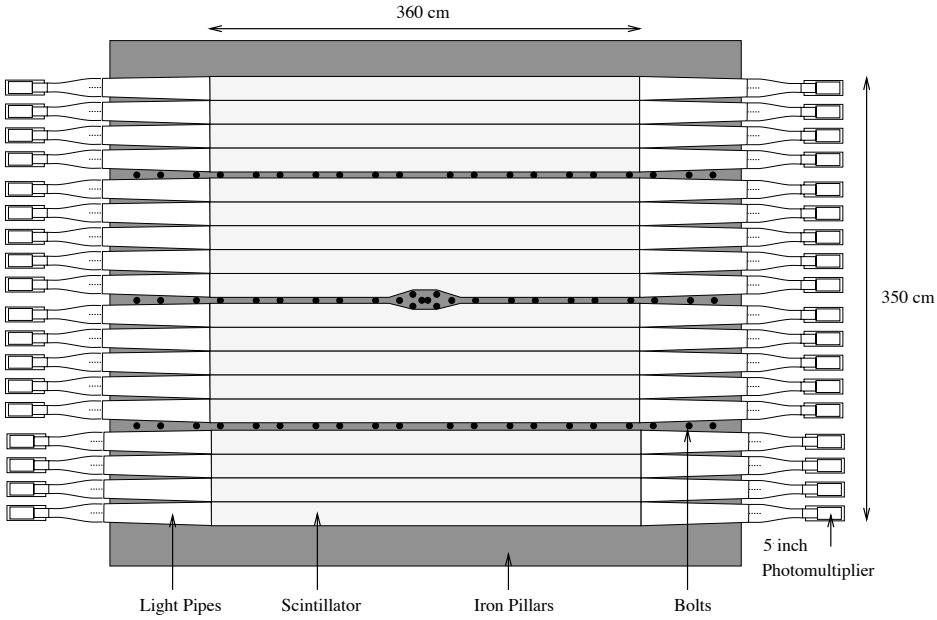


Figure 2.12: Front view of the Hadronic Calorimeter

The Hadronic Calorimeter (HCAL) is an iron-scintillator calorimeter downstream of the electromagnetic calorimeter used for the energy and position measurement of hadrons (Figure 2.12). Most of the hadronic energy is contained in the 3.2 interaction lengths in depth. The hadron calorimeter has an energy resolution of

$$\frac{\sigma(E)}{E} \sim \frac{1.2}{\sqrt{E}} \tag{2.12}$$

where E is again measured in GeV.

### 2.4.9 Muon Chambers

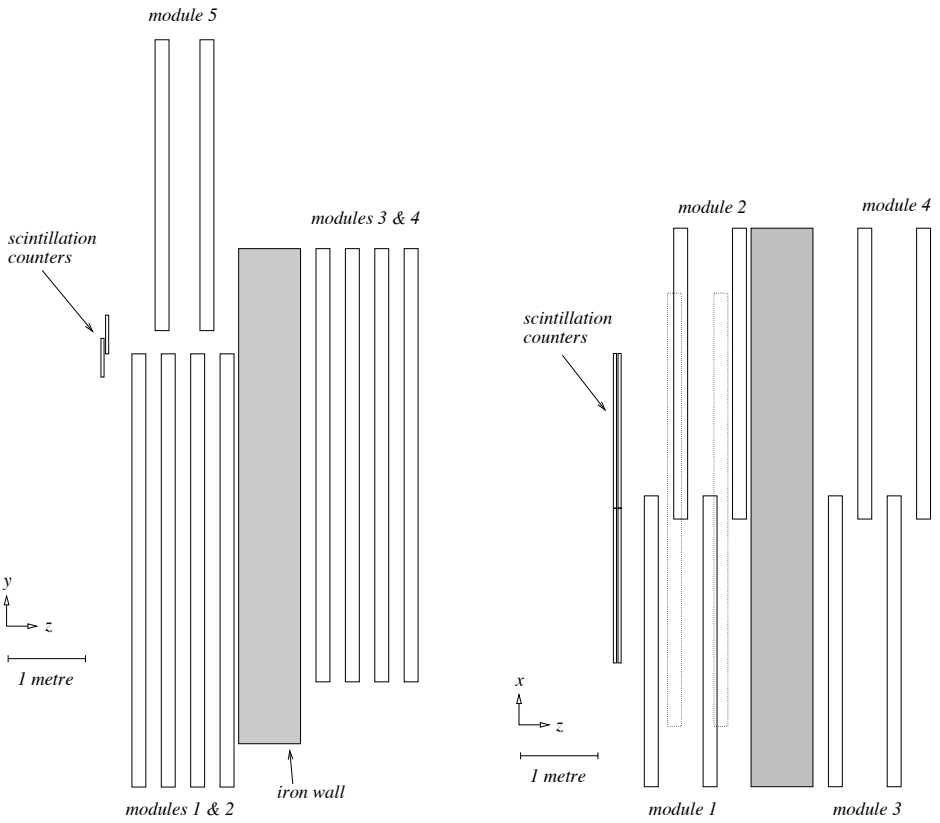


(a) Side View (b) Top View

Figure 2.13: The Muon Chambers

The final components, the muon chambers are pairs of drift chambers (Figure 2.13) with position resolution of 450 $\mu$m, separated by 80cm of iron shielding. Only muons and energetic pions will make it through to the muon chambers, since there is additional shielding between the hadron calorimeter and the first muon chamber. The tracks in the first chamber can be matched

to those in the second chamber, taking into account the multiple scattering caused by the shielding. It is therefore possible to correctly identify muons in NOMAD as is required for the oscillation search. A muon will only leave a minimum ionizing pulse (mip) of energy in the Hadron Calorimeter, whereas a strongly interacting punch-through particle will tend to deposit more.

### 2.4.10 Silicon Target

During 1997 and 1998 a new detector named STAR (Silicon TARget) was installed in place of the first module of drift chambers. It is described in detail in Chapter 3.

## 2.5 Data Acquisition and Handling

### 2.5.1 Data Acquisition

Each of the subdetectors described previously have separate FASTBUS modules which perform the appropriate digitisation for that detector. Each of the modules is then readout by 5 VME-based boards based on the Motorola 68040. Another VME processor (the "Event Builder") assembles the blocks of data from each of the other processors into a single structure which now contains the complete information for a single event.

### 2.5.2 Triggering

The NOMAD trigger is described in reference [63].

Each 14.4$s$ cycle of the SPS was broken up into 4 main periods, shown in Figure 2.14.

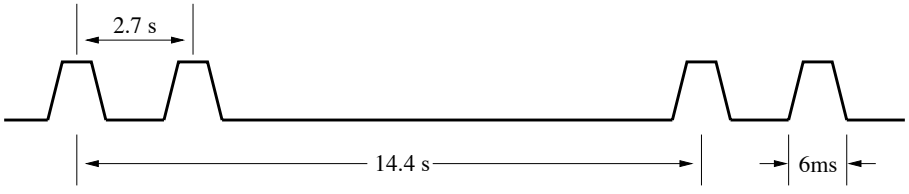


Figure 2.14: Timing of the neutrino target extractions

The first extraction is referred to as $NU1$ as it is the first period where neutrinos are being produced. This is followed by other extractions to test beams in a neighbouring hall. A large quantity of muons, resulting from

| Trigger Signal Components | |
|---|---|
| $\mathbf{T_1}$ | First trigger plane signal |
| $\mathbf{T_2}$ | Second trigger plane signal |
| $\mathbf{T_S}$ | The trigger plane at the back of STAR |
| **V** | Veto signal |
| $\mathbf{V_8}$ | Signal from the veto plane in front of the FCAL |
| $\mathbf{V_S}$ | Signal from the veto plane immediately in front of STAR |
| **Fcal** | FCAL signal |
| **Fcal′** | Signal from the FCAL at a lower discriminator threshold |
| **Ecal** | ECAL signal |
| **Ecal′** | Signal from the ECAL at a lower discriminator threshold |
| **Hcal** | HCAL signal |

Table 2.1: Individual signals which are used to generate NOMAD triggers.

the decay of particles in these beams, then passes through the two neutirno experiments. The period when muons pass through the detector is referred to as $MU$. A second extraction, $NU2$ follows the $MU$ period, after which the SPS requires time for a new bunch of protons to be accelerated.

The data acquisition system breaks the cycle into two main periods for the purposes of triggering. The neutrino gate consists of the periods $NU1$ and $NU2$ while the muon gate is the period $MU$.

The following triggers are implemented in NOMAD during the neutrino gates. The trigger signal components are described in Table 2.1. :

- $\overline{\mathbf{V}} \times \mathbf{T_1} \times \mathbf{T_2}$ : This was the main NOMAD trigger as it selects neutrino interactions inside the Drift Chambers. The rate for this trigger was approximately $5.0/10^{13}$p.o.t, however only $0.5/10^{13}$p.o.t are useful candidates. The remaining triggers were due to cosmic rays, non-vetoed muons and neutrino interactions inside the magnet coil and flux return yoke.

- $\overline{\mathbf{V_8}} \times \mathbf{Fcal}$ : The discriminator threshold was set at 75 mV, which corresponds to an energy of approximately 2.0 GeV, in order to trigger on deep-inelastic interactions in the FCAL.

- $\overline{\mathbf{V_8}} \times \mathbf{Fcal'} \times \mathbf{T_1} \times \mathbf{T_2}$ : The lower discriminator threshold in this trigger allows the selection and study of quasi-elastic like events in the FCAL.

- $\overline{\mathbf{V_8}} \times$ **Ecal** :This configuration was used during most of the 1995 run and was intended to use the ECAL as a neutrino target in order to conduct a search for a new gauge boson in $\pi^0$ decays [45], a search for $\nu_\mu \longrightarrow \nu_e$ oscillations [46] and a search for the so-called KARMEN anomaly [47].

- $\overline{\mathbf{T_1} \times \mathbf{T_2}} \times$ **Ecal** : During the 1996-1998 data-taking runs, the ECAL trigger above was changed to remove the veto signal and instead use the $T_1$ and $T_2$ planes as a veto. This change resulted in an increased live-time.

- $\overline{\mathbf{V_8} \times \mathbf{V_S}} \times \mathbf{T_S} \times \mathbf{T_1}$ : This trigger selects neutrino interactions inside the STAR detector. In a similar manner to the $\overline{V} \times T_1 \times T_2$ trigger, the majority of events selected were of no interest and were mainly caused by non-vetoed muons, and low-momentum particles produced in a neutrino interactions elsewhere in the forward part of NOMAD being bent in the magnetic field and producing $T_S$ while other tracks from the intial interaction produced $T_1$.

- **CHORUS** : The CHORUS trigger was motivated by a search for neutral heavy particles and was a joint trigger with the CHORUS experiment [7]. Both experiments recorded events when a simultaneous interaction was observed in NOMAD and CHORUS. In addition to the requirement for a signal from the CHORUS muon spectrometer and the $\overline{V} \times T_1 \times T_2$ from NOMAD, plane 7 of the CHORUS streamer tubes, which were behind the muon spectrometer, was used as a veto to supress beam muons and charged current interactions in CHORUS. This allowed a search for the production in CHORUS of a hypothetical neutral heavy particle which subsequently decays in NOMAD.

- **RANDOM** : A random trigger was also implemented in order to study detector occupancy, mainly due to out-of-time muons from the neutrino beam. The trigger consisted of a signal $22\mu s$ after every $16^{th}$ valid neutrino trigger. The delay is equivalent to one complete turn around the SPS and was chosen to guarantee a coincidence between the trigger and a proton-extraction.

The following triggers were implemented in place of those above during the muon gate.

- $\mathbf{V} \times \mathbf{T_1} \times \mathbf{T_2}$ : This trigger responds to through-going tracks in the full NOMAD volume and is used for calibration of the Drift Chambers

as well supplying a large sample of minimum ionising muons for the calibration of other detectors

- $\mathbf{V_8 \times Fcal' \times T_1 \times T_2}$ : This trigger selects muons passing through the FCAL.
- $\mathbf{V_8 \times T_1}$ and $\mathbf{V_8 \times T_2}$ : These triggers were implemented in order to measure the separate efficiencies of the $T_1$ and $T_2$ trigger planes.
- $\mathbf{V \times T_1 \times T_2 \times Ecal \times \overline{Hcal}}$ : This trigger allows the selection and study of electrons from muon decay or delta rays for measuring the electron identification efficiency. The purpose of the $\overline{Hcal}$ signal is to exclude triggering on muons when looking for muon decays. When delta rays are required this last signal is not included.
- $\mathbf{V_8 \times V_S \times T_S \times T_1}$ : This trigger selects muons passing through the STAR detector. Events selected by this trigger were used for the calibration and alignment of the STAR detector.

## 2.6 The NOMAD Software

Several different software packages have been necessary in order to conduct an analysis on data taken with NOMAD.

The simulation of the physical processes occuring and the response of each detector is made through a series of programs that utilise Monte Carlo methods and paramaterisations of measured quantities.

The simulation of NOMAD proceeds as folows:

1. Simulation of the neutrino beam.
2. Simulation of the neutrino interaction.
3. Simulation of the progress of the interaction products, including the response of the detectors.

### 2.6.1 Beam Simulation

Simulation of the WANF beamline is performed by a GEANT [40] based program called NUBEAM [44]. NUBEAM simulates the interaction of the SPS proton beam with the neutrino target and follows the particles produced in this collision through the focussing and shielding elements of the beam-line in order to predict the position and 4-momentum of the neutrinos produced in the subsequent decays.

The task of simulating the initial interaction of the proton beam was originally performed by GEANT within the NUBEAM package, however it has since been altered to allow a stand-alone implementation of FLUKA to perform the same task.

Due to the geometry of the WANF beamline, the neutrino beam actually encounters NOMAD from below the z axis and rises at an angle of approximately 42 milliradians. It is necessary to make an allowance for this angle when using the output of NUBEAM, as the radial and energy distributions are only calculated for a single position in Z which corresponds to the center of the ECAL. Figure 2.15 shows the reconstructed angle in the YZ plane of the leading muon in $\nu_\mu$ and $\overline{\nu_\mu}$ charged current events from the 1998 STAR data.

### 2.6.2 Event Generation

Simulated events in NOMAD are generated using the NEGLIB [43] program. The program, based on LEPTO 6.1, [41] can simulate quasi-elastic, resonant and deep-inelastic lepton-nucleon scattering. All the Monte Carlo events used in this thesis, however are deep-inelastic.

Rather than tracking a simulated neutrino from production to interaction in NOMAD, the subdetector in which the neutrino is to interact is chosen before execution and the position in the Z direction determined from the distribution of density in that subdetector.

The profile of the neutrino beam as determined by the beam simulation is sampled as energy versus the square of the radius of the position of the neutrino in the XY plane. These distributions are used to simulate the energy of the incoming neutrino and the interaction point.

It is also possible to select a specific species of neutrino and to restrict the interactions to a range in radius and energy.

The fragmentation (that is the collection of produced partons into bound hadrons) is simulated with the JETSET 7.4 library [42].

### 2.6.3 Detector Simulation

Once the initial interaction has been simulated, it is necessary to simulate the passage of the particles through the material of NOMAD. This simulation needs to include both the behaviour of the particles (such as multiple scattering, energy loss and decay) and the response of the detectors to the passage of these particles.

This task is performed in the GENOM [39] program, which is a specific implementation of the NOMAD detector in the general purpose simulation

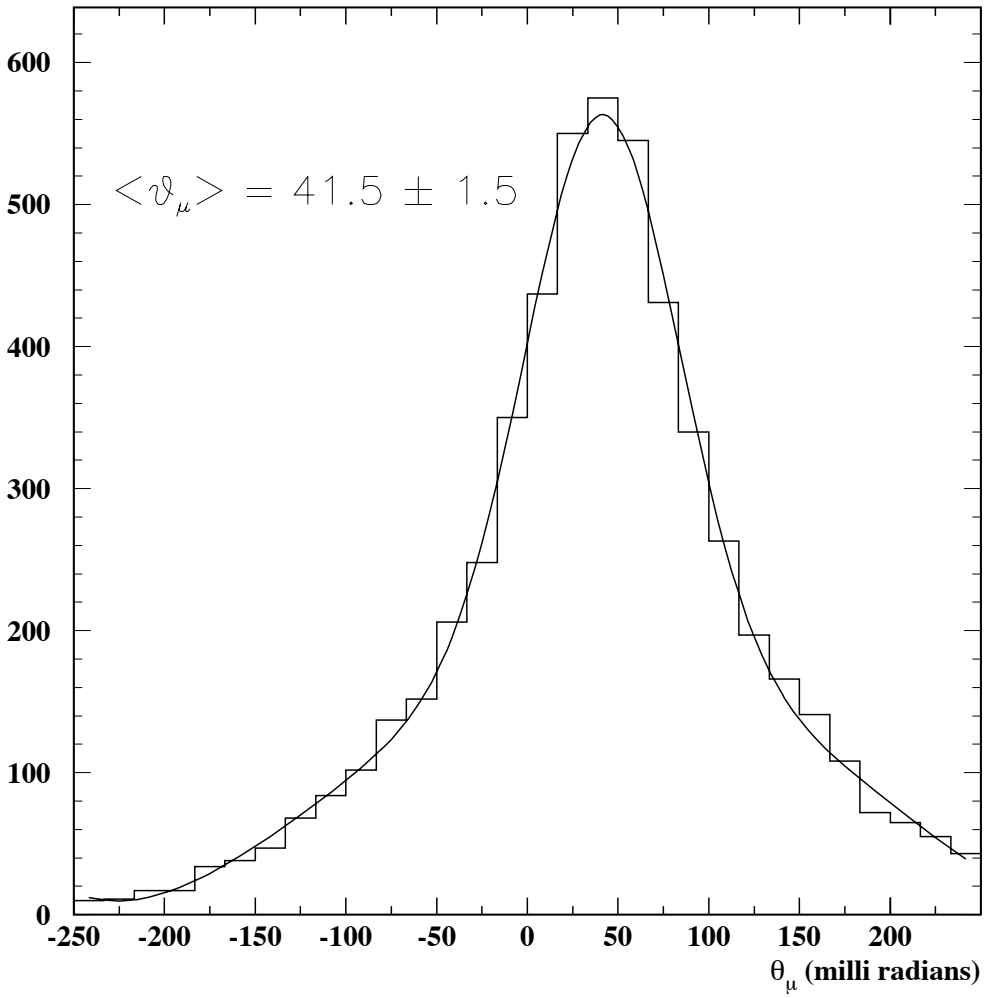


Figure 2.15: Distribution of the reconstructed angle in the YZ plane of the leading $\mu^{\pm}$ in reconstructed $\nu_\mu$ and $\overline{\nu_\mu}$ charged current events from the 1998 STAR data.

package GEANT [40]. The detector simulation includes the production of data in the same format as that recorded by the data acquisition for subsequent reconstruction and analysis.

### 2.6.4 Event Reconstruction

Event reconstruction in NOMAD is based on the tracking provided by the drift chambers. The framework for the reconstruction is a package known as "engine" which drives the reconstruction of each subdetector and the subsequent matching of information between subdetectors. This process occurs in three stages. At each stage, every subdetector is able to perform whatever reconstruction is necessary through a call to a subroutine specific to that subdetector.

In the first stage, the event is read into memory and each subdetector extracts the information relevant to that subdetector. The triplets, consisting of one wire in each of the three orientations ($0^\circ$ and $\pm 5^\circ$) are reconstructed in the drift chambers and will be the basis for the track reconstruction in the next stage. Short tracks known as stubs are reconstructed in the muon chambers.

The second stage sees the reconstruction of tracks and then vertices in the drift chambers. A Kalman filter is used to fully reconstruct tracks in the drift chambers based on the triplets previously reconstructed. The drift chamber tracks (DcTracks) are then used to reconstruct vertices inside the drift chambers and to determine the position of the neutrino interaction (the primary vertex).

The final stage is the matching between the drift chambers and the other detectors. In this stage, particle identification information from the transition radiation detector, preshower and electromagnetic calorimeter is used to separate electrons and pions and to positively identify them as such. Clusters in the calorimeter that are not matched to a drift chamber track (known as "neutral clusters") are treated as photons originating from the primary vertex. Stubs in the muon chambers are matched to drift chamber tracks and compared with energy deposited in the calorimeters to identify any muons that may be in the event.

In the normal NOMAD reconstruction, all the information obtained in this process would then be stored in a Data Summary Tape (DST) [48] which includes the Monte Carlo information (if applicable) as well as the reconstructed tracks, vertices, particle identification and information from each of the matched subdetectors.

The data used in this thesis, however required different reconstruction due to the addition of a second tracking detector (STAR) which will be discussed

in the following chapters.

# Chapter 3

# The STAR upgrade

## 3.1 Introduction

In order to test the NAUSICAA proposal, the STAR (Silicon TARget) detector was constructed and installed inside the NOMAD magnet in April 1997. The associated support structures of the first three drift chambers were removed to accomodate the detector (Figure 3.1). At the same time, two passive targets were installed below STAR in order to study the effects of nuclear reinteractions of the final state products of neutrino interactions (see Fig. 3.1).

## 3.2 The STAR detector

The assembly of a single module (or ladder) of the STAR detector is shown in Fig. 3.2

A STAR ladder consists of 12 Hamamatsu detectors (see Fig. 3.3) glued to a kapton foil which insulates them from a carbon-fibre support 0.5cm thick. The silicon detectors measure $33.5mm \times 59.9mm \times 300\mu m$, and have 641 readout strips with a pitch of $50\mu m$. Floating strips are evenly spaced between the readout strips.

The ladders are read out by 5 VA1 chips which are mounted on a printed circuit board. Each VA1 chip has 128 charge-sensitive low-power low-noise amplifiers and so only 640 of the strips are read out [1], [14].

Each of the 640 readout strips in a detector are bonded to the corresponding strip in the neighbouring detector and finally to the VA1 chips whose output is passed to a repeater board which drives clock signals, and allows control of the operation of the VA1 chip.

The analog signals are readout by CAEN model V 550 10 bit ADCs.

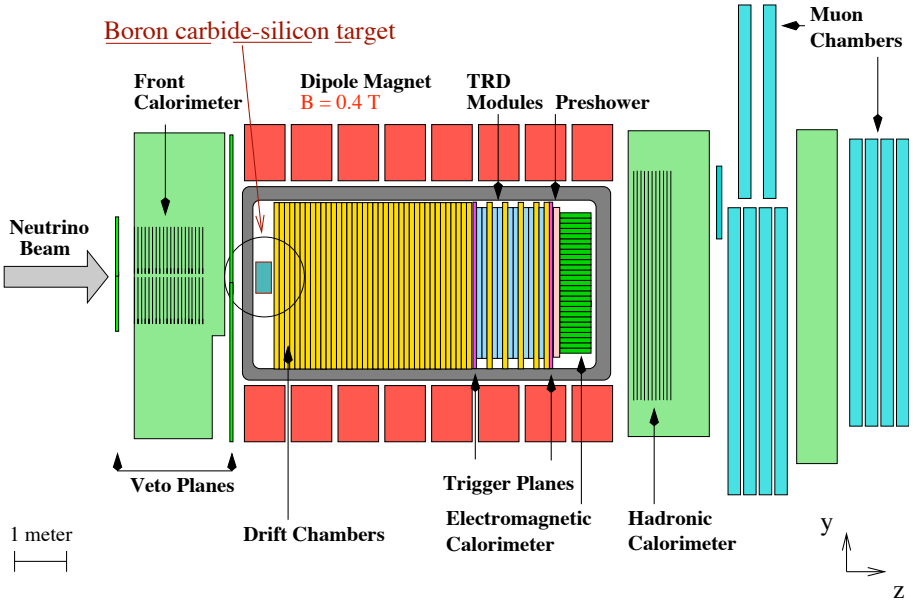


Figure 3.1: Position of the STAR detector within NOMAD

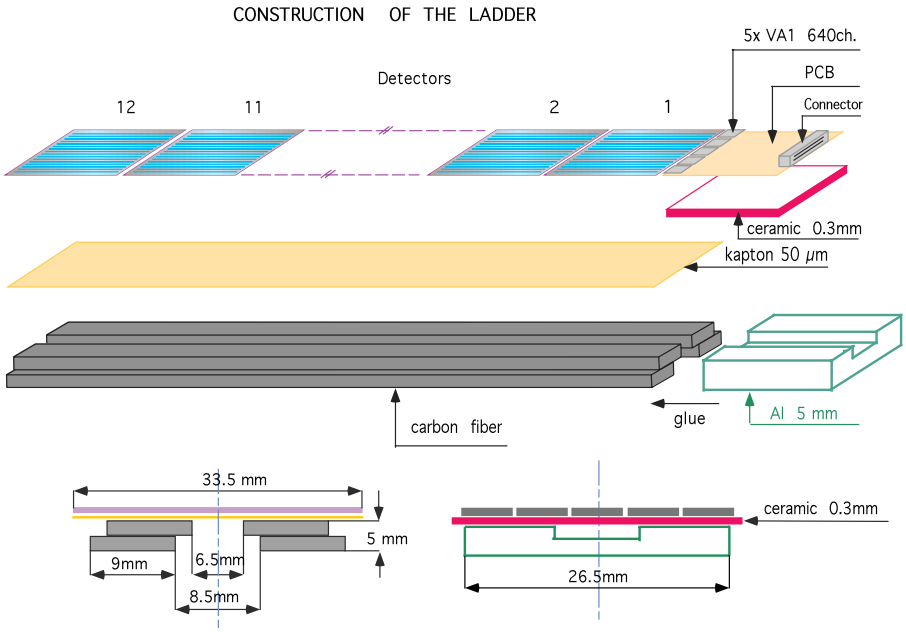


Figure 3.2: Construction of a STAR Ladder

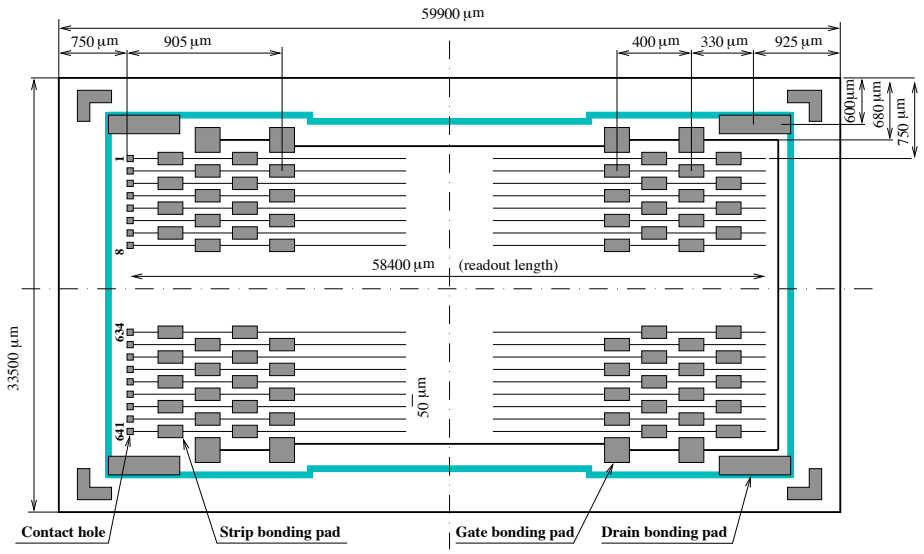


Figure 3.3: A Hamamatsu silicon detector

A layer (or plane) of detectors is composed of 10 ladders orientated such that the silicon strips are parallel to the magnetic field, which corresponds to the X axis in the NOMAD coordinate system (the X axis is parallel to the magnetic field, the Y axis points upwards and the Z axis is at an angle of $43mrad$ with respect to the beam). In order to obtain full coverage in the Y direction, each ladder slightly overlaps with its neighbour. The result is an active surface of $72 \times 31.5cm^2$ (see Fig. 3.4).

The passive target of STAR consists of 4 blocks of $B_4C$ with dimensions of $72 \times 31.5 \times 2cm^3$ and a total mass of 45 kg. Each block is separated by $3.6cm$ and is followed by a plane of detectors. A further plane follows the $4^{th}$ block of $B_4C$ to allow reconstruction of tracks originating in that block (see Fig. 3.5) giving a total of 5 planes of silicon detector. The passive target was chosen as the best compromise between maximum density ( $2.49gcm^{-3}$) and hence number of neutrino interactions, and minimum radiation length ($21.9cm$) and hence multiple scattering [1].

A single $B_4C$ layer contains 0.06 interactions lengths and 0.09 radiation lengths.

A full layer of target, detector and support structure contains an average of between 0.04 and 0.05 radiation lengths.

In order to provide a specific trigger for interactions inside the STAR

[1]For example, Carbon Fibre has a density of around $2.2gcm^{-3}$ and radiation length of $18.8cm$

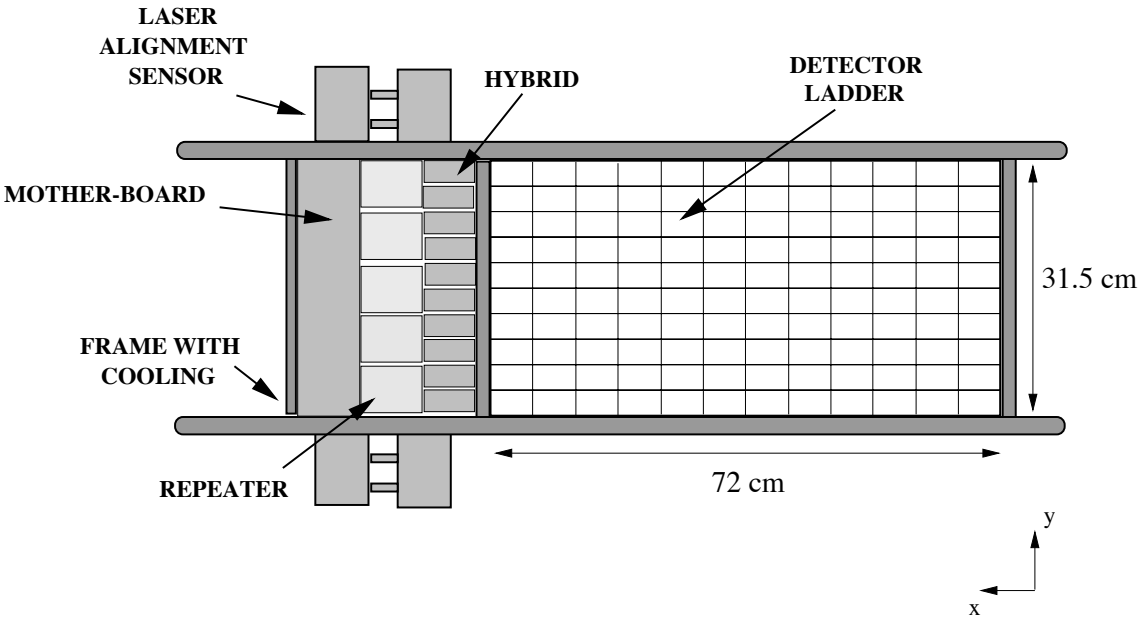


Figure 3.4: Construction of a STAR Plane

volume, two planes of scintillator were placed in front of and behind the detector. The front ($V_s$) pair are $1cm$ thick while the rear pair ($T_s$) are $0.5cm$ thick. Two triggers were added to the NOMAD DAQ system to allow the readout of STAR.

A coincidence of the NOMAD veto plane 8, the STAR veto, the STAR trigger and NOMAD trigger plane 1 ($V_8 V_s T_s T_1$) during the muon-gate causes the detector to be read out. This condition was named STAR-MU and allowed flat-top muons passing through the detector to be recorded.

During the neutrino gates ($\nu_1$ and $\nu_2$) the STAR trigger consisted of the anti-coincidence of veto plane 8 and the STAR veto with a coincidence of the STAR trigger and NOMAD trigger plane 1 ($\overline{V_8 V_s} T_s T_1$). This condition was named STAR-NU and allows the selection of neutrino interactions inside the STAR target.

To allow the detector to be aligned with the maximum precision, a pulley system was incorporated into the support structure (see Fig. 3.6) allowing the $B_4C$ to be raised above the level of the silicon detectors. The multiple scattering experienced by the flat-top muons used for the alignment is thus minimised.

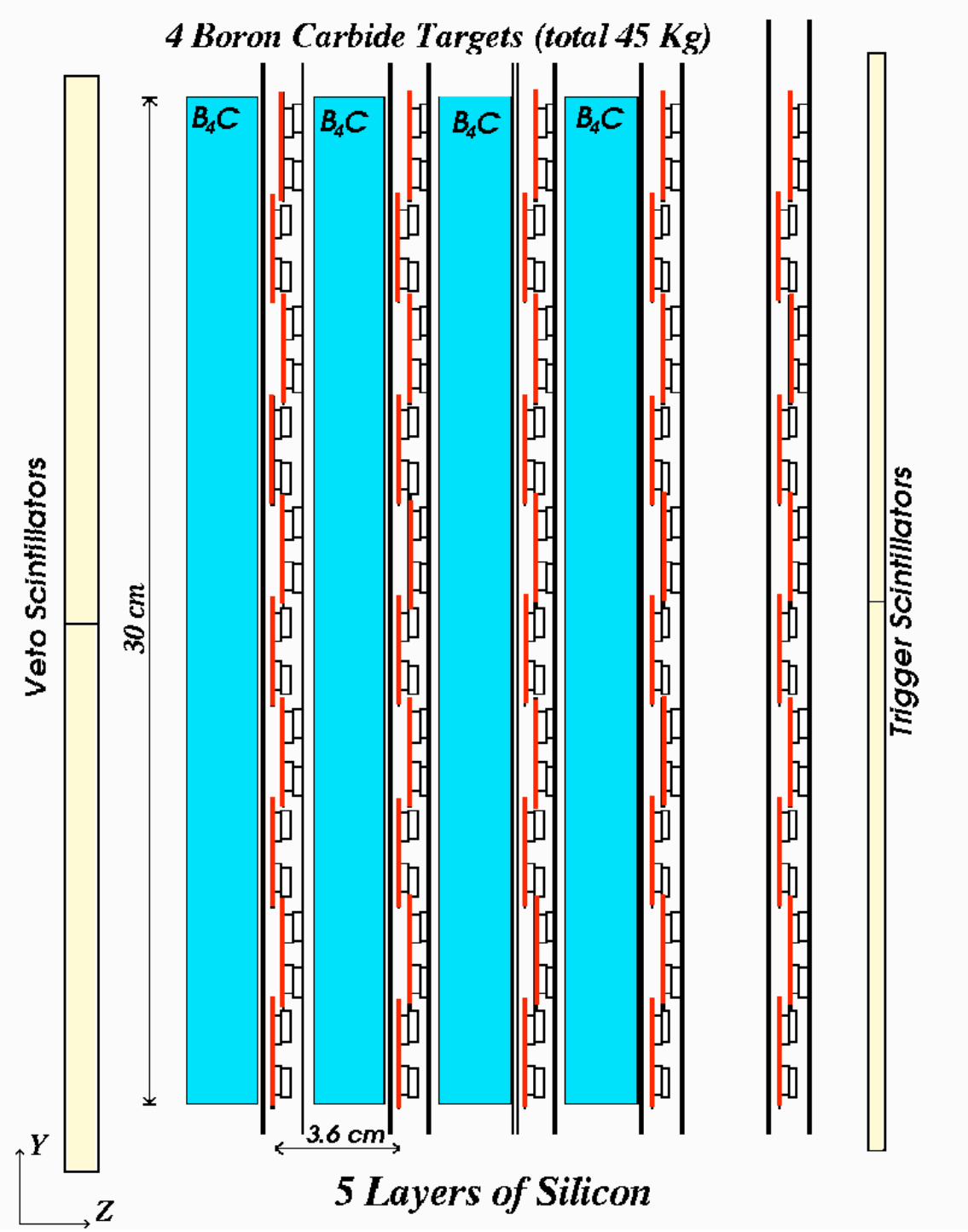


Figure 3.5: Side view of the full STAR detector

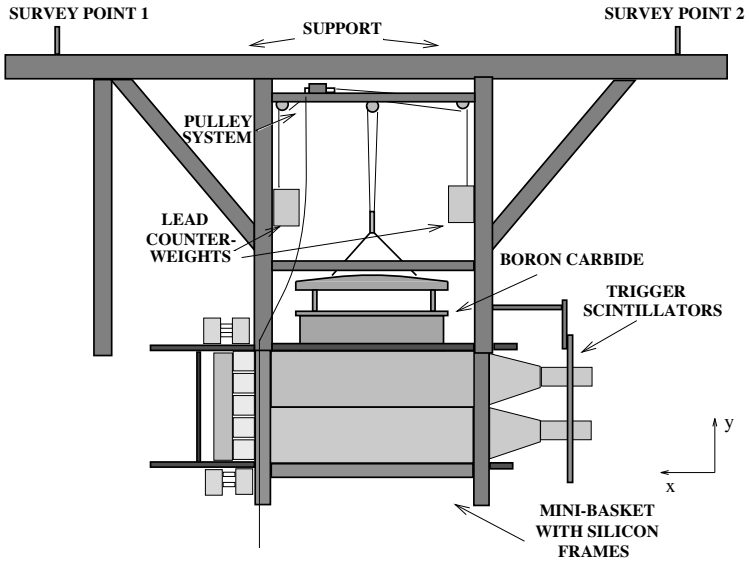


Figure 3.6: Support system for STAR

## 3.3 Alignment of the detector

The initial stage in the determination of the exact locations of each silicon detector was a survey of each ladder conducted prior to the final assembly and installation of STAR [34]. This survey was performed with a CCD camera and magnifying optics which were mounted on a table. The silicon layer undergoing measurement was secured vertically with the detectors facing the camera. The layer remained fixed and the camera was moved independently in each of the three axial directions by stepping motors (see Fig. 3.7).

The position encoders were able to measure the position of the camera with a precision of approximately $1\mu m$. However the overall precision was degraded by the image quality and precision of the stepper motors. A PC was used to read the position and store this information. To measure the X and Y coordinates, the camera was positioned over and focussed on a reference feature on the surface of the detector (a specific corner of a bonding pad on either read-out strip 40 or 600). In order to measure the Z position, a red laser, oriented at 45° to the camera, was focused on the surface to be measured. A spot could be seen on the monitor if the laser light reflected diffusely from an aluminized surface of the detector. The camera was adjusted in the Z-direction so that the centre of the laser spot coincided with a crosshair on the monitor screen. The crosshair was adjusted a priori so that

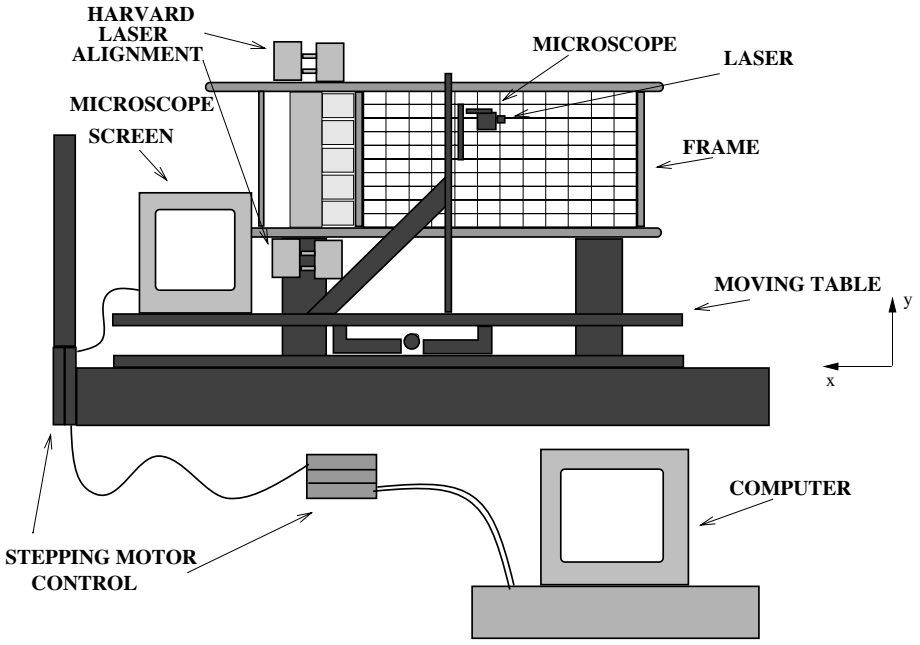


Figure 3.7: Survey of a STAR plane

the camera was in focus when the laser spot hit it.

For each detector, a total of 4 points were measured, resulting in 48 points per ladder. The bottom left corners of the inner bonding pads on strips 40 and 600 were used for this. Each ladder was surveyed by at least two people to test for any systematic errors and to check for mistakes.

Figure 3.8 shows the histograms of the differences in the X, Y and Z measurements performed by each operator for all ladders. It was found that the measurements were repeatable to within 6.4 $\mu$m in the X–axis, 6.6 $\mu$m in the Y–axis and 14 $\mu$m in the Z–axis.

As each layer was added to the mini-basket, the layer was surveyed again to allow the relative positions of each layer (and hence each detector) to be determined. Due to constraints imposed by the camera system, only detectors 4 through 8 were measured in each of ladders 1 through 9. For ladder 10 only the bottom row of the ladder was visible and hence less information was recorded. By comparison of the plane by plane survey to the survey completed inside the minibasket the separation of each detector with respect to reference points on the mini-basket was established.

Once STAR was installed inside NOMAD, the reference points were measured by surveyors and these positions were used to convert the surveyed

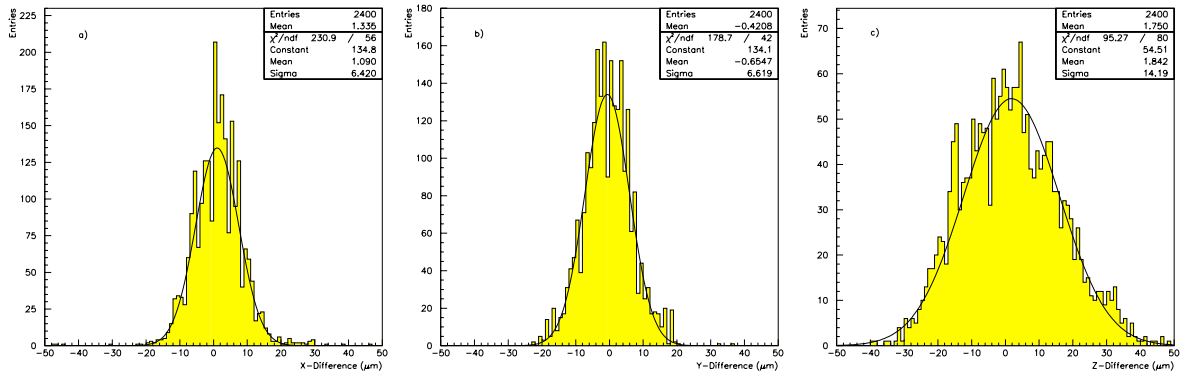


Figure 3.8: Systematic differences in the (a) X, (b) Y and (c) Z position measurements for all operators of the surveying system.

detector positions into the NOMAD coordinate system. This initial survey was used as the starting point for the in-situ alignment performed using high momentum muons.

## 3.4 Neutrino interactions in STAR

The STAR detector was deliberately located below the Z axis at the front of the Drift Chambers, so that the centre of the neutrino beam would pass through it.

The NUBEAM [44] package was used to determine the flux and average energies of the 4 species of neutrino passing through STAR. The concentration and average energy of $\nu_\mu$ $\overline{\nu_\mu}$ $\nu_e$ and $\overline{\nu_e}$ are shown in table 3.1

| Neutrino | Average Energy (GeV) | Concentration (%) |
|---|---|---|
| $\nu_\mu$ | 30.60 | 94.12 |
| $\overline{\nu_\mu}$ | 19.83 | 5.02 |
| $\nu_e$ | 42.18 | 0.69 |
| $\overline{\nu_e}$ | 31.11 | 0.17 |

Table 3.1: NUBEAM predictions for the STAR target

Figure 3.9 shows the predicted neutrino spectrum at STAR.

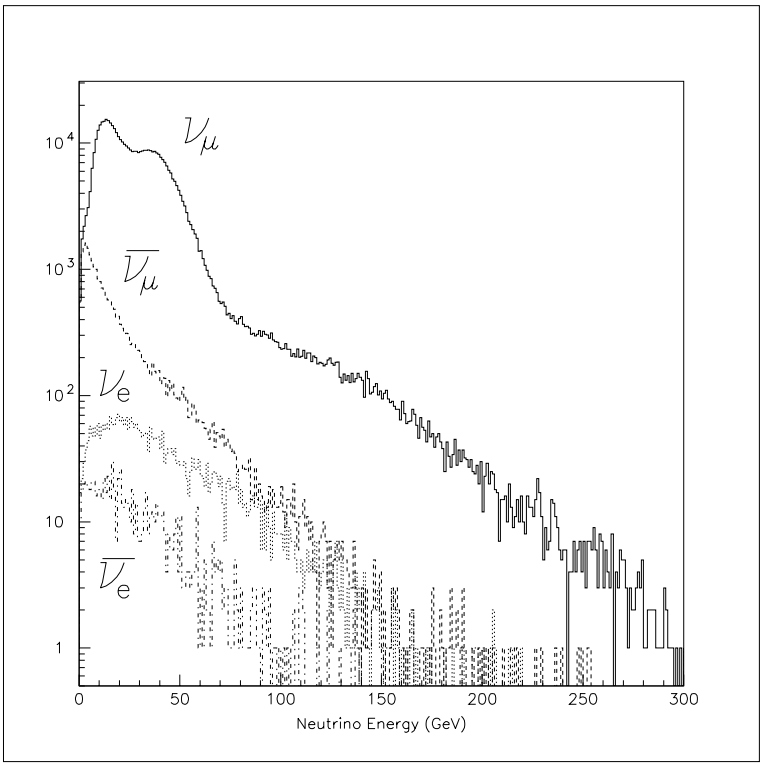


Figure 3.9: The Neutrino Spectrum at STAR as predicted by NUBEAM

# Chapter 4

# Silicon Hit Reconstruction

## 4.1 Introduction

On passing through a silicon detector, charged particles produce a series of electron-hole pairs in the material. A typical minimum ionising particle will deposit approximately $80keV$ (known as a MIP) in a silicon detector. In order to produce a single electron-hole pair, $3.6eV$ is required, thus a MIP will result in the production of approximately 25000 electron-hole pairs in the detector.

Through the electric field produced by the bias voltage, charge is collected on the read-out strips. Due to the scale of the ionisation and charge transport within the silicon, charge is not confined to just one strip, but is distributed over a number of strips. The floating strips help to collect some of this charge, through capacitive coupling to the readout strips. This allows more charge sharing between the readout strips and thus a greater precision in the determination of the hit position.

This fact is used in the pattern recognition of good hits. As the signal of a charged particle is actually a collection (or cluster) of strips with charge, an algorithm, described below, is implemented to use all the available information.

## 4.2 Common Mode Noise subtraction

A number of corrections need to be applied to the ADC readings so that they may be used to search for hits in STAR.

At any given moment during the data-taking process, an individual strip will be read-out with a certain ADC level, even when there was no hit in that region of the detector. This average value is referred to as a pedestal level.

During the data-taking period, on-line software measured the ADC values returned by each of the 32000 strips during the calibration period which occurs at the end of the neutrino beam extractions. By accumulating a large number of such measurements, the average pedestal value was calculated for each strip and stored in a database. At the end of a run of data-taking, this database was transferred to the STAR data-acquisition system. This pedestal information was stored in the VA1 read-out chips [12] and automatically subtracted from the ADC values recorded. An extra feature of the DAQ was zero-suppression in which strips whose pedestal-subtracted ADC was exactly equal to zero were not recorded. These strips have exactly the pedestal level and so are unlikely to be involved in a good hit. This allowed a reduction in the amount of space taken up by the data recorded by STAR. Due to the fact that only strips with a pedestal-subtracted value of exactly zero were subtracted, it is possible to recover this information during off-line processing as these are the only strips without a record.

The same on-line program that calculated the pedestals also calculated the RMS of the ADC recorded on each strip allowing a check of the performance of the detector. During a similar process performed off-line, the average noise value was calculated for each strip for each day of data-taking and stored in a database.

This value of noise was specific to each strip and is used in the reconstruction process to define the signal/noise ratio on that strip.

Typical values for the pedestal on a strip ranged between 150 and 450 ADC counts.

The typical RMS noise measured ranged between 6 ADC counts for good strips and reached as much as 20 ADC counts for noisy strips.

A second form of noise is a result of the read-out chips rather than the strips. This noise is common to each of the 128 strips read-out by a given VA1 chip and is therefore known as Common Mode Noise.

Common Mode Noise (CMN) is calculated on an event by event basis during the event reconstruction and subtracted by each chip before the search for hits begins.

The procedure for calculating CMN starts by first calculating the average value of each strip on a chip by chip basis. This average is then recalculated excluding any strips whose ADC value is more than $3\sigma$ away from the previously calculated average. The reason for this second step is to remove from the average, as far as possible, any large values which actually correspond to a hit.

Once the averages have been calculated for each strip connected to a given chip, the ADC values of every strip on that chip are reduced by the value of the average, which is the CMN.

Figure 4.1 shows the distribution of common mode noise for all chips in the 1998 data and the noise as a function of chip.

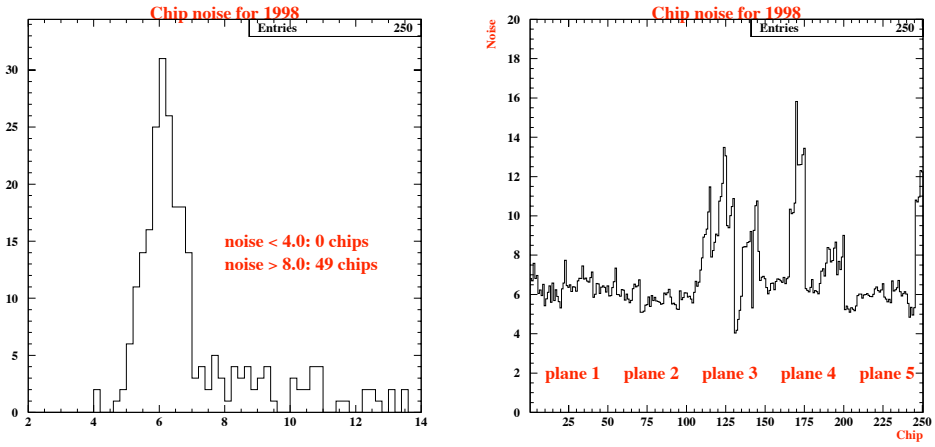


(a) Distribution of CMN (in ADC counts)

(b) CMN (in ADC counts) per chip

Figure 4.1: Common mode noise in STAR during the 1998 run.

## 4.3 Formation of Clusters

The search for hits in STAR starts with a search for "seed" strips. A cluster of charge deposition will be marked by at least one strip on which a very high amount of charge was deposited. A signal/noise threshold was chosen on a ladder by ladder basis, and any strips whose signal/noise exceeded this value are designated seed strips.

Because some clusters may contain more than one strip that exceeds this cut, a test is made on all seed strips to remove those that are neighbours of another with a higher value of signal/noise.

The second phase in the process is to define a lower cut, again on a ladder by ladder basis, that selects strips which are part of the overall cluster. The strips neighbouring each seed strip are tested against this cut, and those that survive are collected into a cluster with the seed hit.

The final stage is to find the total signal/noise of the clusters that have been formed and remove any that do not exceed a third cut which is also

| Seed Cut | Neighbour Cut | Cluster Cut |
|---|---|---|
| 4.0 | 1.0 | 6.0 |

Table 4.1: Signal/Noise cuts used to reconstruct hits in Monte Carlo

applied on a ladder by ladder basis.

The total signal to noise is defined as the sum of the signal to noise of each hit in the cluster.

This process is illustrated in Fig 4.2.

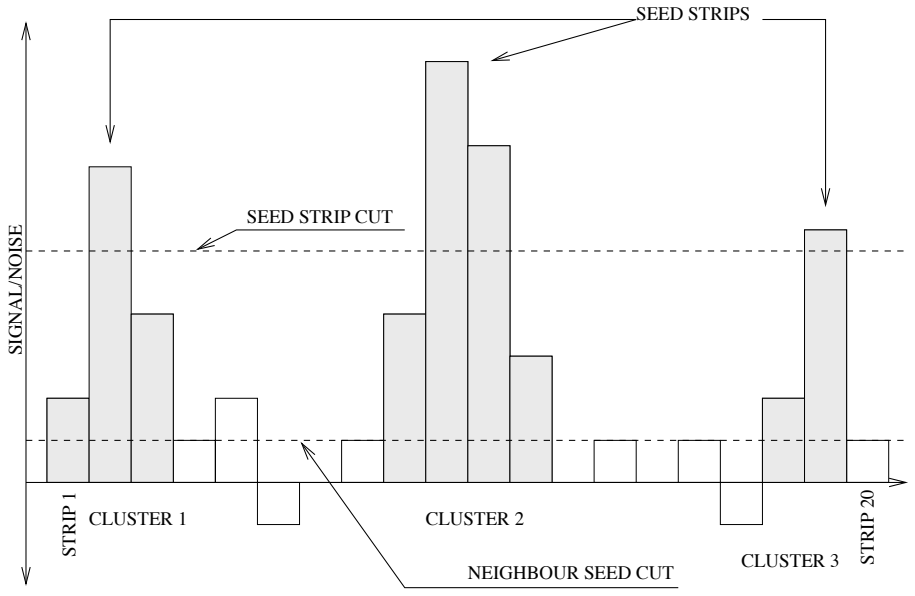


Figure 4.2: Illustration of cluster search algorithm

The values of the cuts described above have to be chosen with some care, as lowering the values too much allows noise to be mistakenly reconstructed as a hit, while raising cuts too high results in the loss of good hits.

In the Monte Carlo, all detectors were modelled as being identical, and so the cuts defined in Table 4.1 were used for all ladders.

When this was applied to the data, it was found that the different ladders in STAR behaved quite differently and so it was necessary to determine optimum cuts separately for each ladder. A study was conducted of the hit finding efficiency as a function of the three cuts on a ladder by ladder basis using single muons passing completely through STAR recorded during the muon gate [49].

The optimised cuts are shown for each ladder in figure 4.3

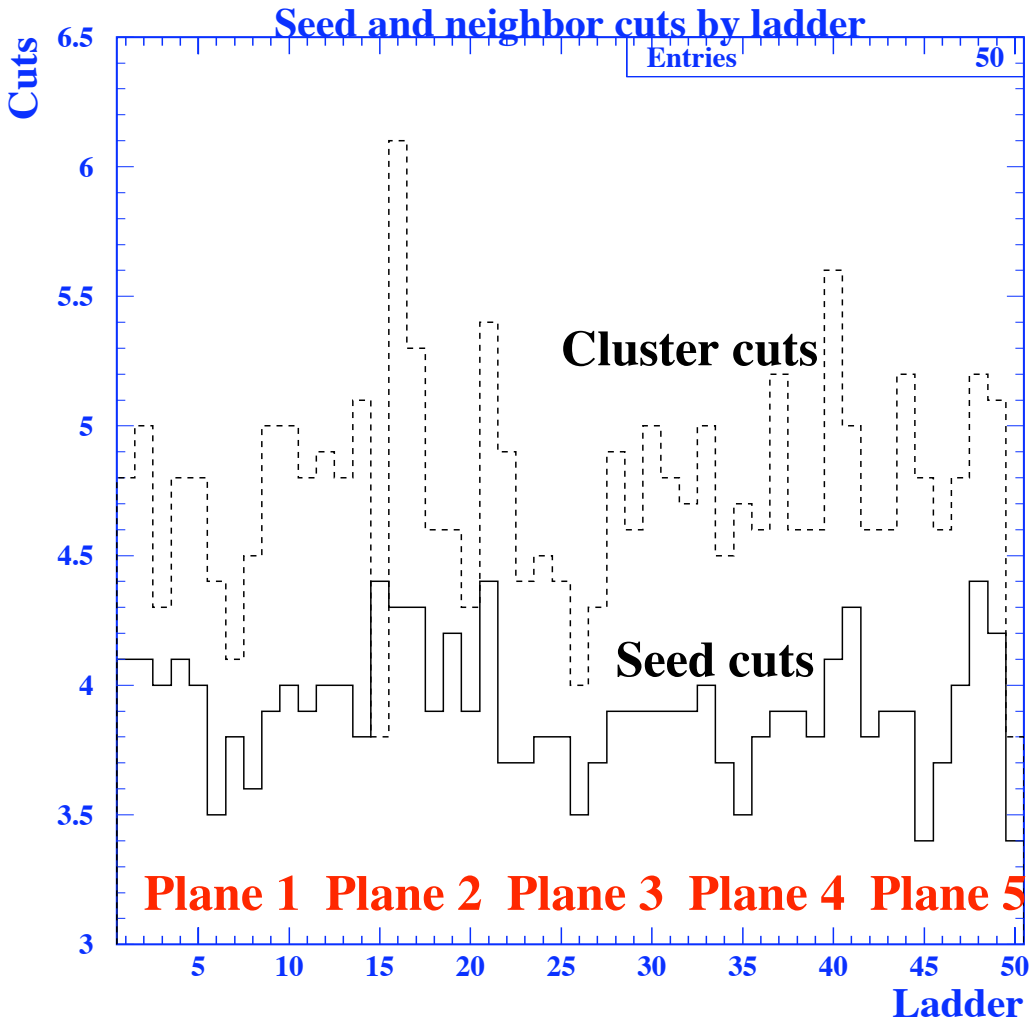


Figure 4.3: Cuts used for reconstructing silicon hits in the data.

These values are also presented in Tables B.1 - B.5.

As a result of this optimisation, the efficiency for finding hits was substantially improved over the simpler method of using fixed cuts for each ladder. A comparison of the hit finding efficiency before and after the optimisation is shown in figure 4.4.

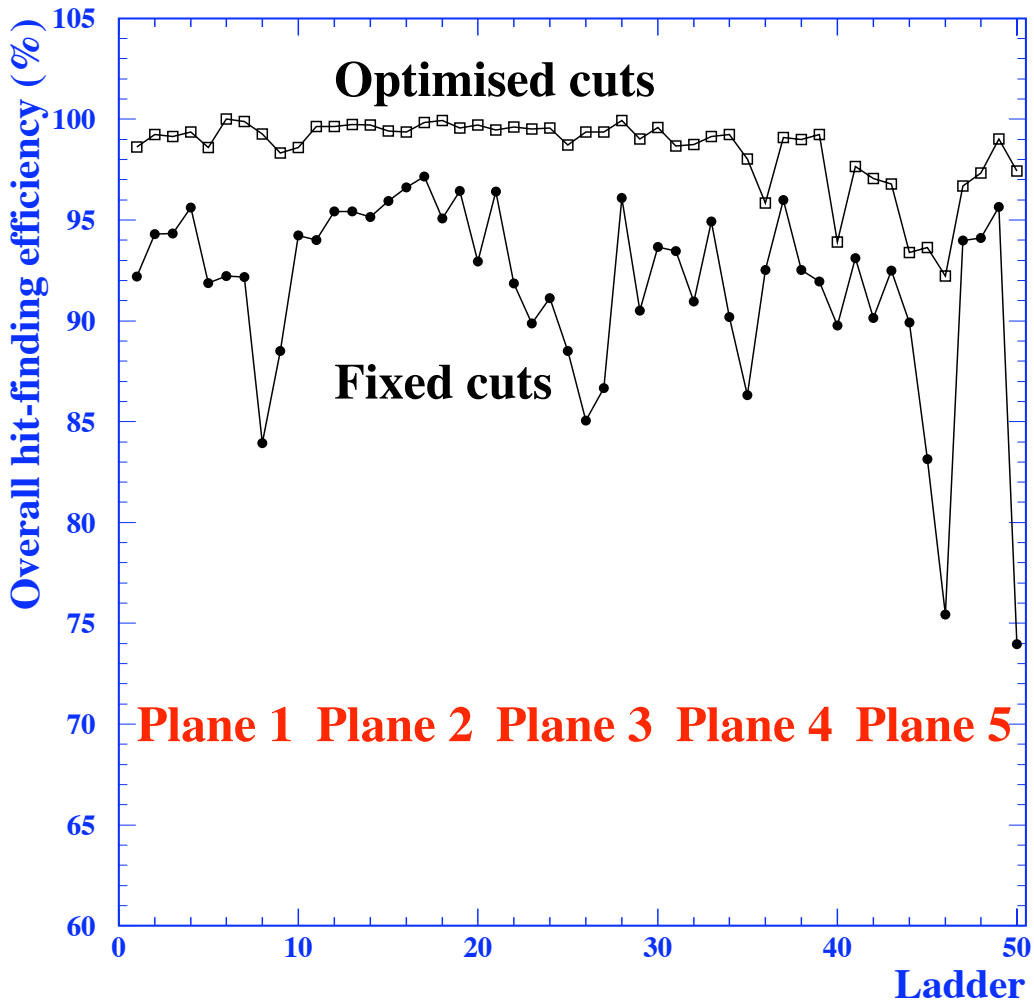


Figure 4.4: Efficiency for reconstructing hits using fixed cuts and optimised cuts.

The effects of these cuts can be seen when silicon hits reconstructed from data and Monte Carlo are compared.

The total number of strips per cluster is shown in Figure 4.5. The real data shows a slightly greater number of strips per cluster on average due to the relaxing of the cluster signal to noise cut and due to not including noisy strips in the simulation.

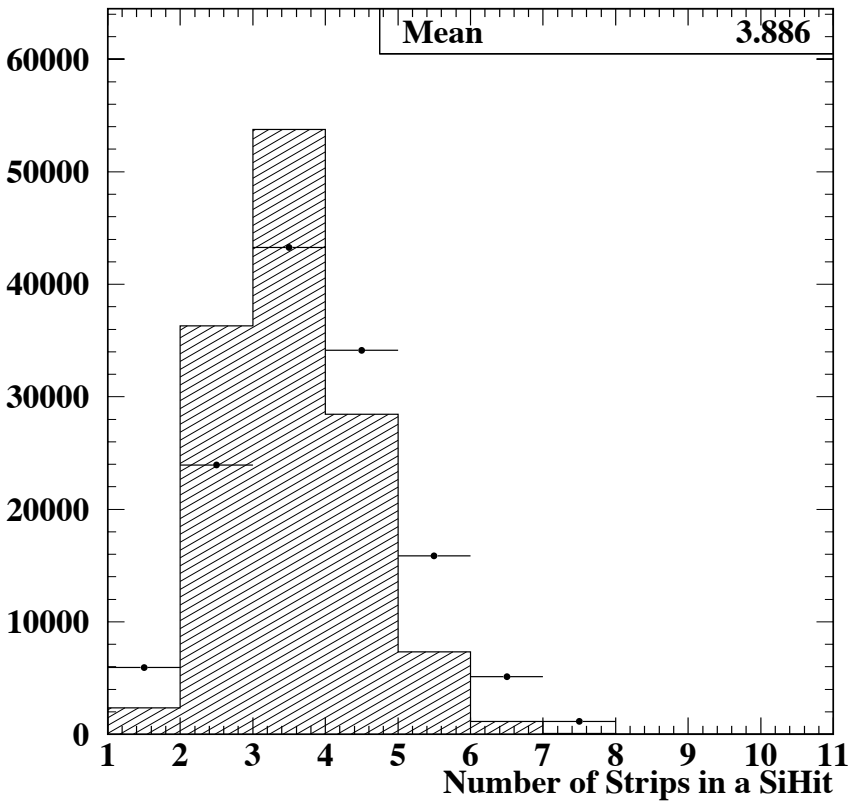


Figure 4.5: Number of strips in a cluster. The data points are overlayed on the Monte Carlo histogram which has been normalised to the data.

The total charge collected in a cluster is shown in Figure 4.6. The total signal/noise for a cluster is shown in Figure 4.7. There are more clusters with a low total charge and signal to noise due to the lower seed and cluster signal to noise cuts and the possible use of noisy strips to create a cluster.

Now that a technique for defining clusters in STAR has been refined, we

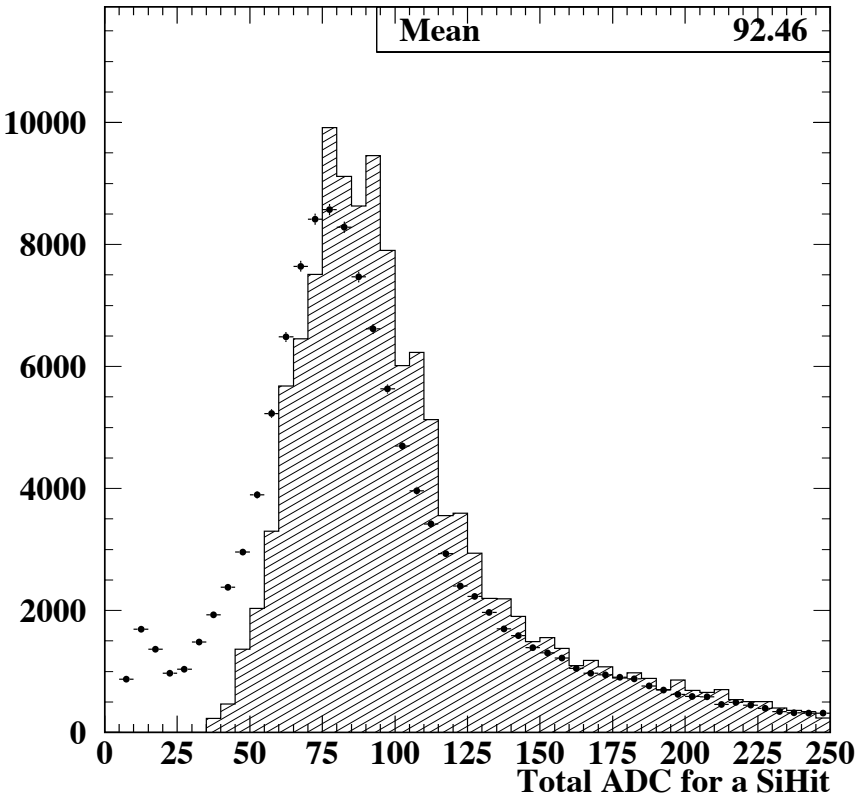


Figure 4.6: Total charge in units of ADC counts deposited in a cluster. The data points are overlayed on the Monte Carlo histogram which has been normalised to the data.

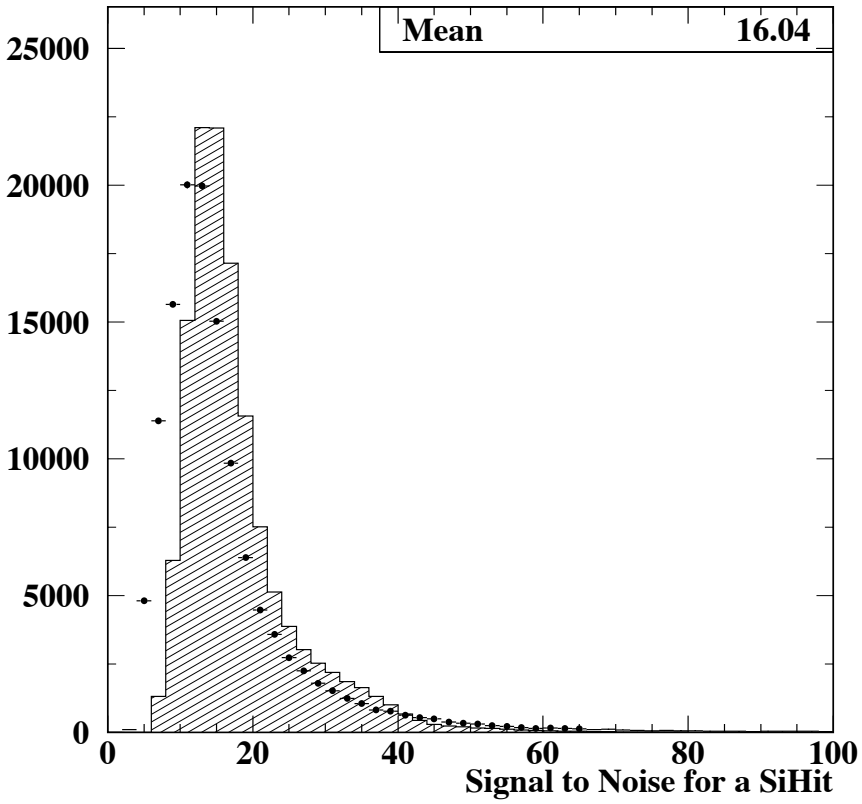


Figure 4.7: Total Signal to Noise distribution in a cluster. The data points are overlayed on the Monte Carlo histogram which has been normalised to the data.

are in a position to consider the process of track reconstruction, which will be addressed in the following chapter.

# Chapter 5

# Track Reconstruction

## 5.1 Introduction

Once the individual hits in STAR have been reconstructed, it is neccesary to identify which hits correspond to which track. Due to the lack of any information in the X-direction, it is necessary to extrapolate already reconstructed tracks in the drift chambers into STAR and use this information to both allocate hits to a given track and determine the optimum position of each hit. Once this information is obtained, the STAR hits can be fit in the Y-Z plane to provide optimum track parameters inside the detector.

## 5.2 Pattern Recognition

The pattern recognition process involves identifying which hits in STAR correspond to a given track in the drift chambers. In order to minimise incorrect associations due to uncertainty in track parameters and multiple scattering in the $B_4C$, two cuts are implemented to select suitable drift chamber tracks (DcTracks). The DcTrack must have a reconstructed momentum of more than 150MeV, and the most upstream hit of the track must have a Z position of less than $100cm$.

For all DcTracks passing these cuts, an iterative procedure is followed, starting with those ladders of plane 5 closest to the drift chambers.

Each DcTrack is extrapolated to the position of that plane of detectors and the extrapolated position in X is tested to check that it lies within the active volume of STAR. The extrapolated position in Y is then tested against each hit in STAR (SiHit).

A simple procedure would then be to assign the SiHit that is closest to each DcTrack to that track. However due to the range of momenta involved

and the corresponding variation in multiple scattering, this can result in a significant rate of mis-identification. The solution is to, instead, measure the difference in Y divided by the approximate uncertainty due to multiple scattering as measured from the DcTrack and the material the track travelled through. These differences are then accumulated for each different plausible combination of assigning hits to tracks. The combination with the lowest overall "cost" is then chosen.

The next stage is a repeat of the procedure carried out on the remaining ladders of plane 5, followed by each half of plane 4 and so on to plane 1.

Once a single SiHit has been associated to a DcTrack, its position can be determined more accurately (see below) and then this position can be used as the starting point of the extrapolation. In this manner, the accuracy of the hit assignment is not degraded by the significant quantity of material that exists between planes 1 and 4.

The extrapolation is improved further once 2 hits are associated to a DcTrack, the two accurate positions in Y and Z are used in conjunction with the measurement of the momentum of the track from the drift chambers to continue the extrapolation towards the FCAL.

In order to further minimise incorrect associations, a test is made on the X position of the extrapolation of the DcTrack to the detector under consideration. If the X position corresponds to an active region of silicon, then the association of a SiHit with that DcTrack will be allowed. This can result in a DcTrack not being associated to hits in one or more planes as the track was passing through an inactive region of the detector at that point. The final check is that if the track has passed through an active region, then it should have had a hit associated to it. A count is kept of the number of unexplained (in terms of the active area) holes (that is planes where a hit is expected but was not found) and once a track exceeds 1 unexplained hole, the extrapolation process for that track is stopped.

## 5.3 Fine Tuning of Hit Position

As each detector in a given ladder is bonded to its neighbour, a ladder is effectively one long strip, with inactive regions due to the bonding pads, approximately $72cm$ long. It was not possible to attach each of the detectors to the support structure such that each strip is aligned exactly with the corresponding strip on the other detectors. For this reason, it is necessary to work out which detector a signal came from, in order to determine the exact Y and Z positions of the strips in that detector.

By extrapolating the DcTrack associated to a given hit to the Z position

of the detector, the approximate X position of the track can be determined. By looking up the database of detector positions determined by the survey and subsequent alignment, the exact positions of the ends of each strip can then be determined.

Once the positions of each strip in a cluster are known precisely, the amount of charge deposited can be used to determine where, in relation to the strips, the particle passed.

The algorithm used to reconstruct the precise location of the hit was described in detail as "Algorithm C" in [1]. In this algorithm, 8 strips are considered on each side of the seed strip and the charge collected on each is taken into account. Some charge will be shared by the readout and floating strips as well as with the backplane. The hit position is assumed to be somewhere between a readout and a floating strip and the charge distribution on each strip is optimised via a chi-square minimisation to determine the position of the hit.

This position is determined as a fraction of the distance from the readout to the floating strip which is subsequently converted into y and z positions through the database of strip positions.

## 5.4 Kalman Track Filter

The Kalman filter is the optimal estimator of the state vector of a linear dynamical system, since it minimizes the mean square estimation error [15, 16]. This has been widely used in High Energy physics tracking applications [17–25].

A track in space can be described by its 5-dimensional state vector $\mathbf{x} = (x, y, dx/dz, dy/dz, 1/p)$, where $x$, $y$ and $z$ are the spatial coordinates and $p$ is its momentum, at each of the measurement points, defined by their $z$ coordinate along its trajectory. In its linear form, the evolution of the state vector is described by the discrete system of linear equations:

$$\mathbf{x}(z_k) \equiv \mathbf{x}_k = \mathbf{F}_{k-1}\mathbf{x}_{k-1} + \omega_{k-1}, \tag{5.1}$$

which defines the change in status of this vector based on the previous measurement point $\mathbf{x}_{k-1}$. The function $\mathbf{F}_{k-1}$ is the track propagator from measurement $k-1$ to measurement $k$ and the random variable $\omega_{k-1}$ describes the random noise of the system (also called process noise). In the tracking of particles through dense media, the process noise can be due to multiple scattering, energy loss or any other physical process that might disturb the particle trajectory.

The actual measurements $\mathbf{m}_k$ carried out at each of the measurement points are a function of the state vector:

$$\mathbf{m}_k = \mathbf{H}_k \mathbf{x}_k + \epsilon_k, \tag{5.2}$$

where $\mathbf{H}_k$ describes the relationship between the measured quantities and the state vector and $\epsilon_k$ describes the measurement noise.

The Kalman filter proceeds by performing these three distinct operations:

- *Prediction*, where the status of the state vector is estimated at a future measurement point;
- *Filtering*, where the current estimation of the state vector is carried out based on the previous measurements; and
- *Smoothing*, where the estimation of the state vector at a previous measurement is re-evaluated with the new information of the present measurement.

These operations will be followed in the description of the application of the Kalman filter to the NOMAD-STAR detector.

### 5.4.1 Trajectories of particles in a magnetic field

The trajectory of a particle inside a constant magnetic field is a helix. Assuming that the magnetic field $B$ (in Tesla) is parallel to the $x$ coordinate, and using the $z$ coordinate as a parameter, then:

$$\rho \equiv \frac{y''[z]}{[1+(y'[z])^2]^{3/2}} = \frac{q\,B\,0.3}{p_\perp} \quad , \tag{5.3}$$

$$x''[z] = 0 \quad , \tag{5.4}$$

where $\rho = 1/R$ is the curvature, $R$ the radius of curvature (in meters), $q$ the charge of the particle and $p_\perp = \sqrt{p_y^2 + p_z^2}$ the transverse momentum to the magnetic field (in GeV). The solutions to these equations are:

$$y = y_c - \tilde{q}\sqrt{R^2 - (z - z_c)^2} \quad , \tag{5.5}$$

$$x = a_x + b_x z \quad , \tag{5.6}$$

which represent the parametric equations of a helix using the $z$ coordinate as a parameter ($a_x$ and $b_x$ being fit parameters). The $xz$ projection (Eq. 5.6) is a straight line and the $yz$ projection a circle (Eq. 5.5), with ($y_c$,$z_c$) the center of the circle, R its radius and $\tilde{q} = q/|q|$ the sign of the charge of the

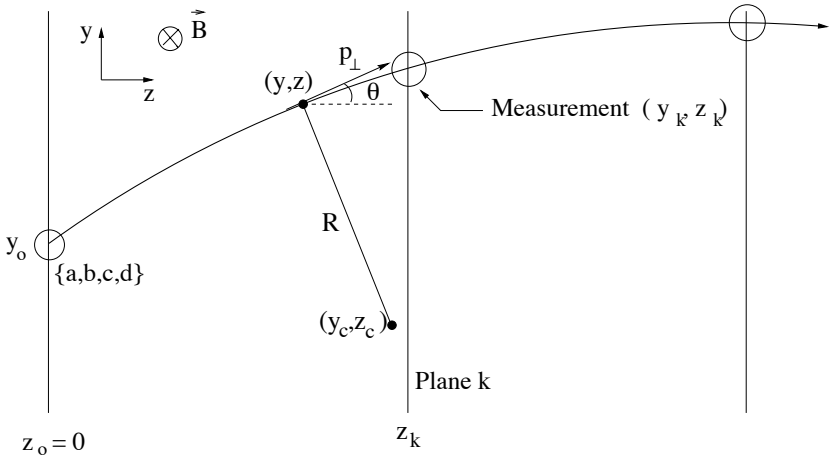


Figure 5.1: Projected measurements for a Kalman filter track fit.

particle. The two possible solutions in Eq. 5.5 are such that a negatively charged particle, $\tilde{q} = -1$, is bent downwards (in the negative $y$ direction) and a positive one is bent upwards (positive $y$ direction). If $\theta$ is the angle of the track with respect to the $z$ axis in the $yz$ plane (see Fig. 5.1), the coordinates of the center of the circle are:

$$y_c = y + \tilde{q} R \cos\theta, \tag{5.7}$$

$$z_c = z - \tilde{q} R \sin\theta. \tag{5.8}$$

The equation of the circle is not linear so, to keep the matrix notation of Eq. 5.2, we perform a Taylor expansion of Eq. 5.5 around $z = 0$ to linearise the problem:

$$y = \sum_{n=0}^{\infty} \beta_n \, z^n \quad , \tag{5.9}$$

$$\beta_n = \frac{1}{n!} \frac{d^n}{dz^n} \left( y_c - \tilde{q} \sqrt{R^2 - (z - z_c)^2} \right)_{z=0} \quad . \tag{5.10}$$

In principle, this expansion implies that the matrices $\mathbf{H}_k$ and $\mathbf{x}_k$ are of infinite dimension: $\mathbf{H}_k = \{1, z, z^2, z^3, ...\}$ and $\mathbf{x}_k = \{\beta_0, \beta_1, \beta_2, ...\}$. However, only three of the $\beta_n$ parameters of the expansion are independent because $y$ only depends on $y_c$, $z_c$ and $R$. The state vector $\mathbf{x}_k$ as defined in Eq. 5.1 needs to contain only the independent parameters, thus:

$$y = \begin{bmatrix} 1 \\ z \\ z^2 \end{bmatrix} . \begin{bmatrix} \beta_0 & \beta_1 & \beta_2 \end{bmatrix} + \sum_{n=3}^{\infty} \beta_n(\beta_0, \beta_1, \beta_2) \; z^n \tag{5.11}$$

The number of terms in the expansion to correctly describe the particle trajectories inside NOMAD-STAR is given by the extrapolation errors associated to each term. Fig. 5.2 shows the extrapolation errors incurred by neglecting $\Delta_j \equiv \sum_{n=j}^{\infty} \beta_n \, l_{max}^n$ in the Taylor expansion, as a function of $p_\perp$ and for track angles 10° and 60°, assuming $B = 0.4$ T and that the separation between two consecutive planes is $l_{max} = 3.6$ cm. One can see that the cubic term is still needed to ensure that the tracking accuracy remains below the intrinsic resolution of the silicon ladders (5 $\mu$m) [1] for some tracks with high angles and low momentum. NOMAD-STAR is not sensitive to further terms in the expansion.

The parameters of the cubic equation: $y = a + bz + cz^2 + dz^3$ and a possible quartic term $ez^4$ are as follows:

$$a \equiv \beta_0 = y_c - \tilde{q}\sqrt{R^2 - z_c^2}, \tag{5.12}$$

$$b \equiv \beta_1 = \frac{-\tilde{q} z_c}{\sqrt{R^2 - z_c^2}}, \tag{5.13}$$

$$c \equiv \beta_2 = \frac{\tilde{q} R^2}{2(R^2 - z_c^2)^{3/2}}, \tag{5.14}$$

$$d \equiv \beta_3 = \frac{-\tilde{q} R^2 z_c}{2(R^2 - z_c^2)^{5/2}} = \frac{2bc^2}{1 + b^2}, \tag{5.15}$$

$$e \equiv \beta_4 = \frac{\tilde{q} R^2 (R^2 + 4z_c^2)}{8(R^2 - z_c^2)^{7/2}}, \tag{5.16}$$

with $d$ and $e$ dependent on $b$ and $c$. It is also worth noting that, as the Taylor expansion was calculated for the limit $z \to 0$, it is necessary to change the coordinate system so that the most upstream plane of the measurement defines $z = 0$. Now the circle parameters can be writen in terms of a, b and c:

$$R = \tilde{q} \frac{(1 + b^2)^{3/2}}{2c} \tag{5.17}$$

$$y_c = a + \frac{(1 + b^2)}{2c} \tag{5.18}$$

$$z_c = -\frac{b(1 + b^2)}{2c} \tag{5.19}$$

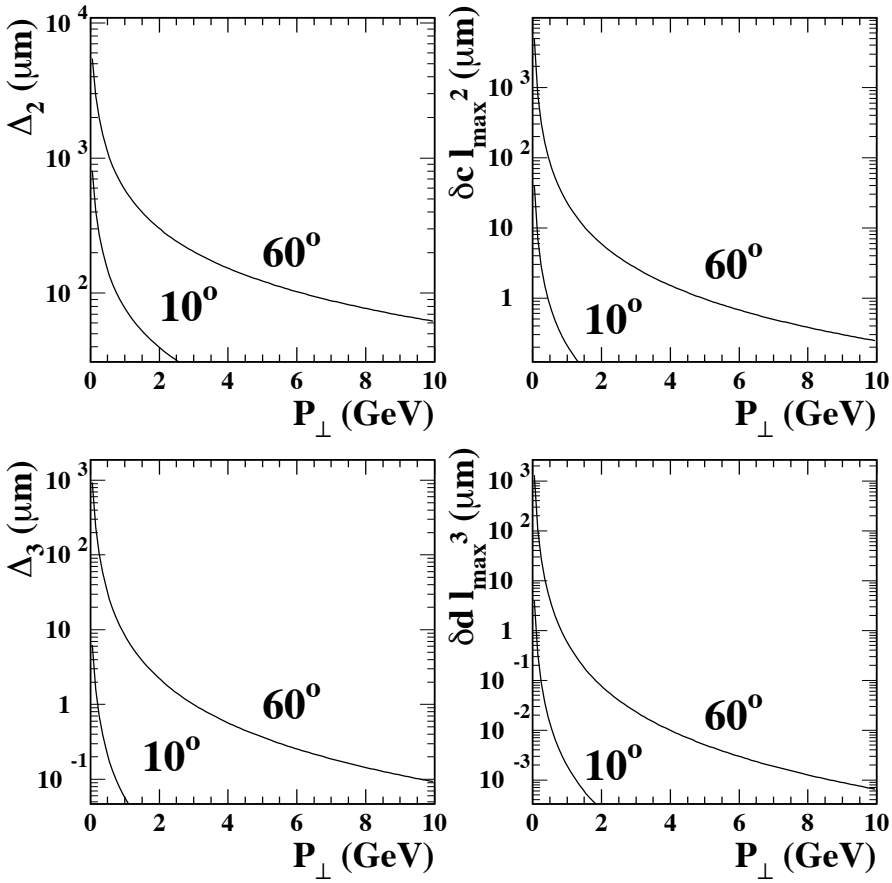


Figure 5.2: Extrapolation errors incurred by neglecting the terms $\Delta_2$ and $\Delta_3$ (where $\Delta_j \equiv \sum_{n=j}^{\infty} \beta_n \; l_{max}^n$) in the Taylor expansion, assuming the separation between consecutive planes is 3.6 cm, as a function of the momentum $p_\perp$ for track angles of $10^o$ and $60^o$. Also shown are the uncertainties due to multiple scattering of the quadratic and cubic terms of the expansion: $\delta c \; l_{max}^2$ and $\delta d \; l_{max}^3$.

### 5.4.2 Kalman Track Filter Algorithm

We now have a simplified scenario where the state vector only has three parameters so we vary the standard implementation of the Kalman Filter to accommodate this circumstance. The measurements $\mathbf{m}_k$ are the measured $y_k$ positions at a given plane at position $z_k$ (see Fig. 5.1).

The measurement equation (Eq. 5.2) has to be modified to include the fixed parameter which is not explicitly included in the state vector:

$$\mathbf{m}_k = \mathbf{H}_k \mathbf{x}_k + dz_k^3 + \epsilon_k. \tag{5.20}$$

This allows the track to be defined by a cubic polynomial, while the fit only alters the first three parameters.

The covariance matrix of the measurement:

$$cov\{\epsilon_k\} = \mathbf{V}_k = \mathbf{G}_k^{-1}, \tag{5.21}$$

is a $1 \times 1$ matrix and is equal to the square of the $y$ resolution of the silicon detectors $\sigma_y^2$.

The evolution of the state vector is given by Eq. 5.1. In the absence of energy loss or any other systematic perturbation to the system, this particular choice of state vector should not vary from one plane to another. In that case we have $\mathbf{F}_k = \mathbf{I}$, the identity matrix. However in the case of NOMAD-STAR energy loss can be visible for some low momentum particles. The inclusion of energy loss in the Kalman Filter is studied in section 5.4.2.

The process noise, defined in Eq. 5.1, is included through the covariance matrix of the extrapolation, defined as:

$$cov\{\omega_k\} = \mathbf{Q}_k. \tag{5.22}$$

This matrix has two contributions, one related with multiple scattering and the other with energy loss:

$$\mathbf{Q}_k = \mathbf{Q}_k^{ms} + \mathbf{Q}_k^{el} \tag{5.23}$$

which are studied in the following two subsections.

#### Multiple Coulomb scattering

Multiple scattering was added to the Kalman filter for a parabolic track model in Ref. [27]. In this section we will generalize this for a cubic model with a more accurate multiple scattering algorithm.

The multiple scattering theory of Molière [28], reformulated by Bethe [29], can be parametrised by a Gaussian approximation [30], where the width of the distribution is given by:

$$\theta_{ms}^2 = \frac{\chi_c^2}{1+F^2}\left[\frac{1+v}{v}\ln(1+v) - 1\right] \quad , \tag{5.24}$$

with:

$$v = \frac{0.5\Omega}{1-F}, \tag{5.25}$$

and where:

$$\Omega = b_c\, q^2 \frac{s}{\beta^2} \tag{5.26}$$

is the mean number of scatters, $s$ is the path length of the particle and $F = 0.98$ is the fraction of tracks considered in the Gaussian distribution. The critical scattering angle [31] is:

$$\chi_c = \chi_{cc}\, q \frac{\sqrt{s}}{p_\perp \beta}, \tag{5.27}$$

with $\chi_{cc} \approx (0.39612 \times 10^{-3})^2 Z'_s \frac{\rho}{W}$, $q$ and $\beta$ the charge and speed of the incident particle, $\rho$ and $W$ the density and molecular weight of the material, and:

$$b_c \approx 6702.33 \rho Z'_s e^{(Z'_x - Z'_E)/Z'_s}. \tag{5.28}$$

For a mixture or compound, the following variables are defined:

$$Z'_s = \sum_{i=1}^{N} \frac{p_i}{A_i} Z_i(Z_i+1), \tag{5.29}$$

$$Z'_E = \sum_{i=1}^{N} \frac{p_i}{A_i} Z_i(Z_i+1)\ln(Z_i^{-2/3}), \tag{5.30}$$

$$Z'_x = \sum_{i=1}^{N} \frac{p_i}{A_i} Z_i(Z_i+1)\ln\left[1 + 3.34\left(\frac{qZ_i}{137\beta}\right)^2\right], \tag{5.31}$$

where $Z_i$ and $A_i$ are the atomic number and atomic weight of each element in the mixture, $p_i$ is the proportion by weight of that element and $N$ the total number of elements. This approximation reproduces the Molière theory with an accuracy of 2%.

For an incident particle of $q = \pm 1$, and for the case of boron carbide, the term $\frac{1+v}{v} \approx 1$ and then Eq. 5.24 becomes:

$$\theta_{ms}^2 = ks\left[\ln(1+Bs) - 1\right], \tag{5.32}$$

with $k = 5.8335 \times 10^{-7}/(p_\perp^2\beta^2)$ and $B = \frac{402685}{\beta^2}e^{-4.944\times10^{-3}/\beta^2}$ (if $s$ is in cm and $p_\perp$ is in GeV/c).

We can assume that, locally, the particle trajectory is a straight line. In that case

$$\delta(\theta_{ms}^2) = k\delta s\left[\ln(1+Bs) - \frac{1}{1+Bs}\right] = kL(z)G(z)\delta z, \tag{5.33}$$

where:

$$L(z) = 1/cos\theta = \sqrt{1+[y'(z)]^2}\ , \tag{5.34}$$

$$s(z) = \int_{z_i}^{z} L(z')dz'\ , \tag{5.35}$$

$$G(z) = \ln(1+Bs(z)) - \frac{1}{1+Bs(z)}. \tag{5.36}$$

The integral of $s(z)$ can be calculated analytically:

$$s(z) = R\left[arcsin\left(\tilde{q}\frac{z-z_c}{R}\right) - arcsin\left(\tilde{q}\frac{z_i-z_c}{R}\right)\right] \tag{5.37}$$

and using Eq. 5.17 and 5.19

$$s(z) = R\left[arcsin\left(\frac{2cz+b(1+b^2)}{(1+b^2)^{3/2}}\right) - arcsin\left(\frac{2cz_i+b(1+b^2)}{(1+b^2)^{3/2}}\right)\right] \tag{5.38}$$

Explicitly, the fitting parameters $\beta_n$ of the track model depend on the multiple scattering angle. The multiple scattering contribution to the covariance matrix of the prediction, $Q_k^{ms}$, is a $3\times3$ matrix with terms:

$$(\mathbf{Q}_k^{ms})_{ij} = cov_\theta\{\beta_i,\beta_j\} = \int \frac{\delta\beta_i}{\delta\theta}\frac{\delta\beta_j}{\delta\theta}\delta(\theta^2) = k\int_{z_i}^{z_f}\frac{\delta\beta_i}{\delta\theta}\frac{\delta\beta_j}{\delta\theta}L(z)G(z)\delta z \tag{5.39}$$

where the integration is needed for non-straight particles and $z_i$, $z_f$ are the limits of each of the $B_4C$ planes. To calculate the terms of this matrix we use the relation:

$$\delta\beta_n = -(n+1)\,\beta_{n+1}\delta z_c \quad , n > 0. \tag{5.40}$$

which is a consequence of Eq 5.10. We also use the continuity of $y(z)$:

$$0 = \delta y = \delta a + \sum_{n=1}^{\infty} \delta\beta_n \, z^n \quad = \delta a - \delta z_c \sum_{n=1}^{\infty} (n+1)\beta_{n+1} \, z^n \quad = \delta a - (y' - b)\delta z_c \tag{5.41}$$

and the relation between the multiple scattering angle and $y'(z) = \tan\theta$:

$$(1 + y'^2)\delta\theta = \delta y' = -y''\delta z_c \tag{5.42}$$

This last equation implies:

$$\delta z_c = \frac{-(1 + y'^2)}{y''} \, \delta\theta = \frac{-L(z)^2}{y''} \, \delta\theta \tag{5.43}$$

Using equations 5.40, 5.41 and 5.43 it is straight-forward to obtain the desired quantities:

$$\frac{\delta a}{\delta\theta} = -(y' - b)\frac{L(z)^2}{y''} \quad , \tag{5.44}$$

$$\frac{\delta\beta_n}{\delta\theta} = (n+1)\beta_{n+1}\frac{L(z)^2}{y''} \quad , n > 0 \tag{5.45}$$

Defining the following integrals:

$$I_1 = \int_{z_i}^{z_f} \frac{(y'(z) - b)^2 L(z)^5}{[y''(z)]^2} G(z) dz \quad , \tag{5.46}$$

$$I_2 = \int_{z_i}^{z_f} \frac{(y'(z) - b) L(z)^5}{[y''(z)]^2} G(z) dz \quad , \tag{5.47}$$

$$I_3 = \int_{z_i}^{z_f} \frac{L(z)^5}{[y''(z)]^2} G(z) dz \quad , \tag{5.48}$$

the covariance matrix can now be written:

$$\mathbf{Q}_k^{ms} = \begin{bmatrix} kI_1 & -2ckI_2 & -3dkI_2 \\ -2ckI_2 & 4c^2kI_3 & 6cdkI_3 \\ -3dkI_2 & 6cdkI_3 & 9d^2kI_3 \end{bmatrix} \quad . \tag{5.49}$$

In the case of the cubic equation: $y'(z) = b + 2cz + 3dz^2$ and $y''(z) = 2c + 6dz$. These integrals are performed numerically for each $B_4C$ plane traversed. The error terms $\delta c = \sqrt{9d^2kI_3}$ and $\delta d = \sqrt{16e^2kI_3}$ are shown in Fig. 5.2. $\delta d$ is found to be negligible for the case of NOMAD-STAR.

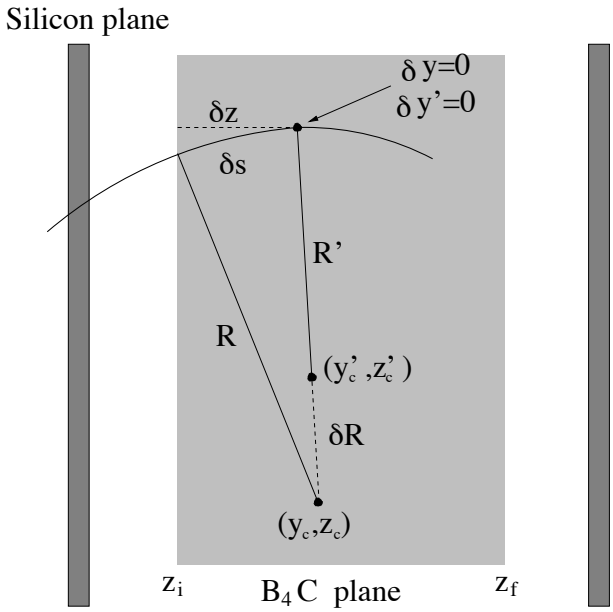


Figure 5.3: Variation of the circle parameters induced by energy loss.

### Energy loss

The trajectory of particles in dense media is affected by energy loss. For moderately relativistic particles other than electrons, the mean rate of energy loss is given by the well known Bethe-Bloch formula [32].

As is shown in Eq. 5.3, the radius of the circle is proportional to $p_\perp$. As the particle loses energy, the radius of the circle does not remain constant and the trajectory is like a spiral. To simplify the Kalman filter formalism we can assume that, locally, the trajectory of the particle is still a circle (Fig.5.3). We assume that energy loss changes the parameters of the circle in a continuous way from one point to the next (in certain cases, delta rays may break this continuity). This assumption implies the continuity of $y(z)$ and $y'(z)$. The infinitesimal variation in the circle parameters can be written in terms of $\delta R$, $\delta y_c$ and $\delta z_c$, but only one of these variations is independent because of the two constraints $\delta y(z) = 0$ and $\delta y'(z) = 0$. Starting from equation 5.5, it is easy to obtain:

$$\delta y_c = -(y - y_c)\frac{\delta R}{R}, \tag{5.50}$$

$$\delta z_c = -(z - z_c)\frac{\delta R}{R}, \tag{5.51}$$

which can also be intuitively extracted from figure 5.3. The variation in the expansion coefficients is:

$$\delta\beta_n = \frac{\partial\beta_n}{\partial R}\delta R + \frac{\partial\beta_n}{\partial y_c}\delta y_c + \frac{\partial\beta_n}{\partial z_c}\delta z_c \quad . \tag{5.52}$$

Introducing the derivatives of equations 5.12, 5.13 and 5.14 into 5.52, and using also 5.50 and 5.51, we obtain:

$$\delta a = -\frac{\delta R}{R}\sum_{n=2}^{\infty}\beta_n z^n \simeq -cz^2\frac{\delta R}{R}, \tag{5.53}$$

$$\delta b = 2cz\frac{\delta R}{R}, \tag{5.54}$$

$$\delta c = (-c + 3dz)\frac{\delta R}{R} \simeq -c\frac{\delta R}{R}. \tag{5.55}$$

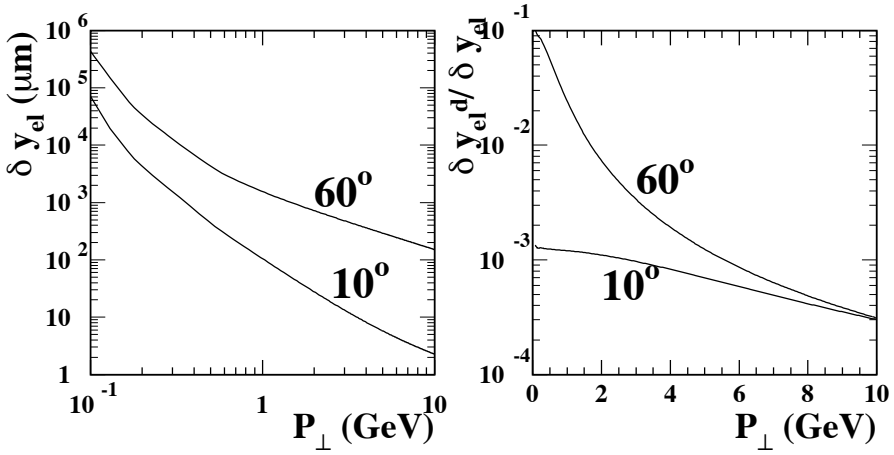


Figure 5.4: a) Extrapolation error incurred by neglecting the energy loss effect through a single $B_4C$ layer and a distance of $3.6cm$ between measurement points (only the dominant terms up to $c$ included) as a function of the momentum for different angles. b) Ratio between the $d$-term and the dominant terms up to $c$ of the extrapolation error due to energy loss.

These two approximations are needed if we want to keep the formalism of Eq. 5.1. Figure 5.4 b) shows the ratio between the terms containing $d$ and the dominant terms up to the one containing $c$ of equations 5.53, 5.54 and 5.55. In general, this ratio is very small, thereby justifying the previous approximations. Now we have to find out how the radius of the circle is affected by energy loss:

$$\frac{dR}{R} = \frac{dp_\perp}{p_\perp} = \frac{dE}{E} = \frac{\beta}{p}\frac{dE}{ds}ds. \tag{5.56}$$

At a given z, the momentum of the particle can be calculated by integrating the Bethe-Bloch formula for energy loss along the length of $B_4C$:

$$p(z) = \int \beta \frac{dE}{ds}ds = \int_{z_i}^{z_f} \beta \frac{dE}{ds}\frac{L(z)}{\cos\gamma}dz, \tag{5.57}$$

where $\gamma$ is the angle between $\mathbf{p}$ and $\mathbf{p}_\perp$ and $\beta = \frac{v}{c} = \frac{p}{E}$. This integral can be performed numerically, but if one assumes that the energy loss can be approximated by a power law:

$$\frac{dE}{ds} = \alpha_1 p^{\alpha_2} \quad , \tag{5.58}$$

then the integral can be performed analytically (assuming $\beta$ constant):

$$p(z) = \left[p_i^{1-\alpha_2} + \beta(1-\alpha_2)\alpha_1\, s(z)\right]^{1/(1-\alpha_2)}. \tag{5.59}$$

Using equations 5.56, 5.58:

$$\frac{dR}{R} = \frac{\beta\alpha_1}{p_i^{1-\alpha_2}\, cos\gamma}\ \frac{1}{1+\frac{\beta(1-\alpha_2)\alpha_1\, s(z)}{p_i^{1-\alpha_2}}}L(z)dz, \tag{5.60}$$

We now combine Eqs. 5.53, 5.54, 5.55 and 5.60, and integrate over the thickness of the $B_4C$ plates, to obtain the $\mathbf{F_k}$ matrix of Eq. 5.1:

$$\mathbf{F}_k = \begin{bmatrix} 1 & 0 & -k_{el}\int_{z_i}^{z_f} z^2F(z)L(z)dz \\ 0 & 1 & 2k_{el}\int_{z_i}^{z_f} zF(z)L(z)dz \\ 0 & 0 & 1-k_{el}\int_{z_i}^{z_f} F(z)L(z)dz \end{bmatrix}. \tag{5.61}$$

where the parameter $k_{el}$ is:

$$k_{el} = \frac{\beta\alpha_1}{p_i^{1-\alpha_2}\, cos\gamma} \tag{5.62}$$

and F(z) is defined as:

| **Momentum range** (GeV/c) | $\alpha_1$ | $\alpha_2$ |
|---|---|---|
| $p_\perp < 0.17$ | $5.729 \times 10^{-4}$ | -1.321 |
| $0.17 < p_\perp < 0.51$ | $3.715 \times 10^{-3}$ | -0.2636 |
| $p_\perp > 0.51$ | $4.615 \times 10^{-3}$ | 0.06141 |

Table 5.1: Parameters for power law parametrizations (Eq. 5.58) of the Bethe-Bloch energy loss formula for $B_4C$. With these parameters, the energy loss is in units of GeVcm$^{-1}$.

$$F(z) = \frac{1}{1 + \frac{\beta(1-\alpha_2)\alpha_1 \, s(z)}{p_i^{1-\alpha_2}}} \quad . \tag{5.63}$$

Notice that at first order, the variation of the state vector between two silicon planes induced by energy loss depends only on the quadratic parameter $c$ as can be seen from equations 5.53, 5.54 and 5.55.

We have parametrized the Bethe-Bloch formula for $B_4C$ (with $dE/ds$ in units of GeVcm$^{-1}$) using Eq. 5.58, with the parameters given in table 5.1 for relevant momentum ranges. This approximation is accurate to better than 10% below 1 GeV/c, and is better than 0.5% between 1 GeV/c and 10 GeV/c. Figure 5.5 shows the parameterised Bethe-Bloch formula and the ratio between this approximation and the Bethe-Bloch formula. Figure 5.4 a) shows the extrapolation error incurred if we do not take into account energy loss in the Kalman filter matrix (Eq. 5.61).

Eq. 5.58 gives the mean rate of energy loss, but in fact fluctuations in energy loss follow a Landau distribution, which is approximately Gaussian for thick media. These random fluctuations contribute to the process noise and are included in the Kalman filter mechanism through the covariance matrix $\mathbf{Q}_k^{el}$ defined in Eq. 5.23. In NOMAD-STAR, the energy loss effect is relatively small, so it has been assumed that the error induced by this effect is even smaller and can therefore be neglected when we add it in quadrature (see eq. 5.23) to the multiple scattering error. This may not be a valid assumption and further work is in progress to extend the covariance matrix to reflect the gaussian approximation to the Landau distribution.

Dramatic energy loss, such as that at the tail of the Landau distribution and delta rays may break the continuity of $y'(z)$ and thus invalidate the assumptions made in this derivation.

Having determined the track model and process noise, the Kalman track filter can now be broken down into its three constituent phases: prediction, filter and smoother (see for example Ref. [16]).

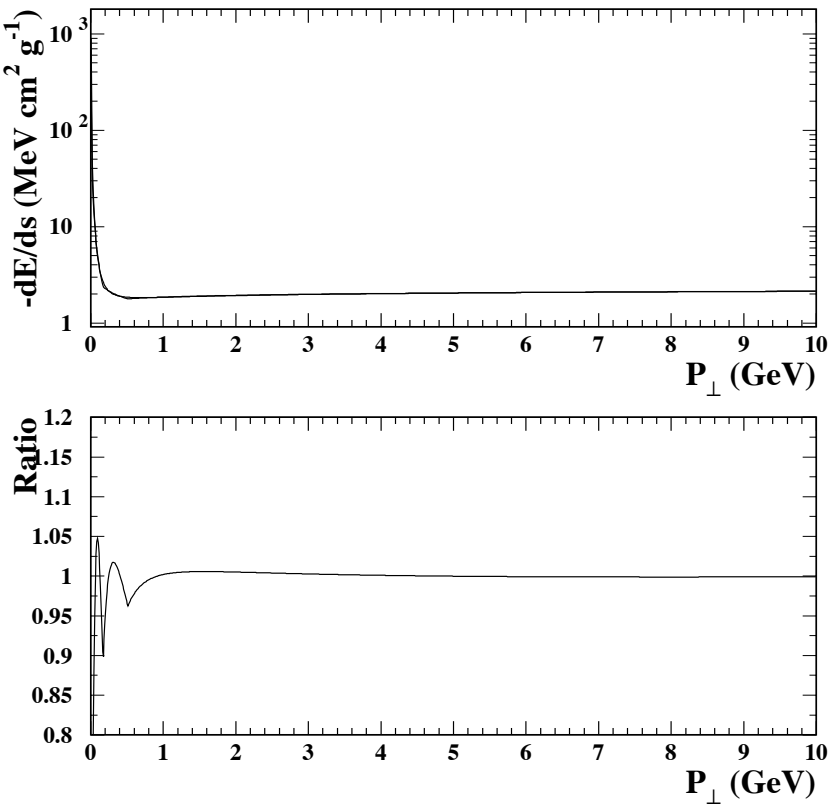


Figure 5.5: Parameterisation of the Bethe-Bloch equation and the ratio between this parameterisation and the original formula.

### Prediction

A prediction of the state vector $\mathbf{x}_k^P$ made at measurement plane $k$ is based on the state vector information at plane $k-1$.

The NOMAD drift chambers provide tracking and momentum information for each of the reconstructed tracks. The initial conditions for the state vector are given by the first silicon hit position, which defines $a$, and the parameters $b$, $c$ and $d$ (Eqs. 5.13-5.15) as given by the drift chambers.

Given the covariance matrix of the state vector as:

$$\mathbf{C}_k = cov\{\mathbf{x}_k^P - \mathbf{x}_k\}, \tag{5.64}$$

the extrapolation of the covariance matrix (the prediction for this covariance matrix given the knowledge of this matrix from previous steps) is:

$$\mathbf{C}_k^P = \mathbf{F}_k \mathbf{C}_{k-1} \mathbf{F}_k^T + \mathbf{Q}_k. \tag{5.65}$$

Again, the initial conditions for the covariance matrix are given by the resolution of the first silicon hit and the errors in the parameters as determined by the drift chamber fit.

The residuals of the prediction from the measurement at plane $k$ is:

$$\mathbf{r}_k^P = \mathbf{m}_k - \mathbf{H}_k \mathbf{x}_k^P - dz_k^3. \tag{5.66}$$

The covariance of this residual is then:

$$\mathbf{R}_k^P = \mathbf{V}_k + \mathbf{H}_k \mathbf{C}_k^P \mathbf{H}_k^T + z_k^6 \sigma_{dd}^2, \tag{5.67}$$

where $\sigma_{dd}^2$ is the square of the error in the parameter $d$ due to the uncertainty in the measured track momentum.

### Filter

The filtering process now incorporates information from the measurement at plane $k$ into the state vector $\mathbf{x}_k$:

$$\mathbf{x}_k = \mathbf{x}_k^P + \mathbf{K}_k \mathbf{r}_k^P, \tag{5.68}$$

where $\mathbf{K}_k$ is known as the Kalman gain matrix that updates the relationship between the state vector and the measurements by including the new information:

$$\mathbf{K}_k = \mathbf{C}_k^P \mathbf{H}_k^T \mathbf{G}_k. \tag{5.69}$$

The updated covariance matrix is then:

$$\mathbf{C}_k = (\mathbf{I} - \mathbf{K}_k\mathbf{H}_k)\mathbf{C}_k^P, \tag{5.70}$$

with the filtered residuals:

$$\mathbf{r}_k = \mathbf{m}_k - \mathbf{H}_k\mathbf{x}_k^P - dz_k^3, \tag{5.71}$$

and the covariance matrix of the filtered residuals:

$$\mathbf{R}_k = (\mathbf{I} - \mathbf{H}_k\mathbf{K}_k)\mathbf{V}_k + z_k^6\sigma_{dd}^2. \tag{5.72}$$

The $\chi^2$ of measurement $k$ at this stage of the filtering process is:

$$\chi_k^2 = \mathbf{r}_k^T\mathbf{R}_k^{-1}\mathbf{r}_k. \tag{5.73}$$

**Smoother**

Once every measurement has been filtered, the smoother is then used to propagate all the information added during the filtering process to a given measurement plane. The superscript $S$ is used to denote the value after the smoothing operation. The smoothed state vector is:

$$\mathbf{x}_k^S = \mathbf{x}_k + \mathbf{A}_k(\mathbf{x}_{k+1}^S - \mathbf{x}_{k+1}^P), \tag{5.74}$$

with:

$$\mathbf{A}_k = \mathbf{C}_k\mathbf{F}_{k+1}^T(\mathbf{C}_{k+1}^P)^{-1} = \mathbf{C}_k(\mathbf{C}_{k+1}^P)^{-1}, \tag{5.75}$$

and the smoothed covariance matrix, residuals and covariance of the residuals being:

$$\mathbf{C}_k^S = \mathbf{C}_k + \mathbf{A}_k(\mathbf{C}_{k+1}^S - \mathbf{C}_{k+1}^P)\mathbf{A}_k^T \quad , \tag{5.76}$$

$$\mathbf{r}_k^S = \mathbf{m}_k - \mathbf{H}_k\mathbf{x}_k^S - dz_k^3 \quad , \tag{5.77}$$

$$\mathbf{R}_k^S = \mathbf{V}_k - \mathbf{H}_k\mathbf{C}_k^S\mathbf{H}_k^T + z_k^6\sigma_{dd}^2 \quad . \tag{5.78}$$

Figure 5.6 shows the residuals for all hits in all tracks with data represented by points with error bars overlayed on $\nu_\mu$ charged current Monte Carlo. The RMS of this distribution is $8.6\mu m$.

The $\chi^2$ also has to be modified for the smoothed values:

$$\chi^{2^S}_k = (\mathbf{r}_k^S)^T(\mathbf{R}_k^S)^{-1}\mathbf{r}_k^S. \tag{5.79}$$

Figure 5.7 shows the smoothed $\chi^2$ and $\chi^2$ probability for data and Monte Carlo for all hits in all tracks.

The three step process of prediction, filtering and smoothing is iterated for all the measurement planes up to and including the information from the

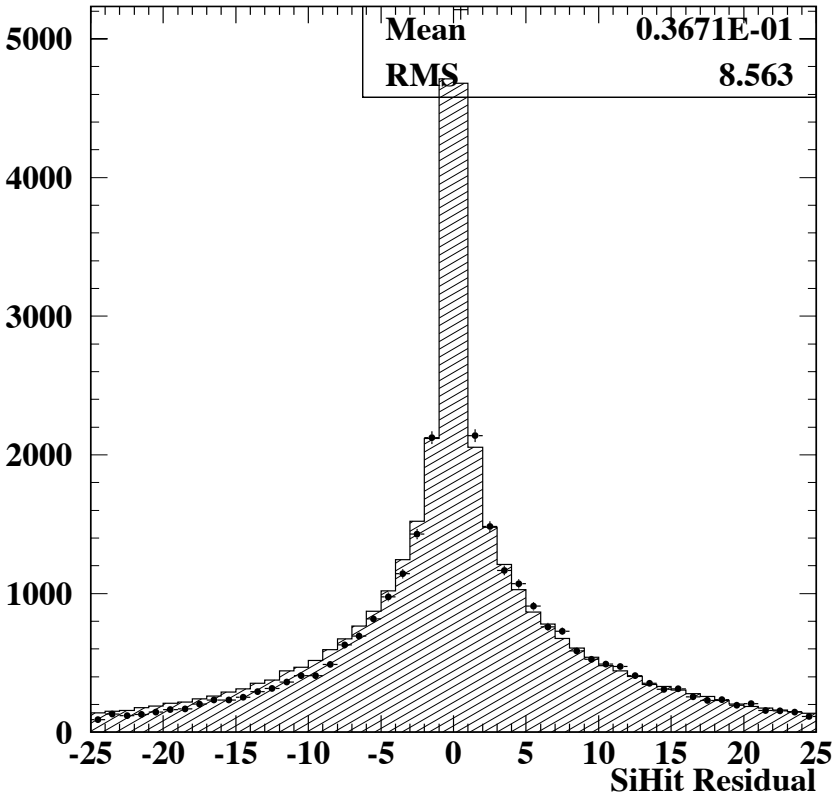


Figure 5.6: Distribution of residuals for all hits ($\mu m$)

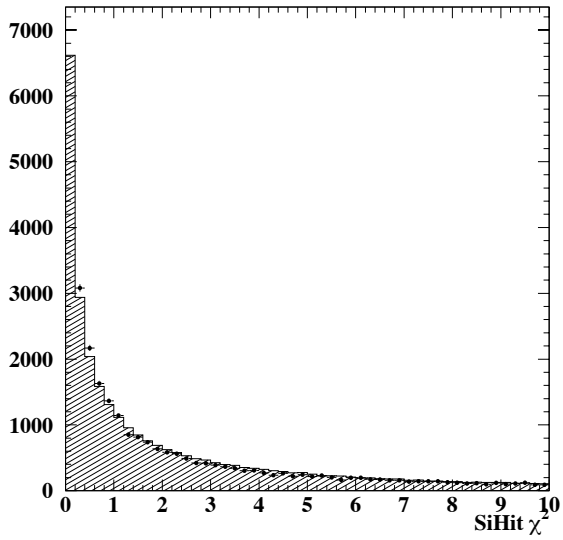


(a) $\chi^2$

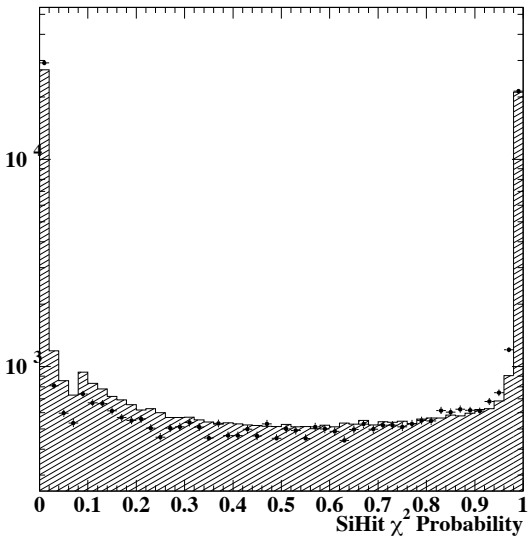


(b) $\chi^2$ probability

Figure 5.7: Distributions of the smoothed SiHit $\chi^2$ and $\chi^2$ probability in the SiTrack

most upstream plane. The whole procedure then gives the track parameters at the plane closest to the interaction point.

The total $\chi^2$ for the track is determined from the sum of the $\chi^2$ contributions of each hit in the track fit.

The total $\chi^2$ and $\chi^2$ probability for data and Monte Carlo are shown in Figures 5.8-5.10 for all tracks, those tracks fitted into the primary vertex and those tracks not in any vertex.

Even though the distributions are in reasonable agreement with each other, the small discrepancies at low $\chi^2$ are probably due to the larger number of low multiplicity events as well as the lower hit finding efficiency in the data.

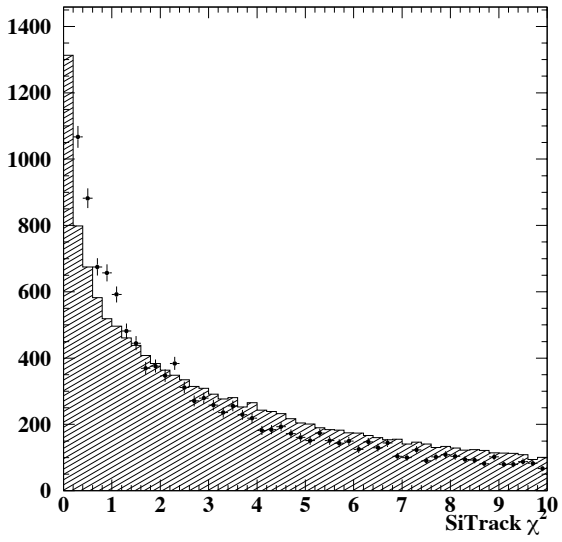


(a) $\chi^2$

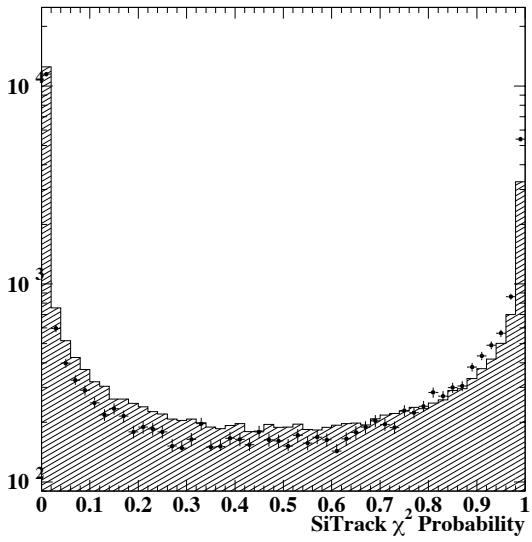


(b) $\chi^2$ probability

Figure 5.8: Distributions of SiTrack total $\chi^2$ and $\chi^2$ probability for all SiTracks

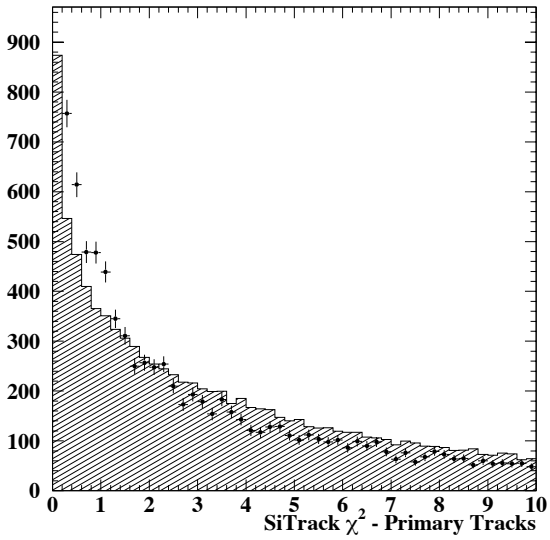


(a) $\chi^2$

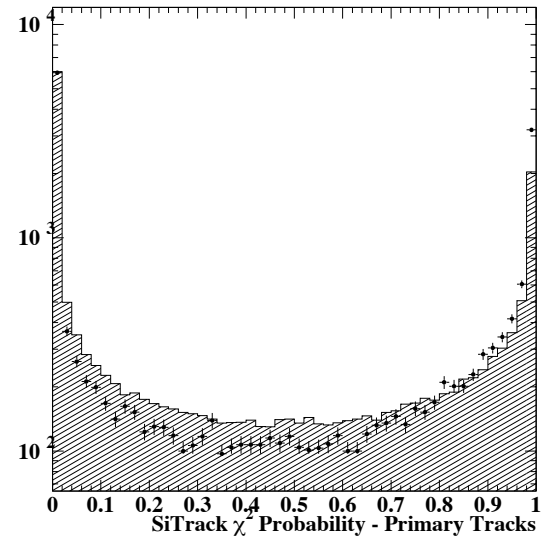


(b) $\chi^2$ probability

Figure 5.9: Distributions of SiTrack total $\chi^2$ and $\chi^2$ probability for SiTracks in the Primary Vertex

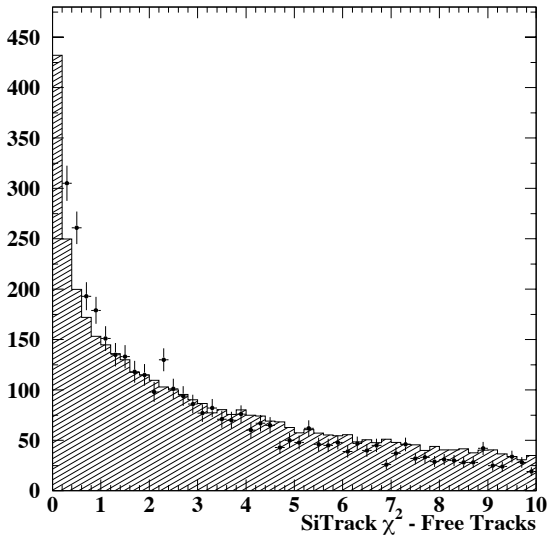


(a) $\chi^2$

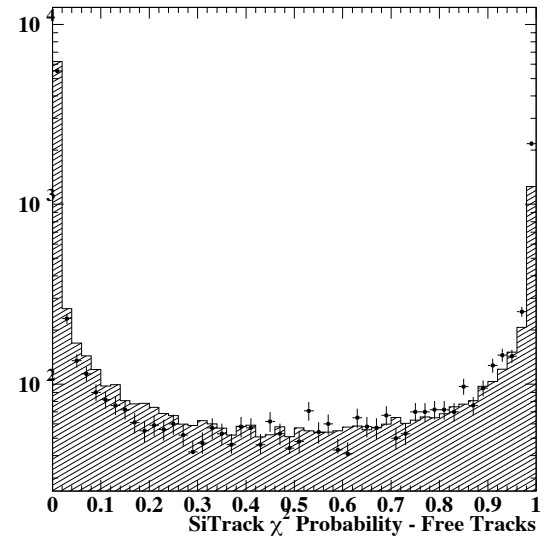


(b) $\chi^2$ probability

Figure 5.10: Distributions of SiTrack total $\chi^2$ and $\chi^2$ probability for free SiTracks

# Chapter 6

# Vertex Reconstruction

## 6.1 Introduction

Once tracks have been reconstructed in the detector, it is possible to use the fitted track parameters to determine the most likely position of the neutrino interaction and that of any subsequent decays.

## 6.2 Pattern Recognition

The limitations of the 2 dimensional information recorded by STAR become evident during the vertex building and fitting stage. As each track is only recorded as the projection of the true track onto the y-z plane, it is not sufficient to look at crossing points of tracks to determine an estimate of the location of the neutrino interaction (primary vertex).

The main analyses required of STAR are a measurement of the Impact Parameter resolution of the detector, the search for the decay of strange mesons and the search for the decay of charmed mesons. As these three analyses all involve the study of $\nu_\mu$ charged current interactions, the pattern recognition uses this information.

The procedure starts by looking for a muon candidate STAR track (SiTrack). This track is chosen as the most "muon-like" in the event. If there exists a muon of the correct sign as identified by the muon chambers, then it will, of course, be chosen. If there is no such track, then the track of type Unknown (which means not an electron, muon or pion) with the correct sign and highest momentum is chosen.

This muon candidate is then tested against all other SiTracks in the event to find the crossing point in the y-z plane. If the crossing point is within the boundaries of STAR, then all other SiTracks are extrapolated to this position

and the amount by which this extrapolation misses the crossing point is compared with a cut of $100\mu m$. The combination of muon and another track that allows the largest number of tracks to pass this cut is taken as the basis for building the primary vertex.

These tracks are fitted into a primary vertex using the Kalman filter described below, and the remaining tracks are tested against the new position returned by the fit. Any more tracks which are now consistent with the new vertex position are added and the vertex is refitted.

## 6.3 Kalman Vertex Filter

The vertex fit is an iterative procedure and is similar to the track fit, except that the measurements now consist of the track parameters determined in the track fit, $\mathbf{P}_k = \{a, b, c, d\}$, and the state vector becomes the position of the vertex $\mathbf{x} = \{y, z\}$ (see Fig 6.1). Each track is weighted according to the inverse of the covariance matrix of the measurements:

$$\mathbf{G}_k = (cov(\mathbf{P}_k))^{-1}. \tag{6.1}$$

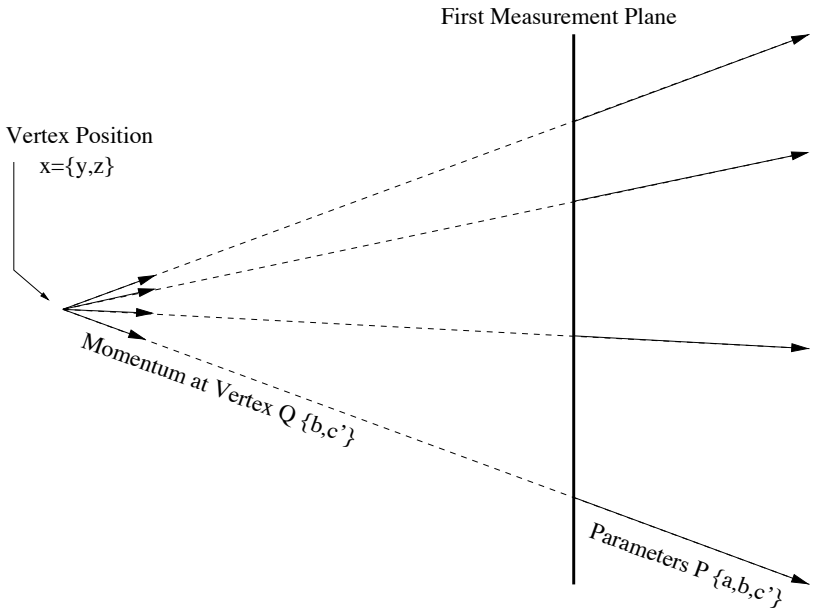


Figure 6.1: Schematic of the Kalman vertex fit.

The tracks with lower momentum will have lower weights, due to the effects of multiple scattering, and so will have a smaller effect on the vertex position. These low momentum tracks have the largest values of the parameters $c$ and $d$ and so in order to save computing time without any significant penalty in vertex accuracy, a new set of track parameters is used: $\mathbf{P}_k = \{a, b, c'\}$, where the parameters $a$ and $b$ are the same as before, but the new parameter $c' = c + d \cdot z$, with $z$ the coordinate of the vertex after the last filter (or the initial estimate, if this is the first iteration). This produces a local approximation to the cubic track model which is accurate as long as the vertex position does not move significantly during the filtering stage.

The covariance matrix of the state vector will again be represented by $\mathbf{C}_k$. An additional vector $\mathbf{Q}_k = \{b, c'\}$ is introduced to represent the angle and magnitude of the momentum of track $k$ at the vertex. The measurement equation contains the track model:

$$\mathbf{P}_k = \mathbf{H}_k(\mathbf{x}_k, \mathbf{Q}_k) + \epsilon_k, \tag{6.2}$$

with the function $\mathbf{H}$ defined as:

$$\mathbf{H}(0) = y - bz - c'z^2 \tag{6.3}$$

$$\mathbf{H}(1) = \frac{y-a}{z} - c'z \tag{6.4}$$

$$\mathbf{H}(2) = \frac{y-a}{z^2} - \frac{b}{z} \tag{6.5}$$

In order to complete the vertex fit, it is necessary to introduce 2 additional matrices:

$$\mathbf{A}_k = \frac{\delta \mathbf{P}_k}{\delta \mathbf{x}_k} = \begin{bmatrix} 1 & -b - 2c'z \\ \frac{1}{z} & \frac{a-y}{z^2} - c' \\ \frac{1}{z^2} & \frac{2(a-y)}{z^3} + \frac{b}{z^2} \end{bmatrix}, \tag{6.6}$$

$$\mathbf{B}_k = \frac{\delta \mathbf{P}_k}{\delta \mathbf{Q}_k} = \begin{bmatrix} 0 & 0 \\ 1 & 0 \\ 0 & 1 \end{bmatrix}, \tag{6.7}$$

such that the function $\mathbf{H}_k$ is linear around the point $(\mathbf{x}_{k,0}, \mathbf{Q}_{k,0})$:

$$\mathbf{H}_k(\mathbf{x}_{k,0}, \mathbf{Q}_{k,0}) = \mathbf{c}_{k,0} + \mathbf{A}_k \mathbf{x}_{k,0} + \mathbf{B}_k \mathbf{Q}_{k,0} \quad , \tag{6.8}$$

and serves as a definition for $\mathbf{c}_{k,0}$. We can then proceed to perform the stages of the Kalman vertex filter as outlined in [16].

### Prediction

The prediction equations are approximated by the parameters at the last measurement plane:

$$\mathbf{x}_k^P = \mathbf{x}_{k-1}, \tag{6.9}$$

$$\mathbf{C}_k^P = \mathbf{C}_{k-1}. \tag{6.10}$$

### Filter

The new state vector after filtering is:

$$\mathbf{x}_k = \mathbf{C}_k[(\mathbf{C}_{k-1})^{-1}\mathbf{x}_{k-1} + \mathbf{A}_k^T\mathbf{G}_k^B(\mathbf{P}_k - \mathbf{c}_{k,0})], \tag{6.11}$$

where the following matrices are also defined:

$$\mathbf{C}_k = [(\mathbf{C}_{k-1})^{-1} + \mathbf{A}_k^T\mathbf{G}_k^B\mathbf{A}_k]^{-1}, \tag{6.12}$$

$$\mathbf{G}_k^B = \mathbf{G}_k - \mathbf{G}_k\mathbf{B}_k\mathbf{W}_k\mathbf{B}_k^T\mathbf{G}_k, \tag{6.13}$$

$$\mathbf{W}_k = [\mathbf{B}_k^T\mathbf{G}_k\mathbf{B}_k]^{-1}. \tag{6.14}$$

The $\chi^2$ of each filter step has 2 degrees of freedom:

$$\begin{aligned}\chi^2_{k,F} \;=\; & (\mathbf{P}_k - \mathbf{c}_{k,0} - \mathbf{A}_k\mathbf{x}_k - \mathbf{B}_k\mathbf{Q}_k)^T\mathbf{G}_k(\mathbf{P}_k - \mathbf{c}_{k,0} - \mathbf{A}_k\mathbf{x}_k - \mathbf{B}_k\mathbf{Q}_k) + \\ & (\mathbf{x}_k - \mathbf{x}_{k-1})^T(\mathbf{C}_{k-1})^{-1}(\mathbf{x}_k - \mathbf{x}_{k-1}),\end{aligned} \tag{6.15}$$

so the total $\chi^2$ of the fit after adding $k$ tracks is just:

$$\chi^2_k = \chi^2_{k-1} + \chi^2_{k,F}. \tag{6.16}$$

The filter is recomputed until there is no significant change in the $\chi^2$ or in the parameter estimates.

### Inverse Filter

It is also possible to remove a track from a vertex fit by applying the inverse filter. The procedure is identical to the filter except in the sign of the matrix $A_k$:

$$\mathbf{x}_k = \mathbf{C}_k[(\mathbf{C}_{k-1})^{-1}\mathbf{x}_{k-1} - \mathbf{A}_k^T\mathbf{G}_k^B(\mathbf{P}_k - \mathbf{c}_{k,0})], \tag{6.17}$$

with:

$$\mathbf{C}_k = [(\mathbf{C}_{k-1})^{-1} - \mathbf{A}_k^T \mathbf{G}_k^B \mathbf{A}_k]^{-1}. \tag{6.18}$$

### Smoother

The smoother does not make any changes to the vertex position since it is assumed that there is no process noise. Rather, it finds the parameters of each track at the final vertex position:

$$\mathbf{x}_k^S = \mathbf{x}_k, \tag{6.19}$$

$$\mathbf{C}_k^S = \mathbf{C}_k, \tag{6.20}$$

$$\mathbf{Q}_k^S = \mathbf{W}_k \mathbf{B}_k^T \mathbf{G}_k (\mathbf{P}_k - \mathbf{c}_{k,0} - \mathbf{A}_k \mathbf{x}_k). \tag{6.21}$$

### Initial Conditions

It has been found that the result of the vertex fit is very sensitive to the initial conditions that are passed to it. This is a peculiarity of a fixed target neutrino experiment, where there is no *a priori* vertex estimate, as opposed to the case of collider experiments or to other fixed target experiments where a well defined target region is defined. An initial estimate for the vertex position and the covariance matrix for this estimate need to be chosen with some care. If the initial vertex position is chosen to be at the origin (or at some other arbitrary location) and the covariance matrix correspondingly large, the fit may not converge quickly (or not at all) as the majority of events in NOMAD-STAR have low multiplicity. If the initial covariance matrix is too small then no matter where the initial position of the vertex is chosen, the filter will have a very small effect compared to the weight of the initial estimate of the track parameters. As a result, the initial estimate should have some physical basis and, in our case, it is made by finding the crossing point of at least 2 tracks while determining the accuracy of this initial estimate by studying Monte Carlo events.

An additional consideration is raised when there are three or more tracks in the vertex fit. A typical $\nu_\mu$ charged current interaction with three or more tracks will contain a $\mu^-$ with a large momentum and several other hadronic tracks of lower momenta. It would be tempting to take the $\mu^-$ and the highest momentum hadronic track to calculate the initial vertex estimate, as this combination suffers least from multiple scattering. This can cause a problem, however, as the initial vertex will lie exactly on the extrapolated

paths of the two highest momenta (and thus highest weight) tracks and the filter will fail to effectively incorporate information from the other lower momentum tracks. In practice, this effect causes the vertex position to only move up and down the path of the highest momentum track. The solution is to take at least three tracks and find the centre of the triangle defined by the 3 crossing points of these tracks. The filter will see that the vertex position does not agree perfectly with any given track and will thus be free to move the vertex to accommodate all the tracks in the fit, weighted appropriately.

## 6.4 Comparison of Data and Monte Carlo

### 6.4.1 Multiplicity and Vertex Position

For this comparison, the filtered sample of 11528 events from the 1998 data taking run are compared with the 62880 simulated $\nu_\mu$ CC events. A detailed discussion of the filter procedure and Monte Carlo is made in Section 8.2.

When comparing the mulitplicity in data and Monte Carlo, it is important to note that the $\nu_\mu$ charged current Monte Carlo only simulated deep inelastic scattering, and so there will be quasi-elastic events in the data with no corresponding sample in the Monte Carlo.

Although an analysis of the quasi-elastic rate in STAR has not been performed, it is possible to estimate the relative fraction of quasi-elastic to deep inelastic (DIS) events in the full NOMAD target.

For an isoscalar target, the DIS cross section is:

$$\frac{\sigma(DIS)}{E} = 0.67 \times 10^{-38} cm^2 GeV^{-1} \tag{6.22}$$

Quasi-elastic (QEL) interactions are practically independent of the neutrino energy and the neutrino beam simulation NEGLIB uses the cross-section:

$$\sigma(QEL) = 0.4455 \times 10^{-38} cm^2 \tag{6.23}$$

These cross sections, along with the flux estimates used in the simulations, predict a total of $1.628 \times 10^6$ DIS and $0.043 \times 10^6$ QEL interactions in the standard NOMAD fiducial volume. Although there is some evidence, based on the observed numbers of DIS events in the data, to suggest that the flux used may be overstimated by up to 20%, the prediction of the ratio of DIS to QEL interactions should be reliable. STAR is exposed to the central part of the neutrino beam and thus one would expect a slightly different ratio of

DIS to QEL events, however it would be of a similar order to that obtained for NOMAD as a whole of approximately 38:1.

There is a small difference in the distribution of the number of reconstructed tracks in the drift chambers (Fig. 6.2) and as these are the basis for the pattern recognition in STAR, it is expected that there will be a difference in the number of reconstructed STAR tracks (Fig. 6.3).

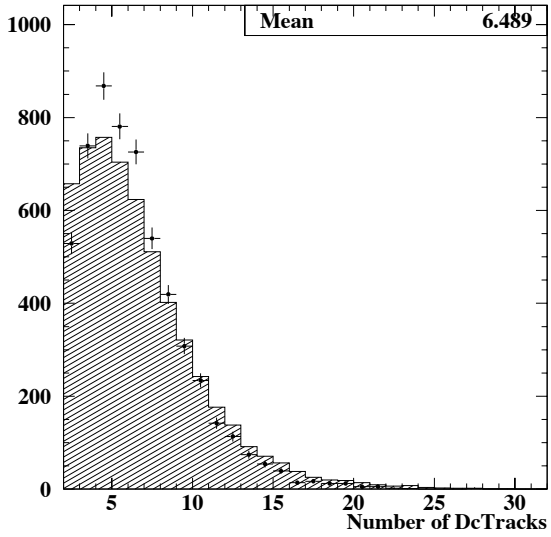


Figure 6.2: Distribution of the number of reconstructed tracks in the Drift Chambers

As the STAR detector contains no tracking information in the x direction, the position of the vertex in x is determined approximately from the extrapolation of tracks from the Drift Chambers (Fig 6.4).

The distribution of the reconstructed Z position (Fig 6.5) of the primary vertex shows the structure of the STAR detector as shown in Figure 3.5. The Monte Carlo only simulated the 4 blocks of $B_4C$ which is why there are very few reconstructed interactions in the gaps between the blocks. In the data, the silicon ladders, carbon fibre supports and aluminium covers have resulted in a small number of interactions between the passive targets.

The Kalman vertex fit produces, through the square-root of the diagonal elements of the covariance matrix, an estimate of the uncertainty in the reconstructed vertex position in the Y and Z directions (Fig. 6.6). These estimates will be used to cut on the quality of reconstructed charm candidate vertices.

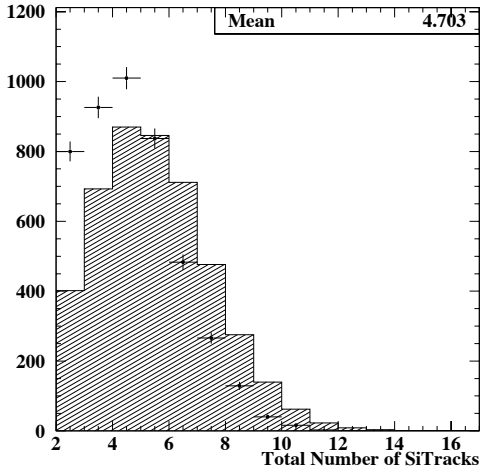


(a) Number of Reconstructed STAR Tracks

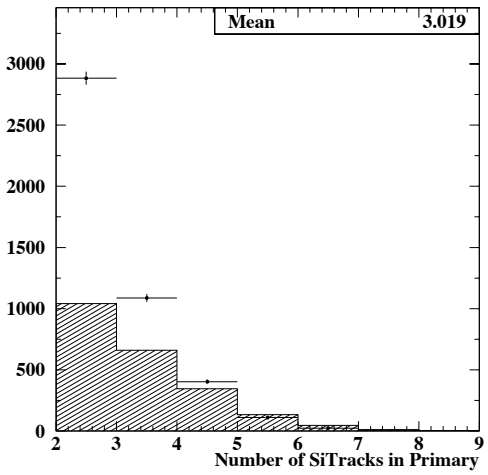


(b) Number of STAR Tracks in the Primary Vertex

Figure 6.3: Distributions of the number of STAR tracks in the event and in the primary vertex. Note the excess of events with 2 or 3 tracks in the data compared with Monte Carlo due to the absence of quasi-elastic events in the simulation

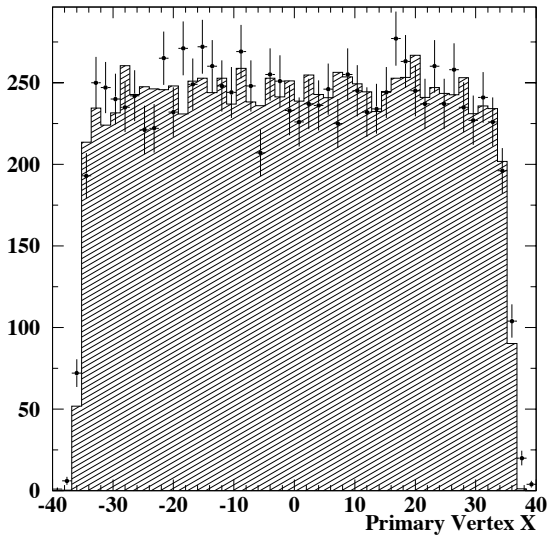


(a) X Position (cm)

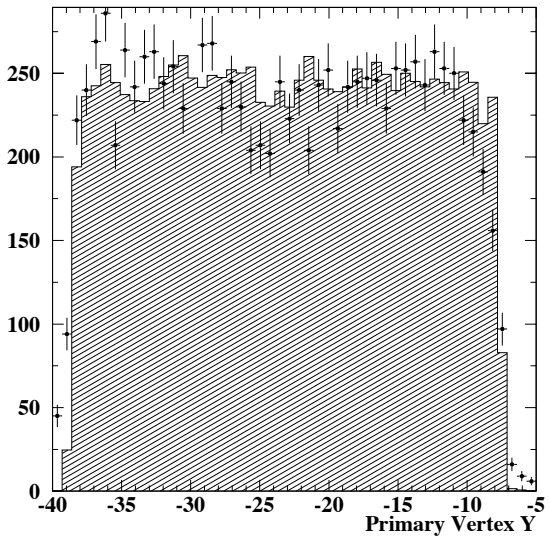


(b) Y Position (cm)

Figure 6.4: Distributions of the X and Y positions of the primary vertex

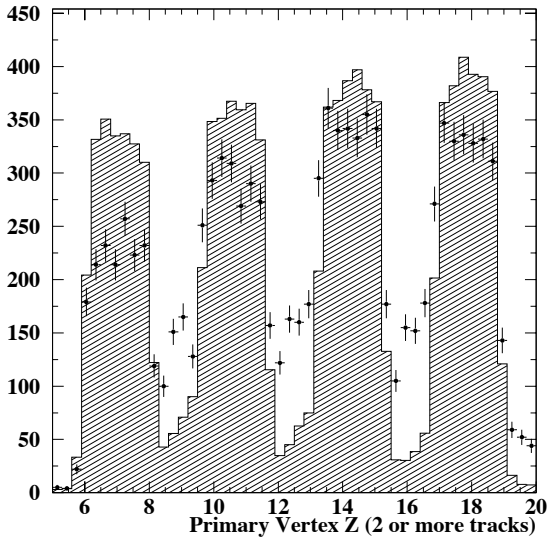


(a) All Primary Vertices

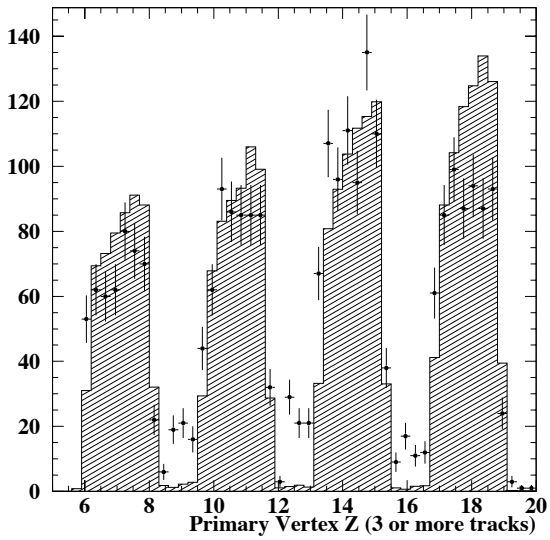


(b) Primary Vertices with 3 or more Tracks

Figure 6.5: Distributions of the Z position of primary vertex (cm)

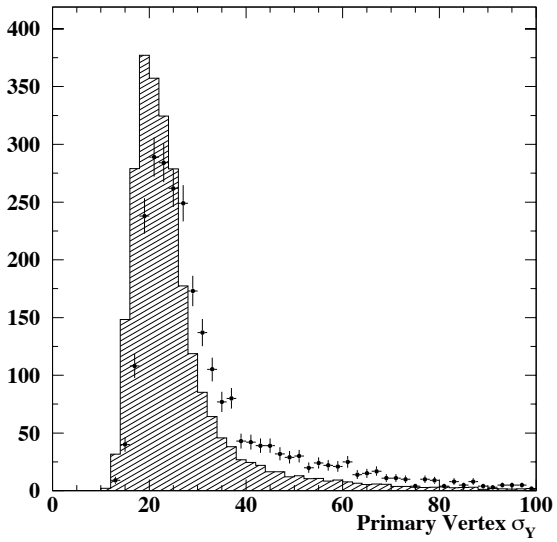


(a) $\sigma_Y$ ($\mu m$)

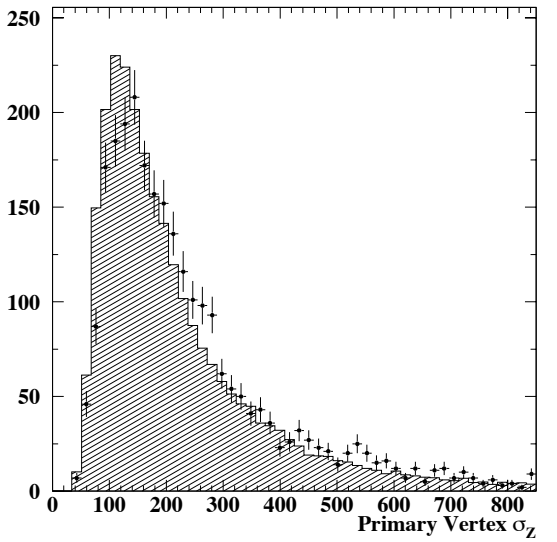


(b) $\sigma_Z$ ($\mu m$)

Figure 6.6: Distributions of the reconstructed uncertainties in the position of the primary vertex

The $\chi^2$ contribution (and $\chi^2$ probability) of each track in the Primary Vertex is shown in Figure 6.7

Figure 6.8 shows the difference between the reconstructed primary vertex position and the true value as obtained from the Monte Carlo. Both distributions have been fitted to a gaussian on top of a polynomial background and indicate a resolution from the central gaussian of $19\mu m$ in Y and $78\mu m$ in Z. The resolution is better in the Y direction due to the orientation of the strips and the fact that on average the tracks produced in the neutrino interaction tend to be produced at small angles to the Z axis and thus constrain the Z position by a lesser amount.

A test of the accuracy of the vertex reconstruction and error estimation can be obtained by plotting the "pull" variable, which is the ratio:

$$Pull(x) = \frac{x_{reconstructed} - x_{MonteCarlo}}{\sigma_x} \tag{6.24}$$

This variable should be normally distributed with a mean of 0 and a width of 1 (see Fig. 6.9).

### 6.4.2 Impact Parameter

During a $\nu_\mu$ charged current interaction, the neutrino is converted into a muon at a certain point in space, which is the same point as that where the hadronic jet is produced.

If a reconstructed event contains a muon in a primary vertex then this fact can be used to test the physical resolution of the detector.

The muon can be removed from the vertex and the vertex refitted so that the position is only dependent upon the tracks comprising the hadronic jet. The muon track is then extrapolated to this new vertex position and the impact paramater measured. The true value of the impact parameter should, of course, be exactly zero. However, due to measurement errors and the effects of multiple scattering it will actually be approximately gaussian in shape, centred at zero with a width which is determined by the resolution of the detector.

Figure 6.10 shows the measured impact parameter and impact parameter significance which is defined in Figures 1.6 and 1.7. The small non-Gaussian tails in the impact parameter significance plot are probably due to neglecting the fluctuations in the energy loss in the covariance matrix $Q_k$ used in the track fit.

Figures A.1- A.4 show a typical reconstructed $\nu_\mu$ charged current interaction from the 1998 run.

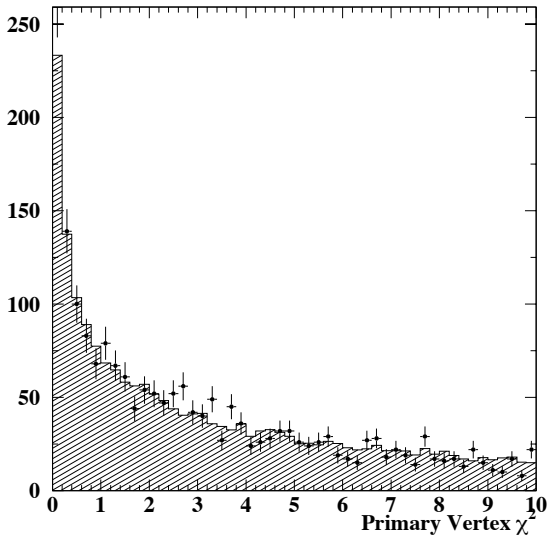


(a) $\chi^2$

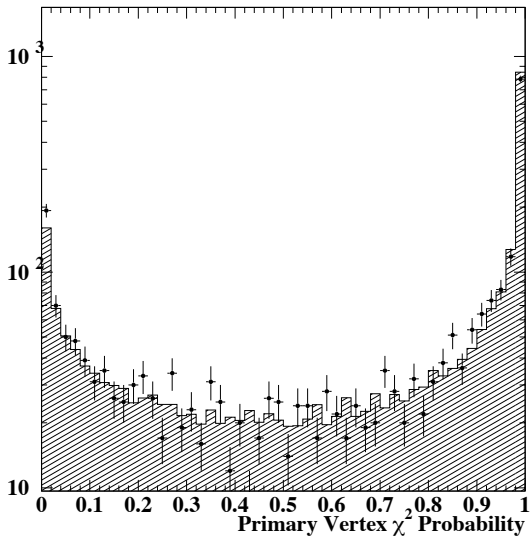


(b) $\chi^2$ probability

Figure 6.7: Distributions of the SiTrack $\chi^2$ and the $\chi^2$ probability in primary vertex

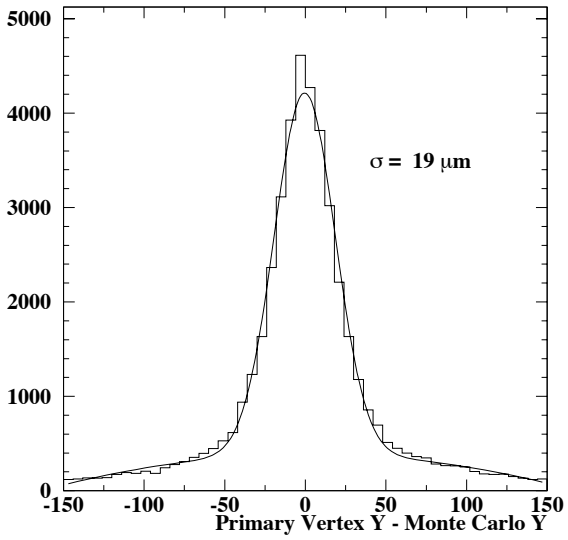


(a) $Y_{rec} - Y_{MC}$ $(\mu m)$

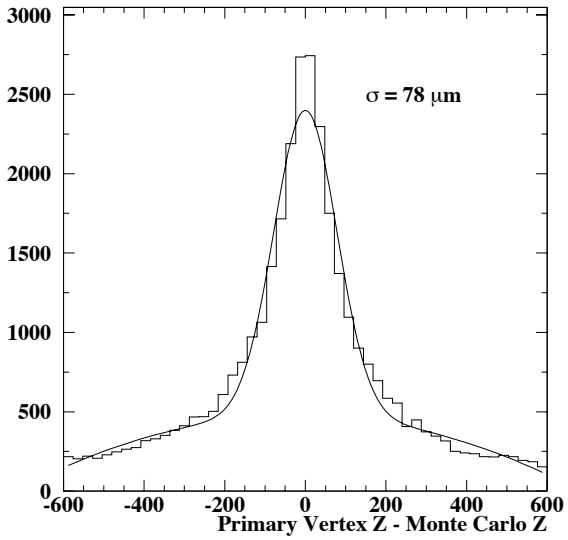


(b) $Z_{rec} - Z_{MC}$ $(\mu m)$

Figure 6.8: Distributions of the position accuracy of the reconstructed primary vertex

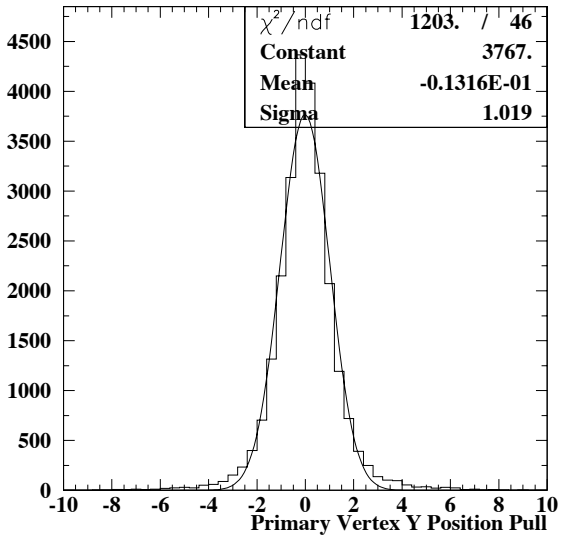


(a) Pull on Y Position

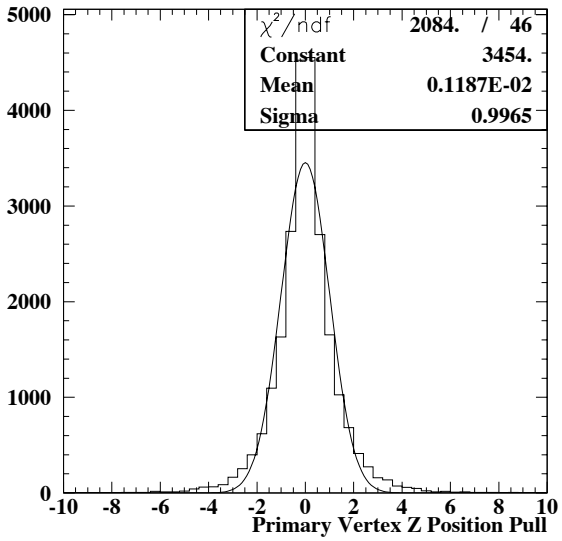


(b) Pull on Z Position

Figure 6.9: Distributions of the pulls on primary vertex position

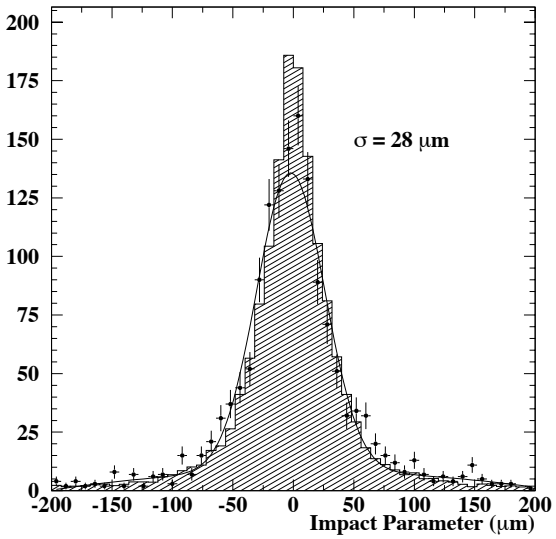


(a) Impact parameter ($\mu m$)

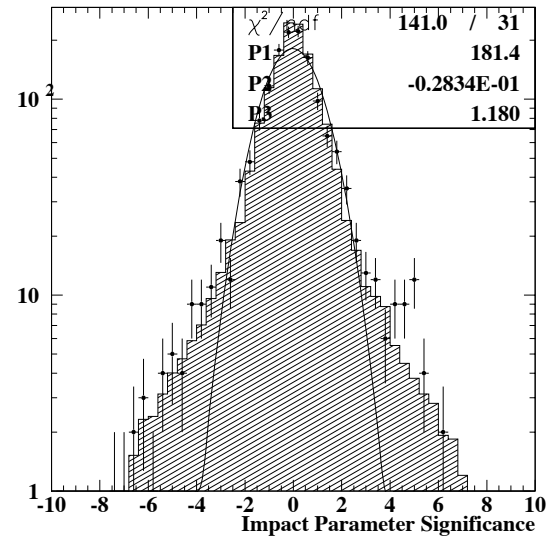


(b) Impact parameter significance

Figure 6.10: Distributions of the Impact parameter and Impact parameter significance

### 6.4.3 Kinematics

The kinematic variables defined in Section 1.2 are calculated when an event is reconstructed with a primary vertex which contains a muon. The event is assumed to be a charged current interaction.

The total energy visible in the event shown in Figure 6.11 is calculated as the total energy of the tracks reconstructed in STAR (under the assumption that tracks without any particle identification information are pions) plus the total energy of clusters in the electromagnetic calorimeter plus the energy of any $V^0$ vertices reconstructed as photon conversions or $K_s^0$ decays reconstructed in the drift chambers. Figure 6.11 also shows the reconstructed energy transferred to the hadronic system ($\nu$) as defined in Eq. 1.9.

The square of the 4-momentum transferred to the hadronic jet ($Q^2$) is calculated from Eq. 1.10 and is shown in Fig 6.12 which also shows $W^2$, calculated from Eq. 1.15.

Figure 6.13 shows the reconstructed momentum of the leading $\mu^{\pm}$ and the total reconstructed momentum of the hadronic jet.

Figure 6.14 shows $X_{bj}$ and $Y_{bj}$ , calculated from Eq. 1.12 and Eq. 1.13.

Figure 6.15 shows the distribution of momentum times electric charge for STAR tracks in the hadronic jet and those not in the primary vertex.

It can be seen that although there is a reasonable agreement between data and Monte Carlo, the tails of the variables such as $\nu$, $Q^2$, $y_{Bj}$ etc., which are formed from the reconstructed hadronic jet, do not agree well. This lack of agreement is due to differences between the fragmentation in Monte Carlo and data as well as possible nuclear reinteractions.

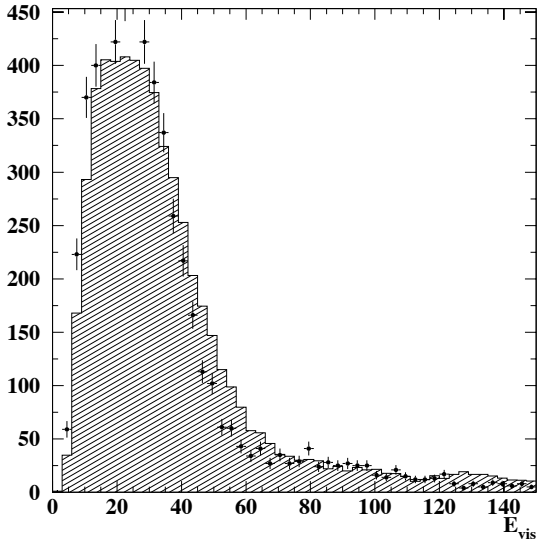


(a) $E_{vis}$ (GeV)

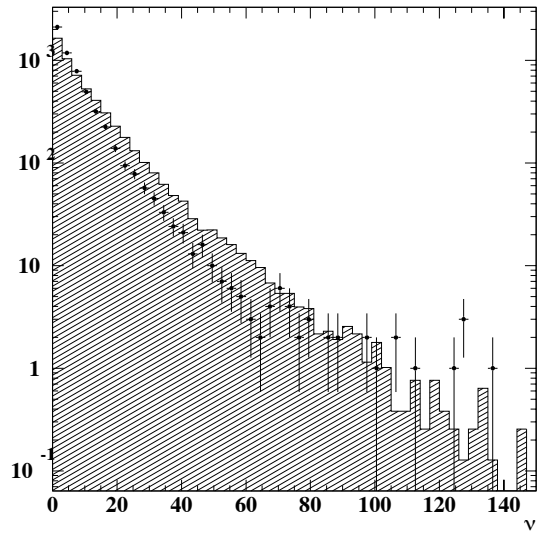


(b) $\nu$ (GeV)

Figure 6.11: Distributions of the reconstructed visible energy and $\nu$

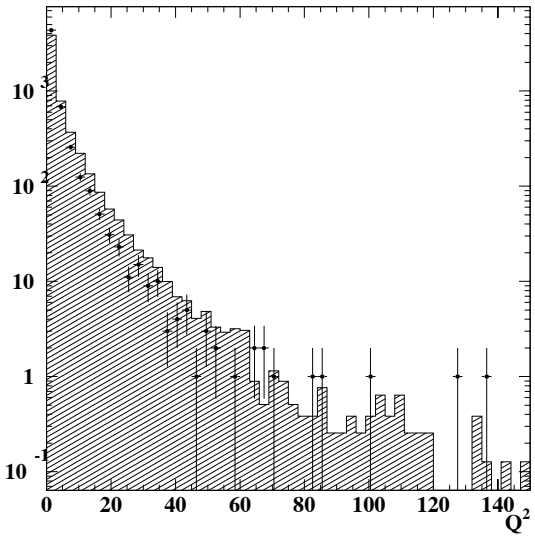


(a) $Q^2$ (GeV$^2$)

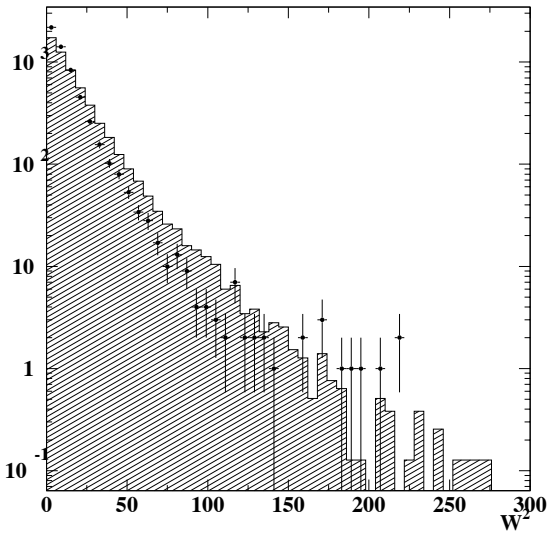


(b) $W^2$ (GeV$^2$)

Figure 6.12: Distributions of the reconstructed $Q^2$ and $W^2$

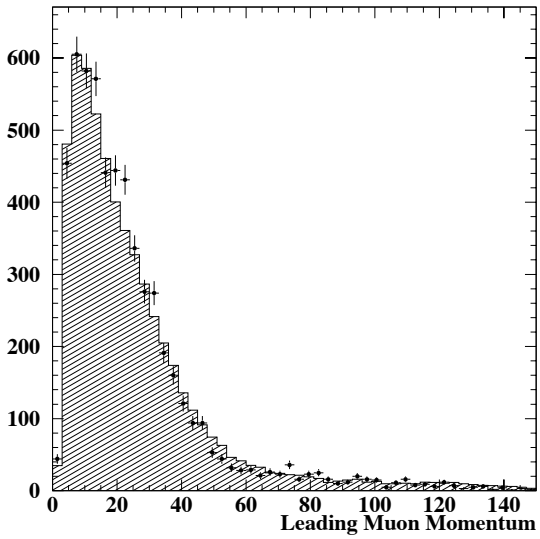


(a) Momentum of the leading $\mu^{\pm}$ (GeV)

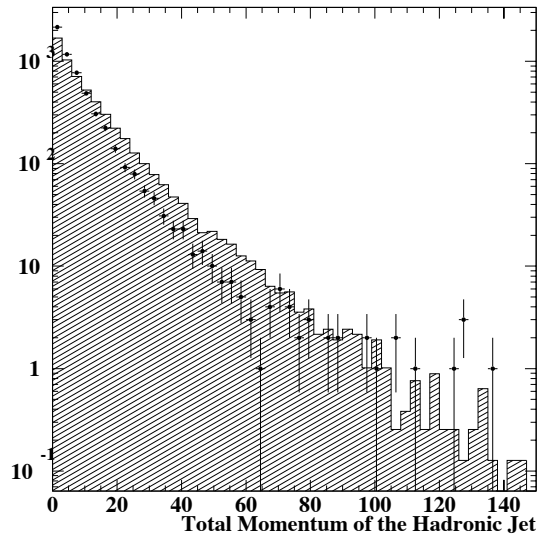


(b) Total momentum of the hadronic jet (GeV)

Figure 6.13: Distributions of the reconstructed $\mu^{\pm}$ momentum and total momentum of the hadronic jet

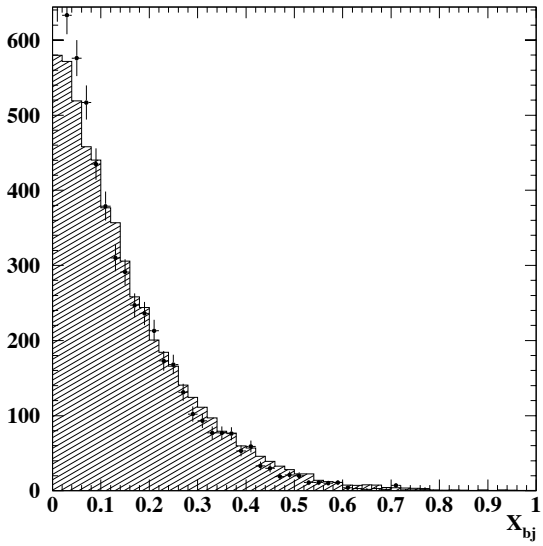


(a) $X_{bj}$

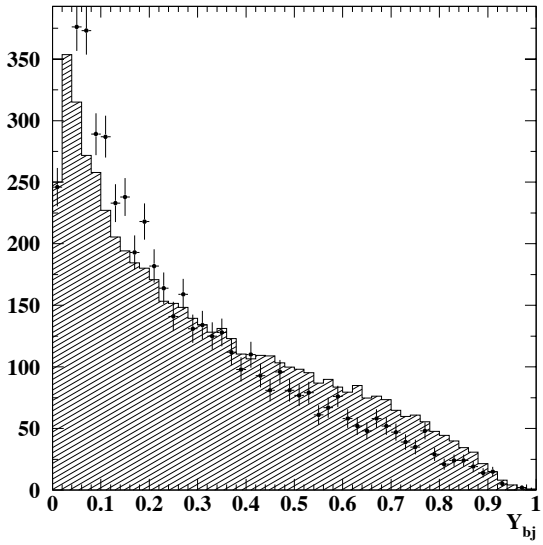


(b) $Y_{bj}$

Figure 6.14: Distributions of the reconstructed variables $X_{bj}$ and $Y_{bj}$

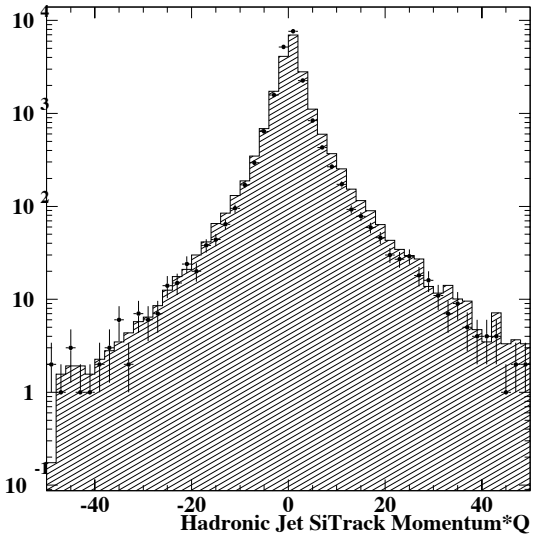


(a) STAR tracks in the hadronic jet

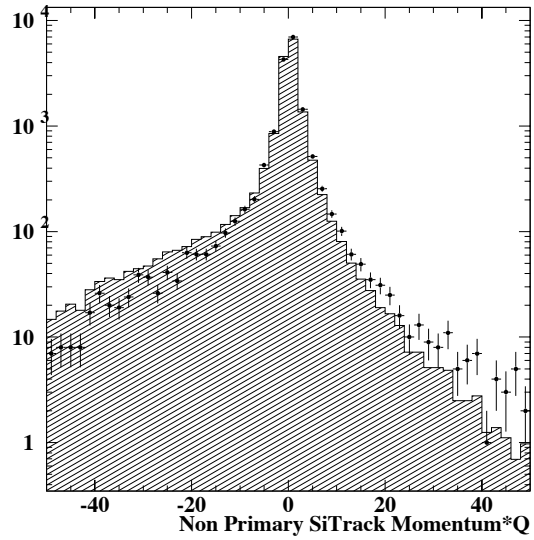


(b) STAR tracks not in the primary vertex

Figure 6.15: Distributions of the momentum × charge for SiTracks in the hadronic jet and those not in the primary vertex

# Chapter 7

# Charm Search

## 7.1 Introduction

During approximately 5% of charged current interactions, a charm quark is produced. This charm quark is mainly bound into D mesons which subsequently decay with a typical lifetime of the order of $10^{-13}s$. This chapter will illustrate the method used for the search for the production and decay of these mesons in the STAR detector.

## 7.2 Charm Production and Decay Topology

When the incoming neutrino strikes a valence d quark, or a d or s quark from the sea, it is possible for a charm quark to be produced, which will be hadronised and form part or all of the hadronic jet. This charmed meson will then travel between approximately $100\mu m$ and $4mm$ before it decays (see Fig 7.1.

## 7.3 Constrained Kinematical Fit

In order to test a number of hypotheses, it is necessary to perform a constrained fit on the momenta of the tracks under investigation. Energy and momentum under the hypothesis must be conserved, so they form the basis of several constraints. As there is a topological criterion which must be satisfied, it can be added as a constraint to the fit.

As the vertex positions obtained in STAR are only 2 dimensional, the topological constraint can only affect the y and z momenta of the decay tracks.

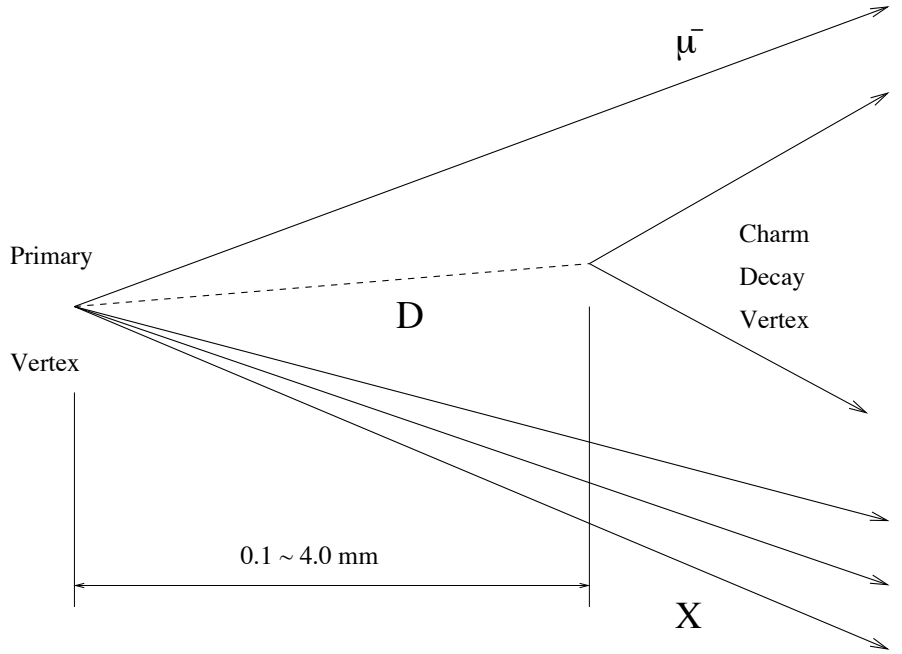


Figure 7.1: Charm production and decay

For the particular case of STAR, the constraint equations used were:

$$f_1 = P - \sum_{i=1}^{n} \sqrt{p_{x_i}^2 + p_{y_i}^2 + p_{z_i}^2} \tag{7.1}$$

$$f_2 = \sqrt{P^2 + M^2} - \sum_{i=1}^{n} \sqrt{p_{x_i}^2 + p_{y_i}^2 + p_{z_i}^2 + m_i^2} \tag{7.2}$$

$$f_3 = \cos^{-1}\left( \frac{\tan\Theta_{yz} \sum_{i=1}^{n} p_{y_i} + \sum_{i=1}^{n} p_{z_i}}{\sqrt{\sum_{i=1}^{n} p_{y_i}^2 p_{z_i}^2 \left[1 + \tan\left(\Theta_{yz}{}^2\right)\right]}} \right) \tag{7.3}$$

Where $p_{x_i}$, $p_{y_i}$ and $p_{z_i}$ are the x y and z momenta of the decay products. The masses of each track in this hypothesis are $m_i$. $P$ is the unknown total momentum of the charmed particle and $\Theta_{yz}$ is the measured angle in the y-z plane that the particle followed between production and decay, as measured by the vertex positions in STAR (see Fig 7.2).

For the purposes of the constrained fit, the measured variables (in this case the measured momenta of each particle and the measured angle $\Theta_{yz}$) are denoted by $x_i$ with the original unfitted quantities specifically referred to as

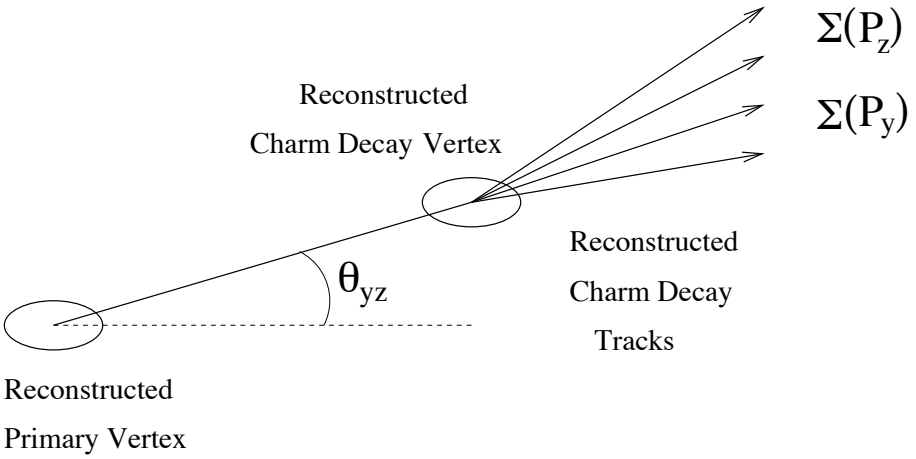


Figure 7.2: Definitions of variables used in charm reconstruction

$x_i^0$. The error matrix of the measured quantities is called $G_x^{-1}$. The unknown variables (in this case only the total momentum of the charmed meson) are referred to as $y_j$.

The fit uses the method of least squares based on the assumption that the variables are distributed normally and that the best set of variables minimises the chi-squared

$$\chi^2 = \sum_{j=1}^{J}\sum_{i=1}^{I}(x_i - x_i^0)(G_x)_{ij}(x_j - x_j^0). \tag{7.4}$$

subject to the constraint that the variables satisfy the equations:

$$f_k(x, y) = 0 \tag{7.5}$$

In order to achieve this, it is possible to re-express the fit in a more general way such that the chi-squared minimised is:

$$\chi^2 = \sum_{j=1}^{J}\sum_{i=1}^{I}(x_i - x_i^0)(G_x)_{ij}(x_j - x_j^0) + \sum_{k=1}^{K} 2\alpha_k^T f_k(x, y) \tag{7.6}$$

This requires the solution of the equations:

$$\frac{d\chi^2}{dx} = 2\left[(x - x^0)^T G_x + \alpha^T f_x(x, y)\right] = 0 \tag{7.7}$$

$$\frac{d\chi^2}{dy} = 2\alpha^T f_y = 0 \tag{7.8}$$

$$\frac{d\chi^2}{d\alpha} = 2f(x, m_i) = 0 \tag{7.9}$$

Where $f_x = \frac{df(x,y)}{dx}$, $f_y = \frac{df(x,y)}{dy}$ and $m_i$ the mass.

For the $\nu^{th}$ iteration of the fit, the constraint equations can be expanded as follows

$$f^\nu + f_x^\nu(x^{\nu+1} - x^\nu) + f_y^\nu(y^{\nu+1} - y^\nu) = 0 \tag{7.10}$$

The value of $\alpha$ for the next iteration can be determined from

$$\alpha^{\nu+1} = S^{-1}\left[R + f_y^\nu(y^{\nu+1} - y^\nu)\right] \tag{7.11}$$

with R and S defined by

$$R = f^\nu + f_x^\nu(x^0 - x^\nu) \tag{7.12}$$

$$S = f_x^\nu G_x^{-1}(f_x^\nu)^T \tag{7.13}$$

It is thus possible to determine the new values of $x$ and $y$

$$x^{\nu+1} = x^0 - G_x^{-1}(f_x^\nu)^T\alpha^{\nu+1} \tag{7.14}$$

$$y^{\nu+1} = y^\nu - \left(\left(f_y^\nu\right)^T S^{-1} f_y^\nu\right)^{-1}\left(f_y^\nu\right)^T S^{-1} R \tag{7.15}$$

and the new chi-squared can be more easily evaluated as

$$\chi^2 = \left(\alpha^{\nu+1}\right)^T\left[R + f_y\left(y^{\nu+1} - y^\nu\right)\right] \tag{7.16}$$

The iteration is repeated until some criteria is satisfied. In this case, the requirements were that the change in chi-squared between iterations be less than 0.1% and that the sum of the functions $f_1$, $f_2$ and $f_3$ be less than 0.0001.

Once the fit has converged on a solution, the chi-squared can be tested by calculating the chi-squared probability.

## 7.4 Charm Decays

The majority of charmed particles produced in $\nu_\mu$ charged current interactions are $D^0$, $D^+$and $D_s^+$, some of which are the result of the decay of higher energy states such as $D^{0^*}$and $D^{+^*}$. Tables 7.1, 7.2, 7.3 and 7.4 show the different decay modes of the $D^0$, $D^+$, $D_S^+$ and $D^*$ respectively that

were reconstructed in the analysis. The branching fractions listed are those from [32]. It should be noted that the branching fractions for those decay modes containing a $K^0_S$ have been halved as the PDG value lists the fraction for $K^0$ or $\overline{K^0}$, this is necessary as NOMAD can only identify $K^0_S$.

### 7.4.1 Decay Modes

Table 7.1 shows the different decay modes of the $D^0$, table 7.2 shows the decay modes of the $D^+$, table 7.3 shows the decay modes of the $D^+_S$ and table 7.4 shows the decay modes of the $D^*$ that were reconstructed in this analysis.

| Decay | Branching Ratio (from [32]) |
|---|---|
| $D^0 \longrightarrow K^-\pi^+\pi^0\pi^0$ | $\sim 15\%$ |
| $D^0 \longrightarrow K^-\pi^+\pi^0$ | $\sim 13.9\%$ |
| $D^0 \longrightarrow \pi^-\pi^+K^0_S\pi^0\pi^0$ | $\frac{\sim 10.6\%}{2} = 5.3\%$ |
| $D^0 \longrightarrow \pi^-\pi^+K^0_S\pi^0$ | $\frac{\sim 10.0\%}{2} = 5.0\%$ |
| $D^0 \longrightarrow \pi^-\pi^+K^0_S$ | $\frac{\sim 5.4\%}{2} = 2.7\%$ |
| $D^0 \longrightarrow K^-\pi^+$ | $\sim 3.83\%$ |
| $D^0 \longrightarrow \pi^-\pi^+\pi^0$ | $\sim 1.6\%$ |
| $D^0 \longrightarrow K^-\pi^+\pi^+\pi^-$ | $\sim 7.49\%$ |
| $D^0 \longrightarrow K^-\pi^+\pi^+\pi^-\pi^0$ | $\sim 4.0\%$ |
| $D^0 \longrightarrow \pi^-\pi^+\pi^+\pi^-\pi^0$ | $\sim 1.9\%$ |

Table 7.1: $D^0$ decay modes reconstructed in this analysis

| Decay | Branching Ratio (from [32]) |
|---|---|
| $D^+ \longrightarrow K^-\pi^+\pi^+$ | $\sim 9.0\%$ |
| $D^+ \longrightarrow K^-\pi^+\pi^+\pi^0$ | $\sim 6.4\%$ |
| $D^+ \longrightarrow K^-K^+\pi^+\pi^0$ | $\sim 1.1\%$ |
| $D^+ \longrightarrow \pi^-\pi^+\pi^+K^0_S$ | $\frac{\sim 1.2\%}{2} = 0.6\%$ |
| $D^+ \longrightarrow K^-\pi^+\pi^+\pi^0\pi^0$ | $\sim 2.2\%$ |
| $D^+ \longrightarrow \pi^-\pi^+\pi^+\pi^0$ | $\sim 1.9\%$ |
| $D^+ \longrightarrow \pi^-\pi^+\pi^+\pi^0K^0_S$ | $\frac{\sim 5.4\%}{2} = 2.7\%$ |

Table 7.2: $D^+$ decay modes reconstructed in this analysis

| Decay | Branching Ratio (from [32]) |
|---|---|
| $D_s^+ \longrightarrow K^+K^-\pi^+\pi^0$ | $\sim 9\%$ |
| $D_s^+ \longrightarrow K^+K^-\pi^+$ | $\sim 4.4\%$ |
| $D_s^+ \longrightarrow K^-\pi^+\pi^+K_S^0$ | $\frac{\sim 4.3\%}{2} = 2.15\%$ |
| $D_s^+ \longrightarrow K^+\pi^+\pi^-$ | $\sim 1.0\%$ |
| $D_s^+ \longrightarrow \pi^-\pi^+\pi^+$ | $\sim 1.0\%$ |

Table 7.3: $D_S^+$ decay modes reconstructed in this analysis

| Decay | Branching Ratio (from [32]) |
|---|---|
| $D^{0^*} \longrightarrow D^0\pi^0$ | $\sim 61.9\%$ |
| $D^{0^*} \longrightarrow D^0\gamma$ | $\sim 38.1\%$ |
| $D^{+^*} \longrightarrow D^0\pi^+$ | $\sim 67.7\%$ |
| $D^{+^*} \longrightarrow D^+\pi^0$ | $\sim 30.7\%$ |

Table 7.4: $D^*$ decay modes reconstructed in this analysis

Each of the decay modes above has been chosen to fulfill a number of criteria. The decay must produce at least two charged tracks, so that a second vertex can be reconstructed using STAR. It was also required that the decay mode only produce particles that can be fully reconstructed in NOMAD, hence the inclusion of modes with $\gamma$, $\pi^0$ and $K_S^0$. The following section details the reconstruction of these last three.

Charmed mesons are not the only charmed particles produced in neutrino interactions, in particular the $\Lambda_c^+$ has been observed by E531 [65]. These events were observed in quasi-elastic interactions: $\nu_\mu N \longrightarrow \mu^-\Lambda_c^+$. A study with Monte Carlo indicated that due to the nature of the production and low efficiency of reconstruction, it was not worthwhile to attempt to reconstruct $\Lambda_c^+$ in the STAR data.

In the following sections, the plots show a comparison of the 1998 filtered data with either a sample of charm enriched Monte Carlo events for determination of efficiency, or non-enriched $\nu_\mu$ CC Monte Carlo events for background determination.

## 7.5 Reconstruction of $\gamma$, $\pi^0$ and $K_S^0$

Photons can be identified in NOMAD through 2 separate means. Firstly, the photon may travel through STAR, the drift chambers and be recorded

in the electromagnetic calorimeter (ECAL), in which case it is assumed that the photon originated at the primary vertex and, using the energy recorded in the ECAL, the momentum can be determined. It is also possible for the photon to convert inside the drift chambers producing an electron and positron which will then be recorded by the drift chambers.

The decay of a $\pi^0$ produces two photons, so having reconstructed photons, it is possible to test the invariant masses of pairs of photons to see if any are consistent with the decay of a $\pi^0$.

Several decay modes of the charmed mesons under study include a $K^0$ or a $\overline{K^0}$. Half of these will appear as $K_L^0$ which cannot be identified in NOMAD, however the other half can be detected when they decay into two charged pions, which occurs approximately 69% of the time. It is for this reason that the decay modes listed previously only indicated $K_S^0$.

### 7.5.1 $V^0$ Reconstruction

The searches for photon conversions and $K_S^0$ are carried out simultaneously. If the drift chamber reconstruction proceeded completely to the stage of identifying secondary vertices, then each vertex which is labelled as being a possible $V^0$ decay is tested for four hypotheses:

$$\gamma \longrightarrow e^+e^- \tag{7.17}$$

$$K_S^0 \longrightarrow \pi^+\pi^- \tag{7.18}$$

$$\Lambda^0 \longrightarrow P\pi^- \tag{7.19}$$

$$\overline{\Lambda^0} \longrightarrow \overline{P}\pi^+ \tag{7.20}$$

For each hypothesis, the difference between the invariant mass and the true value of the mass of the parent particle is compared to the uncertainty of the reconstructed invariant mass. Those combinations which are within $3\sigma$ of the true value and whose invariant mass is close to the true value are accepted as candidates. If more than one hypothesis survives, then that which has the smallest deviation from the true mass is accepted.

A useful method of separating the different hypotheses for a $V^0$ is the Armenteros plot. This plot displays $p_t^+$, the transverse momentum of the positive track with respect to the total momentum of the $V^0$, versus the asymmetry variable:

$$\alpha = \frac{p_l^+ - p_l^-}{p_l^+ + p_l^-}. \tag{7.21}$$

where $p_l^{\pm}$ are the longitudinal momenta of the positive and negative tracks.

This plot shows photons in the low $p_t^+$ region as a photon conversion produces an electron and positron which are initially travelling parallel to each other. The kinematics of the $K_S^0$ and $\Lambda$ decays results in them occupying well defined regions in the plane, with some overlap.

The Armenteros plot in figure 7.3 shows reconstructed photons in black, $K_S^0$ in red, $\Lambda$ in blue and $\overline{\Lambda}$ in green.

Figure 7.4 shows the reconstructed mass for the photon hypothesis for all combinations and that for good photon conversions.

Figure 7.5 shows the reconstructed mass for the $K_S^0$ hypothesis for all combinations and that for good $K_S^0$ decays. The mass of the $K_S^0$ is reproduced by the plot.

Once a $V^0$ has been identified as either a photon or a $K_S^0$, then the constrained fit is performed to determine the true momentum of the parent particle.

### 7.5.2 ECAL $\gamma$ Reconstruction

Each cluster in the ECAL which has been determined by the standard NOMAD reconstruction to be a photon from the primary vertex is kept for later use if the total energy deposited is greater than 100 MeV.

### 7.5.3 $\pi^0$ Reconstruction

Having reconstructed photons through two means, it is now possible to search for $\pi^0$ decays to two photons.

The invariant mass of each possible combination of two photons is tested against the known mass. The constrained fit is again used to determine the best momenta for the $\pi^0$ and as an additional cut, the $\chi^2$ probability is required to be greater than 0.05.

Figure 7.6 shows the reconstructed mass for the $\pi^0$ hypothesis for all combinations and that for good $\pi^0$ decays. The mass of the $\pi^0$ is reproduced by the plot.

## 7.6 Reconstruction of $D^0$, $D^+$ and $D_s^+$

The search for charmed meson decays proceeds by looking for each of the decay modes listed in Tables 7.1- 7.3 in turn, applying several cuts and if any modes survive, selecting that with the best $\chi^2$.

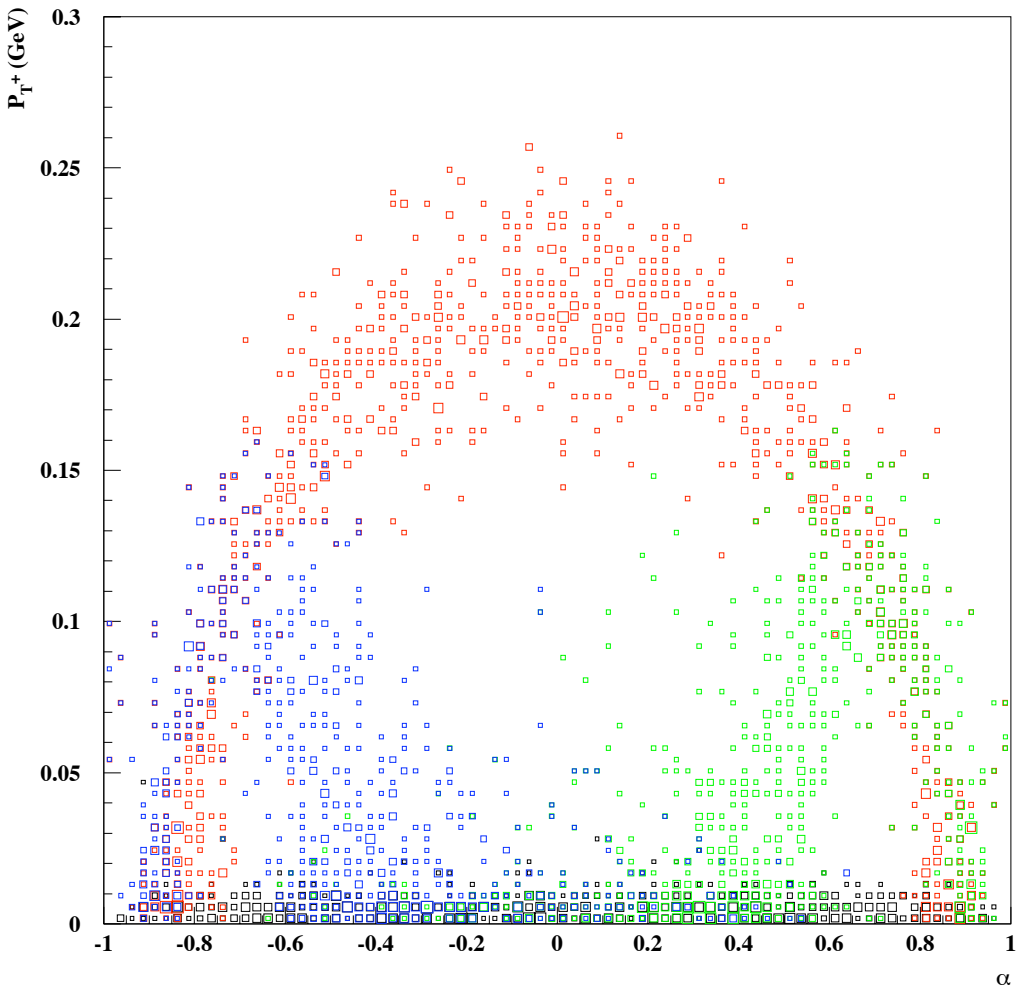


Figure 7.3: Armenteros Plot

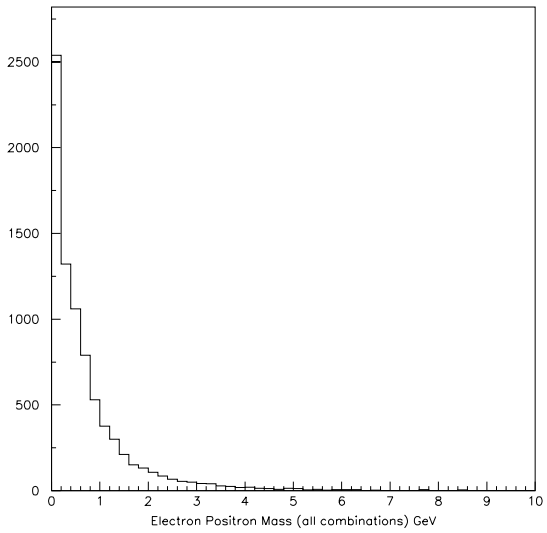


(a) All combinations

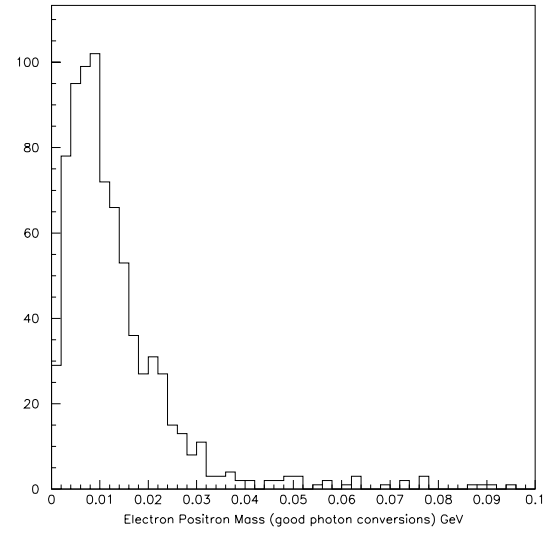


(b) Good combinations

Figure 7.4: Distributions of the reconstructed $V^0$ mass for the $\gamma$ hypothesis (GeV)

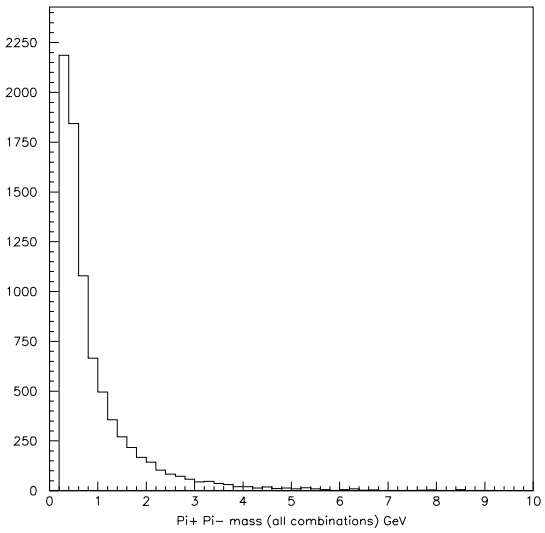


(a) All combinations

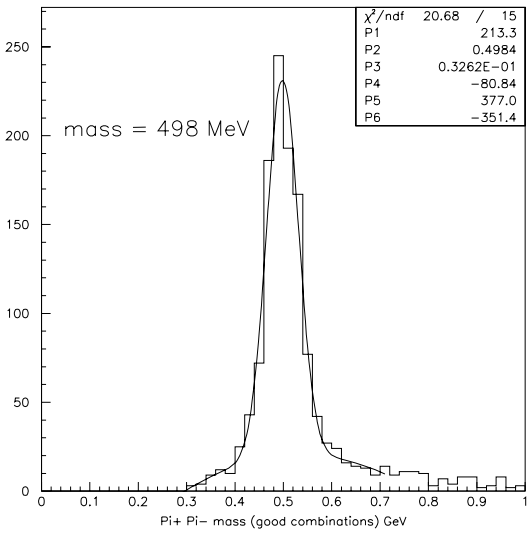


(b) Good combinations

Figure 7.5: Distributions of the reconstructed $V^0$ mass for the $K_S^0$ hypothesis (GeV)

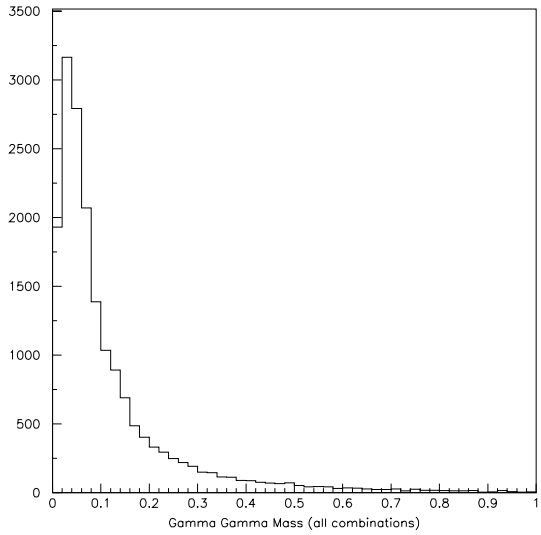


(a) All combinations

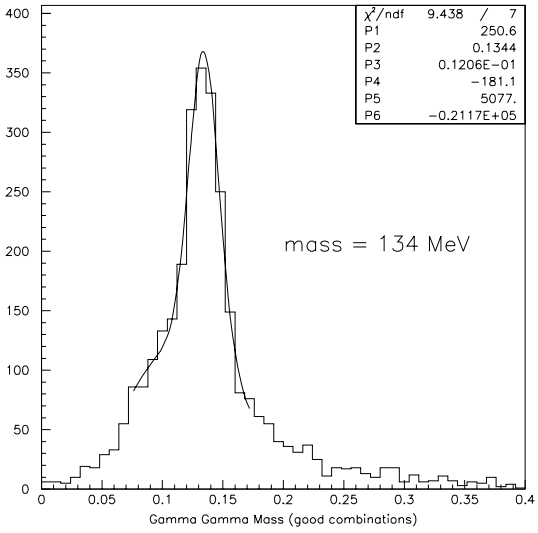


(b) Good combinations

Figure 7.6: Distributions of the reconstructed mass for $\pi^0$ hypothesis (GeV)

In order for an event to be considered, it must have a reconstructed primary vertex that contains a muon of the correct sign (that is a $\mu^-$ when reconstructing $\nu_\mu$ and a $\mu^+$ when reconstructing $\overline{\nu_\mu}$) and at least 4 tracks in total (2 for the primary vertex, of which one is the muon and 2 tracks for the charm decay).

Two separate lists (one for positive, the other for negative tracks) are kept of charged tracks that could possibly be used to form a charm decay vertex. These tracks must either have no particle identification, or have been identified as pions.

The charged tracks must have a momentum of more than 200 MeV. Those tracks that pass this cut are subjected to a second particle identification test for the particular hypothesis under test.

This test just checks that a track positively identified as a pion by the reconstruction is not included in the sample of potential kaons. The reconstruction does not identify charged kaons, so tracks that have been reconstructed without a definite particle identification are used for both pion and kaon hypotheses.

For each charm decay mode, each combination of positive and negative tracks along with reconstructed neutrals is tested to see if they are consistent with a charm decay.

For each combination of charged tracks and neutrals in a given decay mode, the invariant mass is calculated using the reconstructed momenta and mass assignments for that hypothesis and a STAR vertex is built using the charged tracks. The primary vertex may have contained one or more of the tracks under consideration and so this vertex is rebuilt without these tracks. From these two vertices, the line of flight of the decay hypothesis is known and can then be used, along with the reconstructed momenta of the decay tracks, in the constrained fit.

The constrained fit returns the $\chi^2$ and $\chi^2$ probability as well as the fitted total momentum of the D meson and $P_D^*$, the total momentum of the decay products in the rest frame of the D meson according to the fit.

These variables, along with several others described below, are used to remove (non-charm) background and incorrect decay modes.

### 7.6.1 Constrained Fit

The constrained fit returns a $\chi^2$ value which is used to remove background. If several decay hypotheses in an event survive all the cuts, then the hypothesis with lowest $\chi^2$ is chosen.

Combinations with a $\chi^2$ less than 20 were kept.

Figure 7.7 shows the $\chi^2$ of the constrained fit for all combinations and those that pass all the cuts defined in sections 7.6.1- 7.6.10.

### 7.6.2 Invariant Mass

The reconstructed invariant mass is compared with the known value from [32] and combinations whose reconstructed mass is less than 150 MeVfrom the known value are kept.

The distributions of reconstructed mass minus the known mass are shown in Figure 7.8.

From the uncertainties in the reconstructed momenta of the charged tracks and neutrals, it is possible to determine the uncertainty in the invariant mass calculated from these momenta.

Combinations with an uncertainty in the mass of less than 160 MeVwere kept. The distributions of uncertainty in the invariant mass are shown in Figure 7.9.

### 7.6.3 Distance of Flight

From the Monte Carlo, it is seen that the distance travelled by the D mesons between production and decay rarely exceeds $4mm$. Beyond this distance the vast majority of combinations are background due to poorly reconstructed tracks, or tracks that have undergone significant multiple scattering. Combinations whose distance of flight in the Z direction exceeds $4mm$ are excluded.

The distributions of distance of flight in the Z direction are shown in Figure 7.10

### 7.6.4 Uncertainty in the Decay Vertex Position

In order to remove poorly reconstructed vertices, or those vertices where the opening angle of the tracks is very low, and hence the reconstructed Z position is poorly known, a cut was made on the reconstructed uncertainty in the Z position ($\sigma_Z$).

Events with a value of $\sigma_Z$ greater than $400\mu m$ were rejected.

The distributions of distance of $\sigma_Z$ are shown in Figure 7.11.

### 7.6.5 Reconstructed $c\tau$

If the distance travelled by the D meson between production and decay as well as the momentum are known, then it is possible to measure the lifetime of the meson. It is convenient to express this lifetime as the product $c\tau$

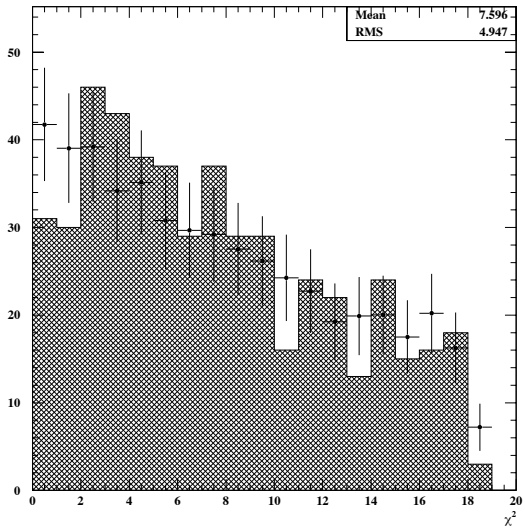


(a) All combinations

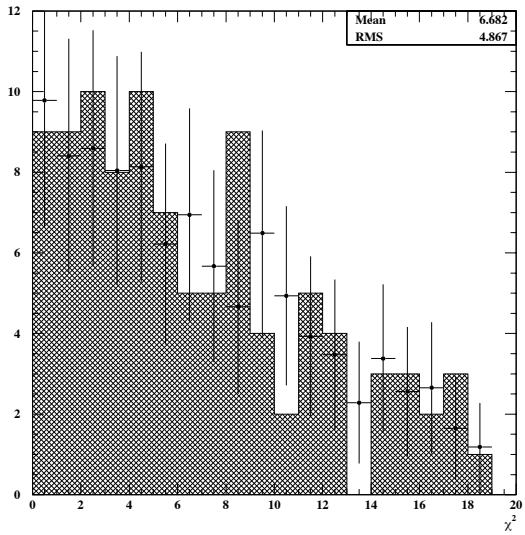


(b) Surviving combinations

Figure 7.7: Distributions of the $\chi^2$ returned by constrained fit

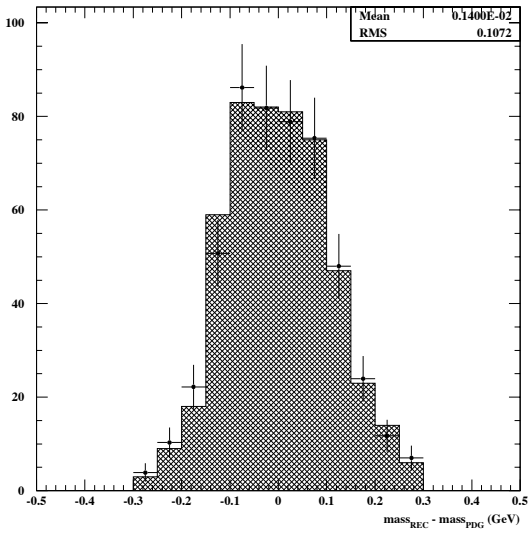


(a) All combinations

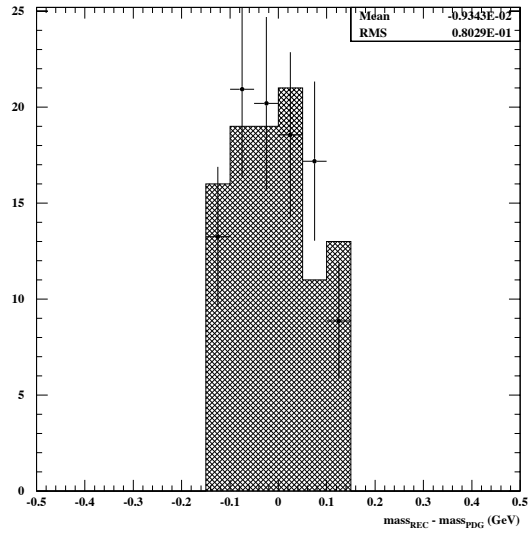


(b) Surviving combinations

Figure 7.8: Distributions of the difference between reconstructed mass and PDG mass (GeV)

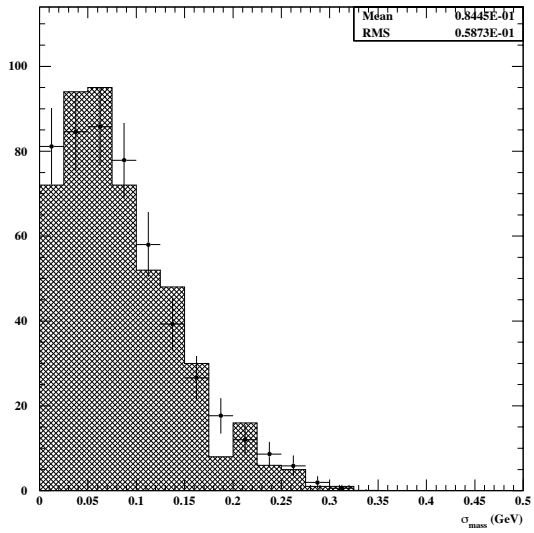


(a) All combinations

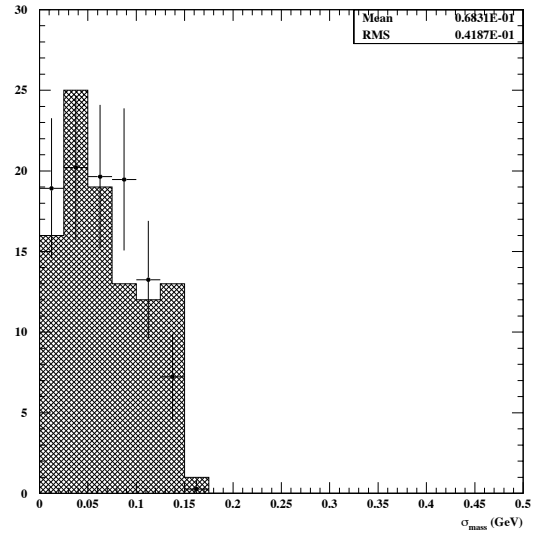


(b) Surviving combinations

Figure 7.9: Distributions of the uncertainty in invariant mass (GeV)

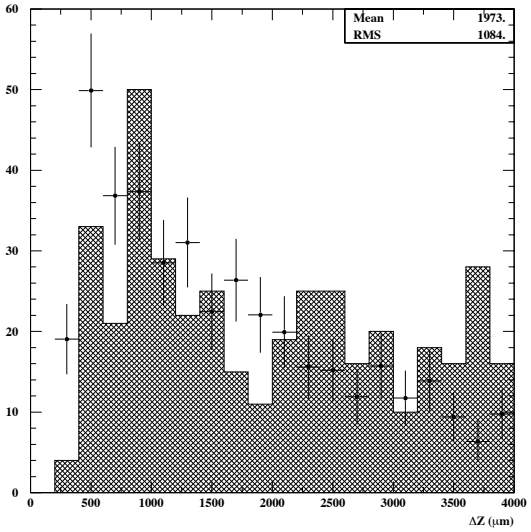


(a) All combinations

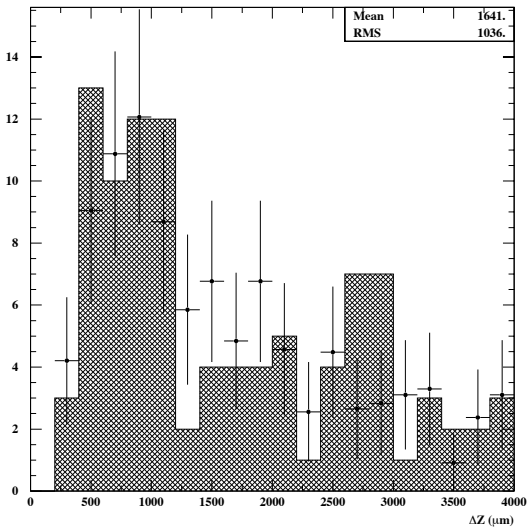


(b) Surviving combinations

Figure 7.10: Distributions of the distance of flight in the Z direction ($\mu m$)

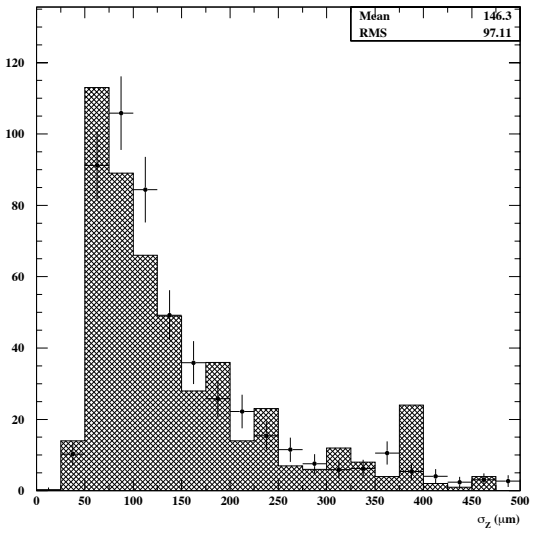


(a) All combinations

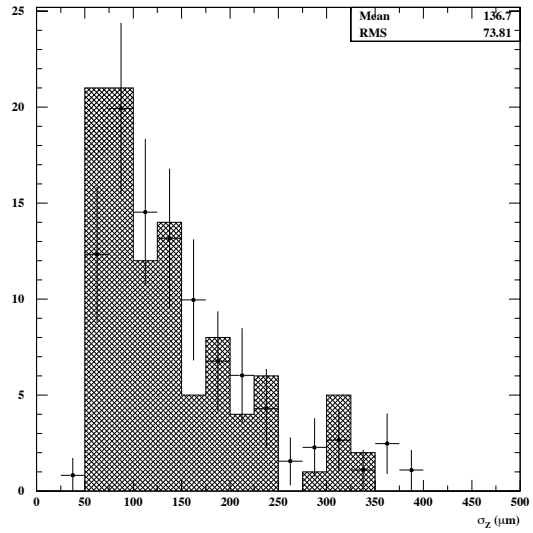


(b) Surviving combinations

Figure 7.11: Distributions of the reconstructed uncertainty in the Z position of the decay vertex ($\mu m$)

where $\tau$ is the lifetime of the meson and c the speed of light. If the measured distance of flight is $d$ and the Lorentz factors $\beta$ and $\gamma$ are determined from the reconstructed momentum, then the lifetime can be determined from:

$$c\tau = \frac{d}{\beta\gamma} \tag{7.22}$$

From the fitted momentum of the D meson and the distance of flight in the YZ plane as measured by the STAR vertices, it is possible to make an estimate of the $c\tau$ of the decay. A cut is made on the normalised $c\tau$, which is the reconstructed $c\tau$ divided by the known value from [32]. Events with a normalised value of $c\tau$ greater than 6 are rejected.

The distributions of distance of normalised $c\tau$ are shown in Figure 7.12.

### 7.6.6 Fitted Total Momentum

The constrained fit returns the total momentum of the D meson under the hypothesis under test. Combinations with a fitted momentum between 2 GeVand 40 GeVwere kept.

The distributions of fitted momentum are shown in Figure 7.13.

### 7.6.7 Fragmentation

On average, events in which charm is produced tend to be quite hard. A variable which tests this feature of the interaction is $P_{max}$ which is defined

$$P_{max} = \frac{P_{reconstructed}}{\sqrt{{E_{had}}^2 - {M_D}^2}} \tag{7.23}$$

Here $E_{had}$ is the visible hadronic energy and $M_D$ is the PDG value for the mass of the D meson in the hypothesis under test.

$P_{max}$ can range from low values, when the D meson carried a small fraction of the total hadronic energy to 1, if the only hadronic product is the D meson itself.

In order to select hard interactions, only combinations with $P_{max}$ greater than 0.5 are kept.

The distributions of $P_{max}$ are shown in Figure 7.14.

### 7.6.8 Total Momentum in Rest Frame

As described above, the constrained fit calculates the total momentum of the decay products in the rest frame ($P_D^*$) of the D meson, using the fitted total momentum and PDG mass to calculate the boost.

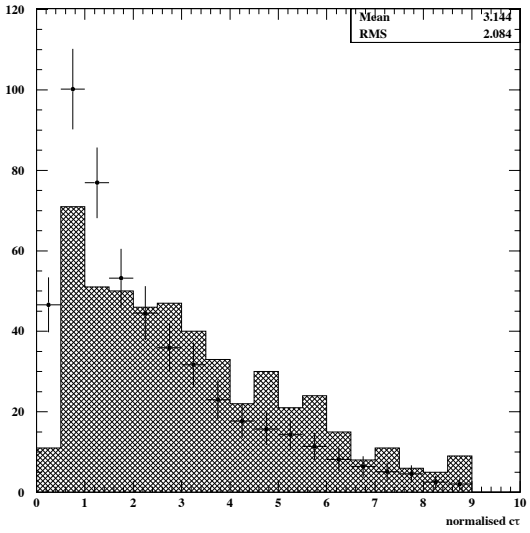


(a) All combinations

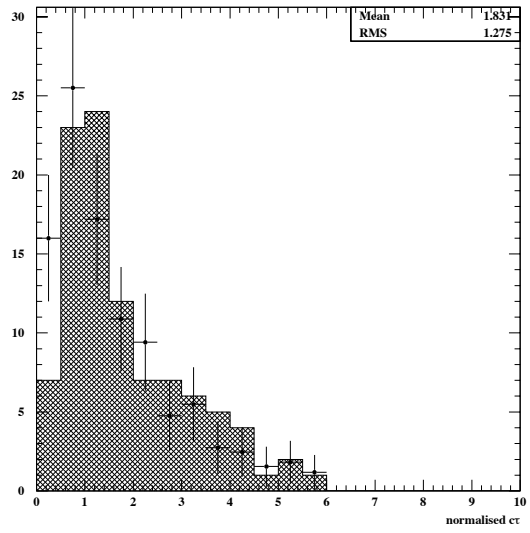


(b) Surviving combinations

Figure 7.12: Distributions of the normalised $c\tau$

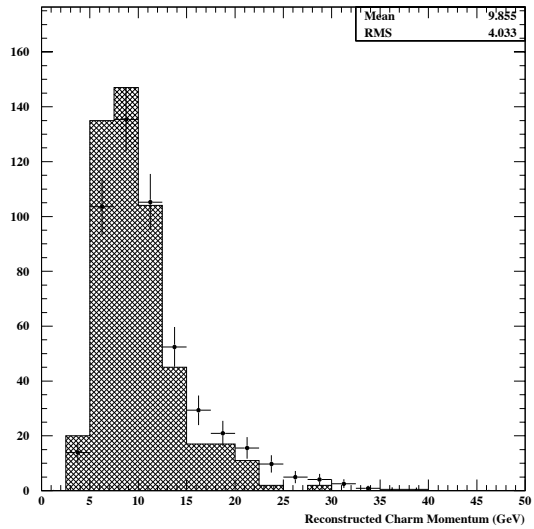


(a) All combinations

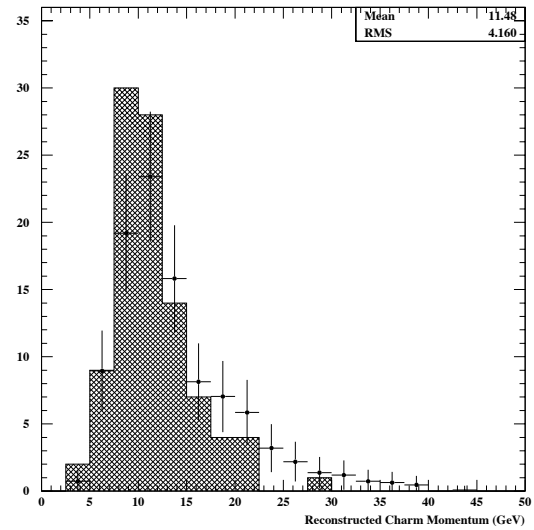


(b) Surviving combinations

Figure 7.13: Distributions of the fitted total momentum (GeV) of the reconstructed D meson

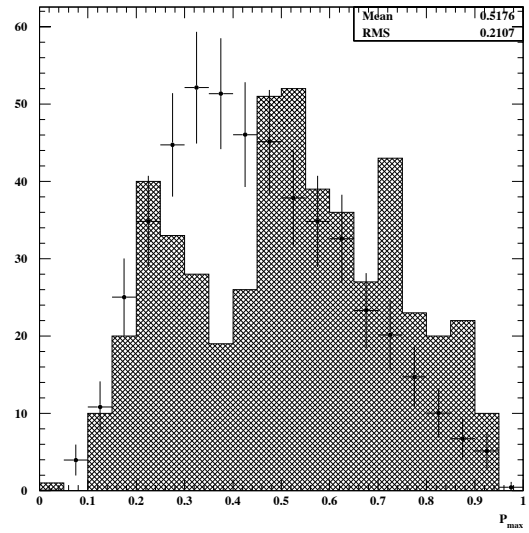


(a) All combinations

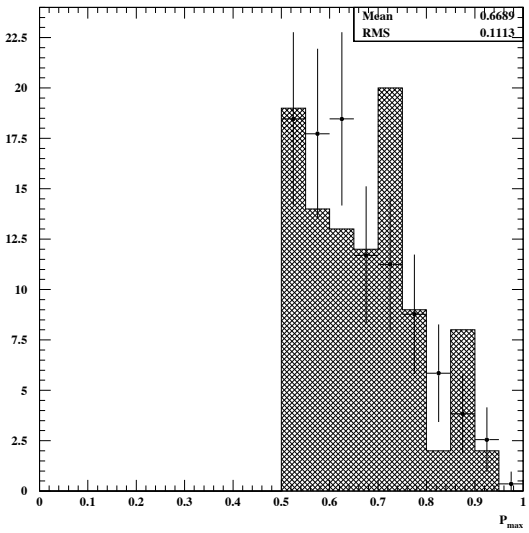


(b) Surviving combinations

Figure 7.14: Distributions of the reconstructed momentum divided by the maximum possible momentum

Combinations with $P_D^*$ less than 200 MeVwere kept.

The distributions of $P_D^*$ are shown in Figure 7.15.

### 7.6.9 Topological Cuts

Two variables $\Theta_{YZ}$ and $\Phi_{YZ}$ are defined in Figure 7.16.

The variable $\Theta_{YZ}$ is the angle in the YZ plane that the line of flight of the D meson makes with the Z axis. This is the same angle used in the constrained fit.

The variable $\Phi_{YZ}$ is the angle between the angle $\Theta_{YZ}$ and the angle formed by the fitted total momentum of the charm decay products in the YZ plane.

Events with an absolute value of $\Theta_{YZ}$ greater than 10° are rejected as are those with an absolute value of $\Phi_{YZ}$ greater than 10°.

The distributions of $\Theta_{YZ}$ are shown in Figure 7.17.

The distributions of $\Phi_{YZ}$ are shown in Figure 7.18.

### 7.6.10 Charge Sum

When a $\nu_\mu$ charged current interaction occurs on a neutron or proton, conservation of charge requires that the total charge of the hadronic jet be either +1 or +2.

This is used in conjunction with the known charge of the D meson under investigation, to test the remaining tracks in the hadronic jet (see Fig. 7.19).

When the primary vertex is fitted without the tracks used for the charm decay vertex, it will contain the reconstructed muon and at least one other charged track. The variable $Q_{sum}$ is defined as the total charge of all the charged tracks in the primary vertex except the muon.

The variable $Q_{sum}$ can thus take a number of values, depending on the type of D meson under investigation. If a $D^0$ is being reconstructed, then $Q_{sum}$ can either be +1 or +2 while if a $D^+$ or $D_S^+$ is being reconstructed then $Q_{sum}$ must be either 0 or +1.

The cuts applied are exactly those described above.

The distributions of $Q_{sum}$ are shown in Figure 7.20.

### 7.6.11 Summary of Cuts

The cuts described in sections 7.6.1- 7.6.10 above are summarised in Table 7.5 which shows the number of combinations passing each cut.

To create this table, a sample of simulated $\nu_\mu$ charged current events, including both charm and non-charm events, were reconstructed and analysed

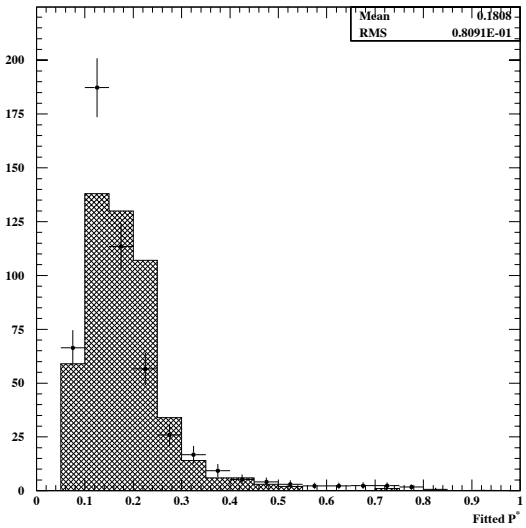


(a) All combinations

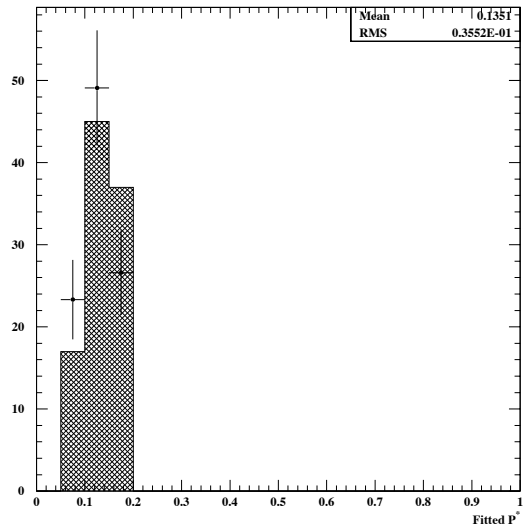


(b) Surviving combinations

Figure 7.15: Distributions of the reconstructed total momentum in the rest frame of the D meson (GeV)

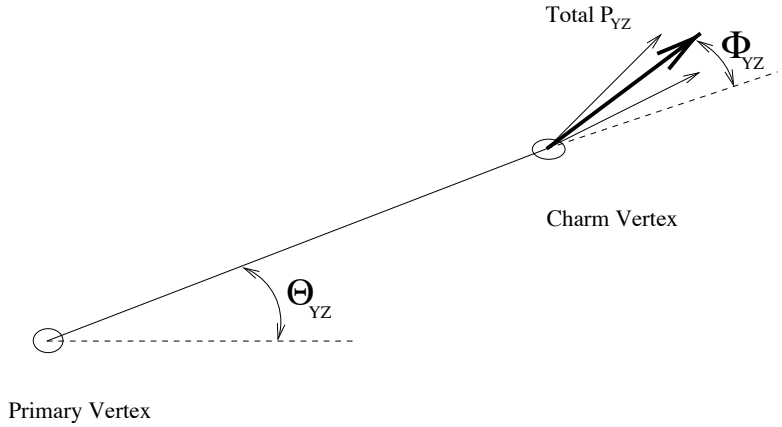


Figure 7.16: Definitions of Angles $\Theta_{YZ}$ and $\Phi_{YZ}$

using the procedure described above. It should be noted that the number of combinations surviving a certain cut does not equate to a number of charm events, but to the total number of combinations over all events that survive the cuts to that stage. Of the combinations surviving the full set of cuts, some will be different interpretations of the same event (for example a $D^+$ or $D_s^+$ decaying into the same mode) and others will be non-charm background. The calculation of the reconstruction efficiency and predicted background rate for each charmed meson will be discussed in section 8.4.

For a given event, if there are one or more combinations that survive all the cuts, then that combination with the best kinematic fit is retained.

Figures A.5- A.8 show a reconstructed Monte Carlo event in which a $D^0$ has been produced and subsequently decayed into a $K^-$ and $\pi^+$.

## 7.7 Reconstruction of $D^{0*}$ and $D^{+*}$

If a $D^0$ or $D^+$ is reconstructed in the event, then a second search is made, for the decay of a $D^*$.

Depending on the D meson that has been reconstructed, combinations of $\pi^\pm$, $\pi^0$ and $\gamma$ are combined with the reconstructed D and the invariant mass is calculated. A test is then made on the invariant mass as well as the invariant mass difference:

$$\Delta^*_{mass} = mass^{D^*}_{rec} - mass^{D}_{rec} \tag{7.24}$$

If the reconstructed invariant mass is within 150 MeVof the known (PDG)

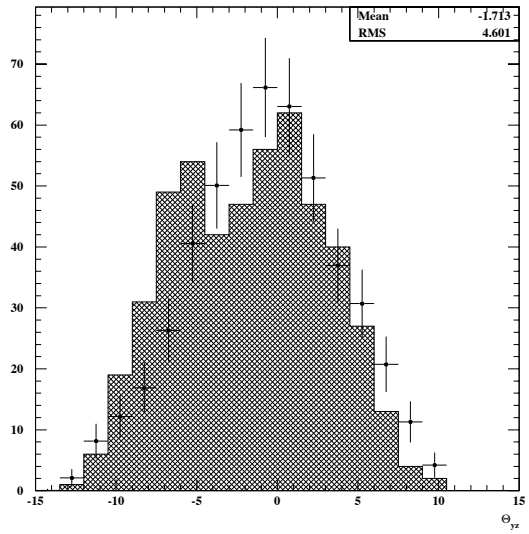


(a) All combinations

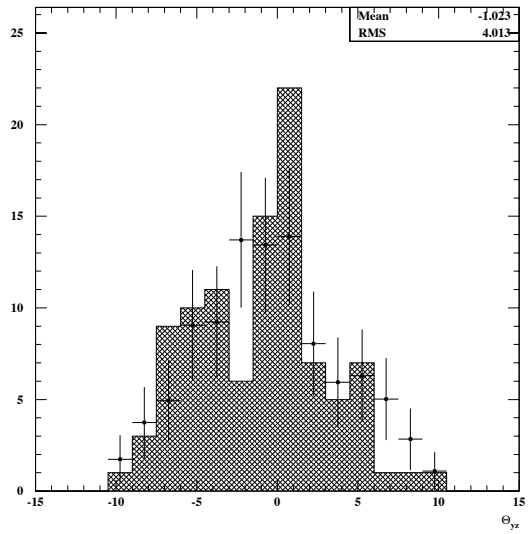


(b) Surviving combinations

Figure 7.17: Distributions of $\Theta_{YZ}$, the angle that the line of flight of the D meson makes with respect to the Z axis (°).

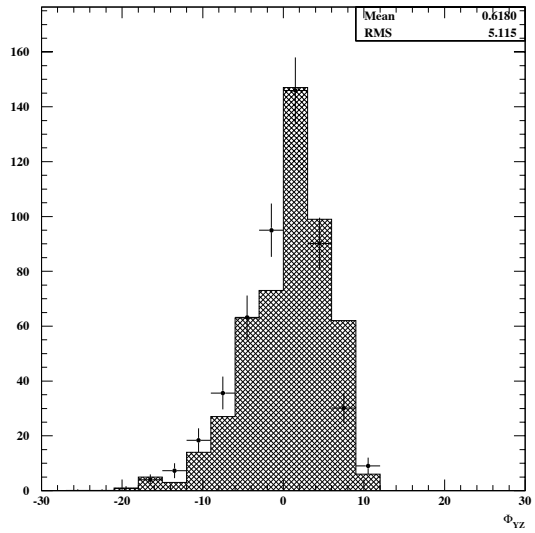


(a) All combinations

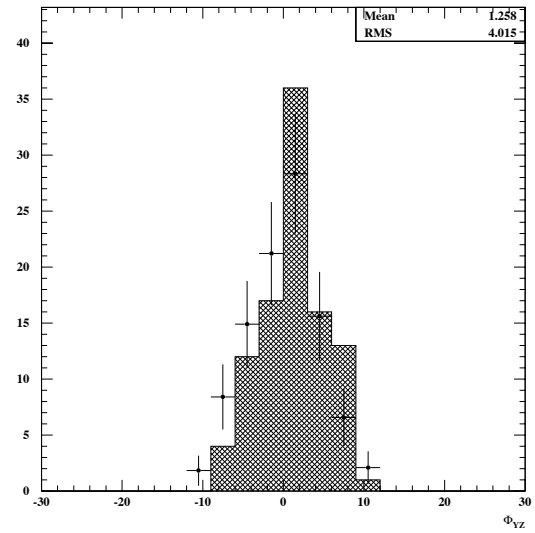


(b) Surviving combinations

Figure 7.18: Distributions of $\Phi_{YZ}$, the angle that the line of flight of the D meson makes with respect to the fitted total momentum of the decay products in the YZ plane (°).

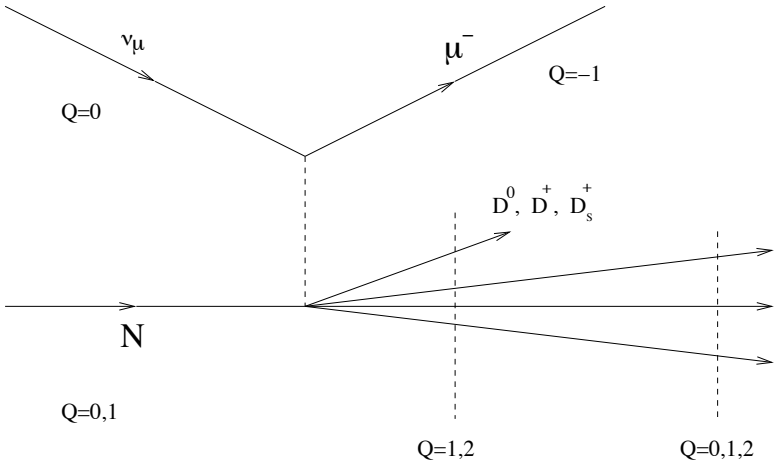


Figure 7.19: Charge assignment in a $\nu_\mu$ charged current interaction used in the definition of $Q_{sum}$.

| Cut | Number of combinations | Efficiency | Relative Efficiency |
|---|---|---|---|
| $\chi^2 < 20$ | 7567 | 100.0% | 100.0% |
| $\sigma_{mass} < 160$ MeV | 6645 | 87.8% | 87.8% |
| $\Delta_{mass} < 150$ MeV | 6370 | 84.2% | 95.9% |
| $\Delta_Z < 4000\ \mu m$ | 5376 | 71.0% | 84.4% |
| $\sigma_Z < 400\ \mu m$ | 5265 | 69.6% | 97.9% |
| $\frac{c\tau_{rec}}{c\tau_{PDG}} < 6$ | 5057 | 66.8% | 96.0% |
| $2 < P_D < 40$ GeV | 5056 | 66.8% | 100.0% |
| $P_{max} > 0.5$ | 1910 | 25.2% | 37.8% |
| $P_D^* < 200$ MeV | 1573 | 20.8% | 82.4% |
| $\Theta_{YZ} < 10^\circ$ | 1528 | 20.2% | 97.1% |
| $\Phi_{YZ} < 10^\circ$ | 1484 | 19.6% | 97.1% |
| $Q_{sum} = \{0, 1, 2\}$ | 1083 | 14.3% | 73.0% |

Table 7.5: Charm event selection and efficiency from $\nu_\mu$ charged current Monte Carlo.

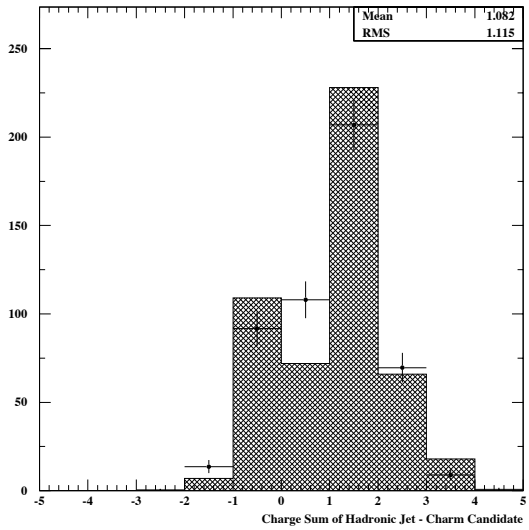


(a) All combinations

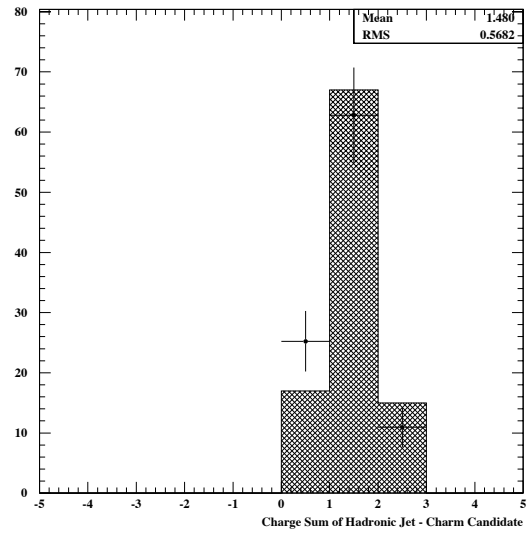


(b) Surviving combinations

Figure 7.20: Distributions of $Q_{sum}$, the total charge of the hadronic jet minus the charge of the D Meson.

value and the mass difference is within 100 MeVof the known value ($\Delta^*_{PDG}$), then the combination is kept.

If more than one combination in the event survive these cuts, that combination with the lowest difference $\Delta^*_{mass} - \Delta^*_{PDG}$ is kept.

## 7.8 Comparison of Monte Carlo and Data

Figure 7.21 shows two scatter plots of the difference between the reconstructed and true charm meson mass versus the separation of the reconstructed vertices in the Z direction divided by the uncertainty in the separation. In the top figure, the small points represent Monte Carlo background events while the larger open circles represent Monte Carlo charm events. The lower figure is the same as the top, except that events passing all the cuts in the data are now superimposed as filled large circles, indicating that the distribution of events reconstructed as charm in the data agrees well with the predicitions of the Monte Carlo.

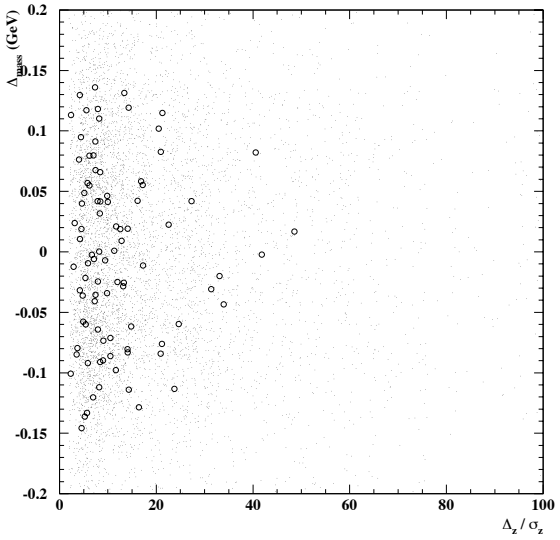


(a) Monte Carlo Signal and Background

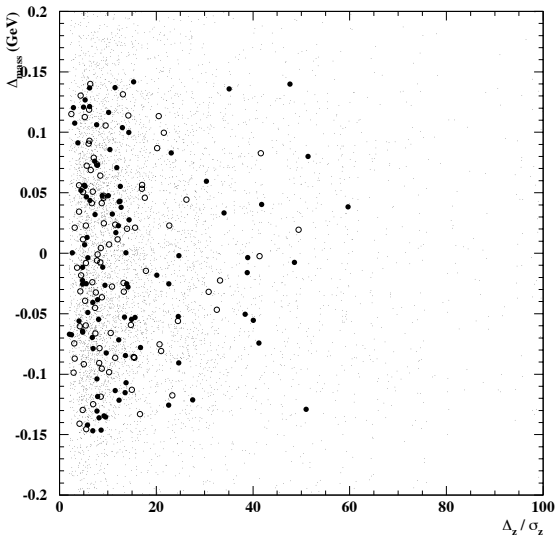


(b) Monte Carlo and Data

Figure 7.21: Scatter plot of the difference between the reconstructed and true charm meson mass (GeV) versus the separation in Z of the reconstructed vertices divided by the uncertainty in that separation

# Chapter 8

# Results

## 8.1 Introduction

The data sample used in this analysis consisted of 11528 filtered STAR events from the 1998 data run and 98279 Monte Carlo events consisting of $\nu_\mu$ CC, $\overline{\nu_\mu}$ CC and $\nu_\mu$ NC.

## 8.2 Filter

During the 1998 data-taking run, approximately 63 million events were recorded during the two neutrino gates. Of these events, 423249 were STAR-NU triggers. Due to the location of STAR close to the coil of the NOMAD magnet and the proximity of the nuclear targets, it is quite possible for a neutrino interaction that does not occur in STAR to produce a STAR-NU trigger. Only 2% of STAR-NU triggers turned out to be actual neutrino interactions inside STAR. As a result, a filter was developed to produce a sub-sample of STAR events for later detailed reconstruction and analysis.

The first stage of the filter was to select only STAR-NU triggers from the raw NOMAD data.

A special version of the reconstruction was developed with looser cuts on track and vertex reconstruction, that sorted the data into 4 categories:

- STAR Vertex Events - Events where a primary vertex was reconstructed in STAR using STAR tracks.
- STAR Track Events - Events which did not pass the STAR Vertex Event criteria but which had at least one reconstructed STAR track.

- DC Vertex Events - Events not passing the two criteria above, but for which the DC reconstruction produces a primary vertex in STAR.
- Other - Events not passing any of the three criteria above.

Table 8.1 shows the number of events assigned to each of the four categories described above.

| Event Category | Number of Events |
|---|---|
| STAR Vertex Events | 11632 |
| STAR Track Events | 29442 |
| DC Vertex Events | 4600 |
| Other | 377575 |
| Total STAR-NU | 423249 |

Table 8.1: Number of events assigned to each category during the filter

It was shown with Monte Carlo that 100% of neutrino interactions in STAR that produce a STAR-NU trigger will be accepted by the first three criteria.

For this analysis, however, it is necessary to reconstruct a good primary vertex using reconstructed STAR tracks and so the data sample used is only those events in the STAR Vertex Event category. In addition, the quality cuts on the vertex reconstruction used for this analysis were tightened with respect to those used for the filtering. This resulted in a total of 11528 events with a properly reconstructed primary vertex.

## 8.3 Reconstruction

The STAR reconstruction described in Chapters 4- 7 was added into the standard NOMAD reconstruction, however the output was a set of ntuples containing information specific to STAR, rather than the usual NOMAD DST.

### 8.3.1 Monte Carlo

Table 8.2 shows the reconstruction efficiencies for $\nu_\mu$ CC Monte Carlo events.

The criteria for accepting an event as having a vertex, is that a vertex is reconstructed from 2 or more STAR tracks, whose position falls in the following volume:

$$-36cm < x < +36cm \tag{8.1}$$
$$-39cm < y < -7cm \tag{8.2}$$
$$+5cm < z < +19cm \tag{8.3}$$

If an event has a vertex satisfying these criteria, a search is performed amongst the tracks in the event for a muon.

If the vertex has at least 3 tracks, and one of those tracks is a muon, then the muon track is removed from the vertex, and the position of the vertex refitted. The muon track can now be extrapolated to the new position of the vertex and the impact parameter calculated (see Figure 1.6).

| | Number of Events | Efficiency | Relative Efficiency |
|---|---|---|---|
| All Events | 62880 | 100.0% | 100.0% |
| Events with a Vertex | 57602 | 91.6% | 91.6% |
| Vertex and a $\mu^-$ | 44678 | 71.1% | 77.6% |
| Impact Parameter | 19114 | 30.4% | 42.8% |

Table 8.2: Reconstruction Efficiencies for $\nu_\mu$ CC Monte Carlo

The equivalent information for neutral current Monte Carlo is shown in Table 8.3.

| | Number of Events | Efficiency | Relative Efficiency |
|---|---|---|---|
| All Events | 15011 | 100.0% | 100.0% |
| Events with a Vertex | 11741 | 78.2% | 78.2% |
| Vertex and a $\mu^-$ | 77 | 0.5% | 0.6% |
| Impact Parameter | 33 | 0.2% | 42.9% |

Table 8.3: Reconstruction Efficiencies for $\nu_\mu$ NC Monte Carlo

For $\overline{\nu_\mu}$ CC events, it is no longer sensible to talk about a leading $\mu^-$, so Table 8.4 shows the efficiency for reconstructing a vertex with a $\mu^+$.

### 8.3.2 Data

During the 1998 data taking period, the neutrino beam was run in several different configurations. Most of the time the horn and reflector were configured to produce a predominantly $\nu_\mu$ beam. A subset of the data was taken

| | Number of Events | Efficiency | Relative Efficiency |
|---|---|---|---|
| All Events | 20388 | 100.0% | 100.0% |
| Events with a Vertex | 16982 | 83.3% | 83.3% |
| Vertex and a $\mu^+$ | 15605 | 76.5% | 91.9% |
| Impact Parameter | 5867 | 28.8% | 37.6% |

Table 8.4: Reconstruction Efficiencies for $\overline{\nu_\mu}$ CC Monte Carlo

with the polarity of these focussing elements reversed, which resulted in a $\overline{\nu_\mu}$ beam.

For this reason, Table 8.5 shows both negative and positive muons, as the reconstruction would look for a $\mu^-$ when the the neutrino beam was producing $\nu_\mu$ and a $\mu^+$ when the beam was $\overline{\nu_\mu}$.

| | Number of Events | Rate |
|---|---|---|
| All Events | 11528 | 100.0% |
| Events with a Vertex | 10846 | 94.0% |
| Vertex and a $\mu^-$ | 5099 | 44.2% |
| Vertex and a $\mu^+$ | 591 | 5.1% |
| Vertex and a $\mu^\pm$ | 5690 | 49.3% |
| Impact Parameter ($\mu^-$) | 1393 | 12.1% |
| Impact Parameter ($\mu^+$) | 152 | 1.3% |
| Impact Parameter ($\mu^\pm$) | 1545 | 13.4% |

Table 8.5: Reconstruction Rates for 1998 Data

## 8.4 Charm Search

For each of the charmed mesons, Monte Carlo was used to determine the reconstruction efficiency and expected background. In order to normalise the Monte Carlo and data samples, the number of events in which an impact parameter is measured was used. As was shown in Table 8.2 and Table 8.3 the vast majority of events with a reconstructed impact parameter will be from charged current interactions.

### 8.4.1 Monte Carlo Signal

In order to determine the efficiency of reconstructing charm, a separate sample of Monte Carlo charm events was produced, using a modified version of NEGLIB that generated events normally, but only wrote the event to disk if a charm quark was produced in the initial interaction. This Monte Carlo charm sample consisted of 7511 events, distributed as shown in table 8.6. The total number of simulated charm events is shown as well as the total number of simulated events in which an impact parameter is reconstructed. The $D^0$ and $D^+$ entries include those events in which a $D^*$ was produced and subsequently decayed into a $D^0$ or $D^+$.

| Charmed Particle | Number of simulated events | Number with Impact Parameter |
|---|---|---|
| $D^0$ | 4574 | 1586 |
| $D^+$ | 2441 | 845 |
| $D_s^+$ | 110 | 38 |
| Other charm | 386 | 133 |
| Total charm | 7511 | 2602 |
| $D^{0*}$ | 3014 | 1044 |
| $D^{+*}$ | 1871 | 648 |

Table 8.6: Numbers of charmed particles in Monte Carlo

Table 8.7 shows the efficiency for reconstructing different charmed mesons as determined from the charm Monte Carlo. It can be seen that the efficiency for reconstructing a $D_s^+$ is significantly higher than that for a $D^0$ or $D^+$. This is primarily due to the greater number of decay modes for the $D_s^+$ which contain only charged decay products as well as kinematics of the decay resulting in lower combinatorial background, resulting in less stringent cuts.

| Charmed Meson | Events Reconstructed | Efficiency |
|---|---|---|
| $D^0$ | 161 | $3.51 \pm 0.27$ % |
| $D^+$ | 86 | $3.52 \pm 0.37$ % |
| $D_s^+$ | 14 | $12.7 \pm 3.2$ % |
| $D^{0*}$ | 23 | $0.76 \pm 0.16$ % |
| $D^{+*}$ | 18 | $0.96 \pm 0.23$ % |

Table 8.7: Efficiency of reconstructing charmed mesons with respect to the total number of charmed mesons produced

### 8.4.2 Monte Carlo Background

The background rate for each charmed particle was determined from Monte Carlo in terms of the number of events with a measured impact parameter, so that the expected background in the data can be easily determined.

A sample of general $\nu_\mu$ charged current Monte Carlo events were used to test each reconstructed D-meson decay mode. For each mode, the rate at which events were incorrectly reconstructed as containing a D-meson decay when there was none, or in which the decay mode or identity of the meson was incorrectly reconstructed was determined.

Table 8.8 shows the background rate from both charged current and neutral current interactions.

| Charmed Meson | Number Reconstructed | Background rate |
|---|---|---|
| $D^0$ | 183 | $0.957 \pm 0.070$ % |
| $D^+$ | 52 | $0.272 \pm 0.038$ % |
| $D_s^+$ | 71 | $0.371 \pm 0.044$ % |
| $D^{0*}$ | 126 | $0.659 \pm 0.059$ % |
| $D^{+*}$ | 25 | $0.131 \pm 0.026$ % |

Table 8.8: Rate of incorrectly reconstructing a background event as a charmed meson as a fraction of the number of events with a reconstructed impact parameter

### 8.4.3 Systematic Uncertainties

In order to measure the effect of systematic uncertainties, each of the cuts described in table 7.5 were individually varied by 10% and the new overall reconstruction efficiencies and background rates were determined for each charmed meson. The total effect was determined by adding each of the contributions in quadrature, resulting in a change of between 0.5% and 1.8%. As the statistical errors in this analysis are much larger (of the order 10% to 25%) the systematic errors are not included in any of the calculations.

### 8.4.4 Data

We are now able to examine the data. By multiplying the scaled background rate in Table 8.8 by the number of reconstructed impact parameter measurements, the estimated number of background events can be determined. Once the number of background events have been subtracted, the reconstruction

efficiency can be used to estimate the number of charm mesons of each type that were produced in the data.

| Charmed Meson | Reconstructed | Estimated Background | Estimated Number |
|---|---|---|---|
| $D^0$ | 24 | $13.33 \pm 0.98$ | $304 \pm 144$ |
| $D^+$ | 10 | $3.79 \pm 0.53$ | $176 \pm 93$ |
| $D_s^+$ | 11 | $5.17 \pm 0.61$ | $46 \pm 26$ |
| $D^{0^*}$ | 11 | $9.18 \pm 0.82$ | $239 \pm 451$ |
| $D^{+^*}$ | 3 | $1.82 \pm 0.36$ | $123 \pm 187$ |

Table 8.9: Reconstructed charmed mesons in $\nu_\mu$ charged current interactions from the 1998 data

In the limited sample of $\overline{\nu_\mu}$ charged current data taken when the neutrino beam was altered to produce predominantly $\overline{\nu_\mu}$, one event was found with a reconstructed charmed meson. This event was reconstructed as $\overline{D^{0^*}} \longrightarrow \overline{D^0}\pi^0$ and is in addition to the 45 events described above. Due to the lack of statistics, an analysis of the production of anti-charm by anti-neutrinos will not be attempted in this thesis.

The reconstructed mass of the $D^0$ mass (see Figure 8.1) is determined to be $1.875 \pm 0.075$ GeVwhich agrees with the world average of $1.8645 \pm 0.0005$ GeV.

The reconstructed $c\tau$ (see Figure 8.2) of $145^{+39}_{-25}\mu m$ is consistent with the world average of $123.7 \pm 0.8\mu m$.

The reconstructed mass of the $D^+$ (see Figure 8.3) is determined to be $1.880 \pm 0.088$ GeV, which agrees with the world average of $1.8693 \pm 0.0005$ GeV.

The reconstructed $c\tau$ (see Figure 8.4) of $213^{+183}_{-67}\mu m$ is consistent with the world average value of $315 \pm 4\mu m$.

The reconstructed mass of the $D_s^+$ (see Figure 8.5) is determined to be $1.973 \pm 0.061$ GeVwhich agrees with the world average of $1.9686 \pm 0.0006$ GeV.

The reconstructed $c\tau$ (see Figure 8.6) of $199^{+132}_{-56}\mu m$ is consistent with the world average value of $148.6^{3.0}_{-2.7}\mu m$.

The reconstructed mass of the $D^{0^*}$ (see Figure 8.7) is determined to be $1.973 \pm 0.046$ GeVwhich agrees with the world average of $2.0067 \pm 0.0005$ GeV.

The reconstructed mass of the $D^{+^*}$ (see Figure 8.8) is determined to be $2.072 \pm 0.031$ GeVwhich is close to the world average of $2.0100 \pm 0.0005$ GeV.

The production rates of charmed mesons at a mean neutrino energy of

33 GeVare shown in Table 8.10. The "Total Charm" rate is determined by the sum of the $D^0$, $D^+$ and $D_s^+$ rates. The rates quoted for the $D^0$ and $D^+$ include those events where the $D^0$ or $D^+$ was reconstructed as the decay of a $D^*$.

| Charmed Meson | Number of Events | Production Rate |
|---|---|---|
| $D^0$ | $304 \pm 144$ | $4.2 \pm 2.0$ % |
| $D^+$ | $176 \pm 93$ | $2.4 \pm 1.3$ % |
| $D_s^+$ | $46 \pm 26$ | $0.64 \pm 0.36$ % |
| $D^{0^*}$ | $239 \pm 451$ | $3.3 \pm 6.2$ % |
| $D^{+^*}$ | $123 \pm 187$ | $1.7 \pm 2.6$ % |
| Total Charm | $526 \pm 174$ | $7.2 \pm 2.4$ % |

Table 8.10: Production rates of charmed mesons as a fraction of $\nu_\mu$ DIS charged current interactions

Even though the individual rates of each of the exclusive channels $D^0$, $D^+$ and $D_s^+$ are not significantly measured (a respective significance of $2.1\sigma$, $1.8\sigma$ and $1.8\sigma$), the total rate of charm produced is measured at the 3 sigma level. This serves to prove the principle that a STAR-like silicon detector can measure charm states within a fixed-target neutrino detector, but with a small efficiency. With additional target mass, additional tracking stations and a 3 dimensional reconstruction (strips in both the x and the y direction) some of the cuts could be tightened to produce higher efficiencies, thereby improving these measurements. The $D^{0^*}$ and $D^{+^*}$ states were not measured above the high background, but with a 3 dimensional detector this background would be further reduced thereby making the measurement possible.

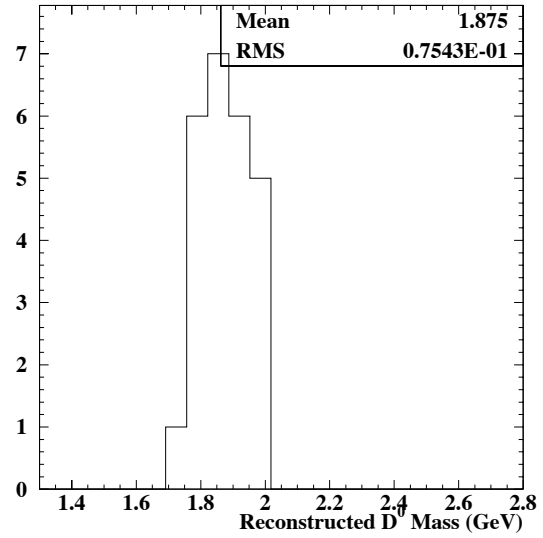


Figure 8.1: Distribution of reconstructed $D^0$ mass (GeV)

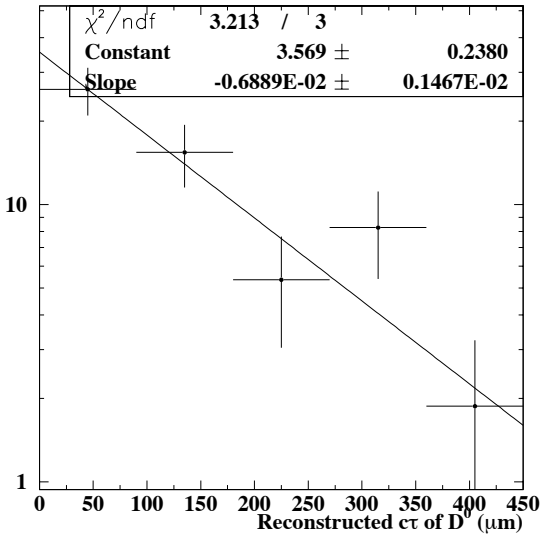


Figure 8.2: Distribution of reconstructed $D^0$ $c\tau$ ($\mu m$)

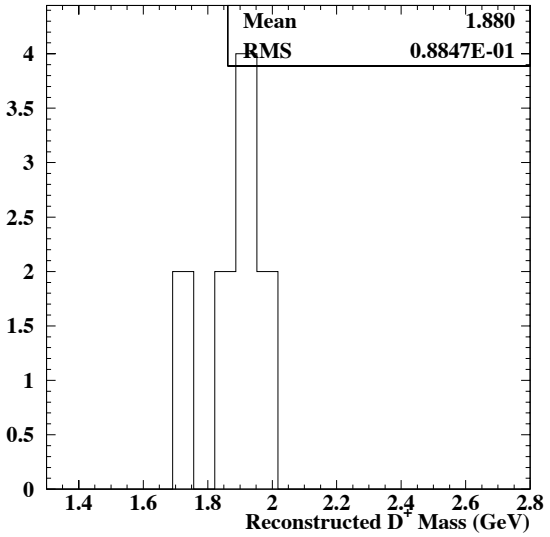


Figure 8.3: Distribution of reconstructed $D^+$ mass (GeV)

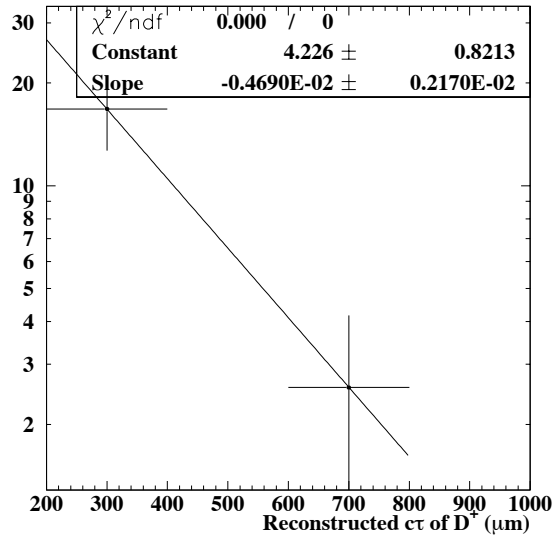


Figure 8.4: Distribution of reconstructed $D^+$ $c\tau$ ($\mu m$)

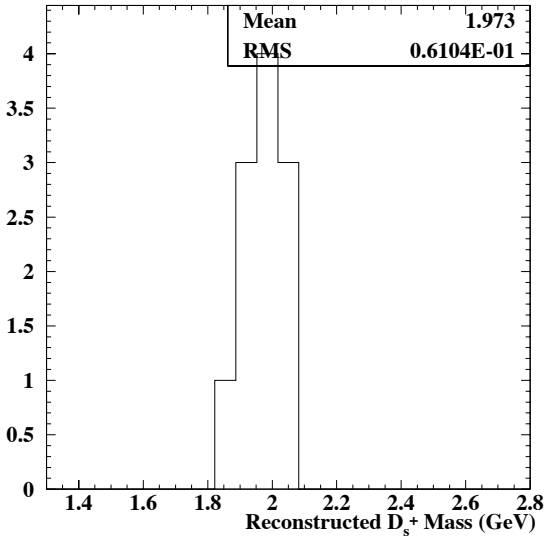


Figure 8.5: Distribution of reconstructed $D_s^+$ mass (GeV)

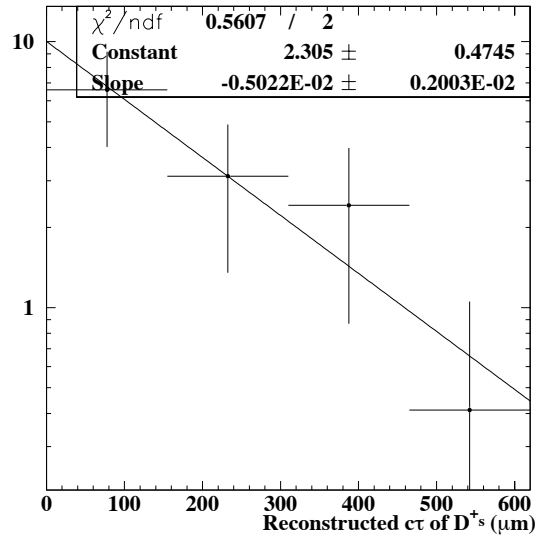


Figure 8.6: Distribution of reconstructed $D_s^+$ $c\tau$ $(\mu m)$

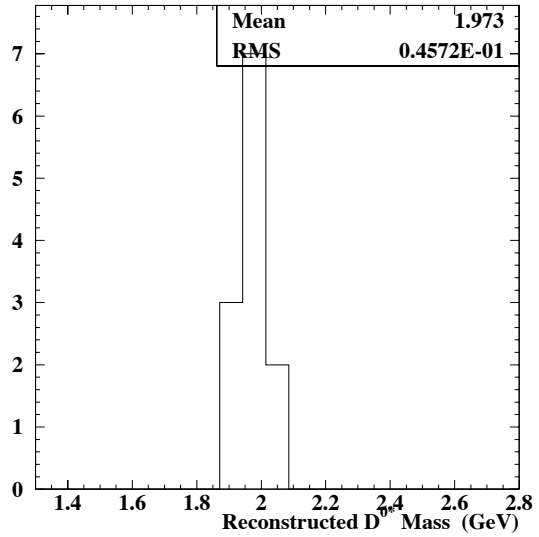


Figure 8.7: Distribution of reconstructed $D^{0*}$ mass (GeV)

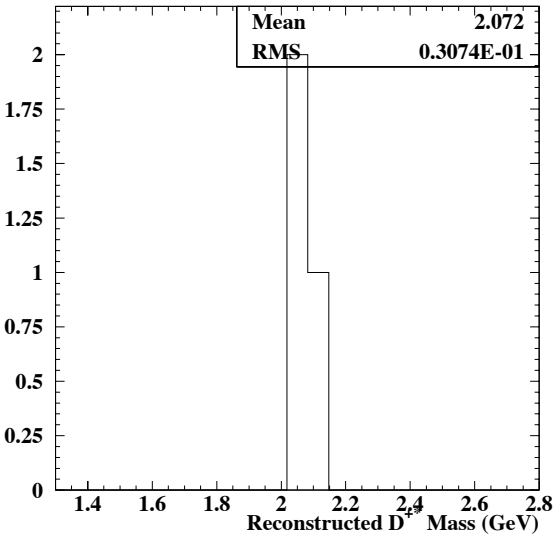


Figure 8.8: Distribution of reconstructed $D^{+*}$ mass (GeV)

### 8.4.5 Comparison with Past Experiments

The most significant experiment to measure the production cross-sections of individual charmed particles by neutrinos was E531 ( [64], [65]). This experiment was able to reconstruct the primary neutrino interaction and the charm decay in a nuclear emulsion.

E531 observed the production and decay of $D^0$, $D^+$, $D_s^+$ and $\Lambda_c^+$ particles.

Table 8.11 shows a comparison between the observed rates of production of charmed mesons in STAR and E531. As NOMAD-STAR did not attempt to make an inclusive measurement of the charm production cross-section, the rates are presented in terms of the production of the $D^0$.

| Charmed Meson | Rate in STAR | Rate in E531 |
|---|---|---|
| $D^0$ | 100% | 100% |
| $D^+$ | $58 \pm 41\%$ | $72 \pm 18\%$ |
| $D_s^+$ | $15 \pm 12\%$ | $11 \pm 7\%$ |

Table 8.11: Comparison between the observed production rates of charmed mesons in STAR and E531.

In [6] and [5], the total charm production cross-section was determined by reconstructing the semi-leptonic decay of charmed particles into a muon, giving a dimuon signature. Although a search for dimuons was not performed in STAR, it is possible to use the known semi-leptonic branching ratios of the charmed particles in [32] and the observed charmed particle production in STAR to estimate the dimuon rate that would be observed at STAR.

This rate was determined to be $0.41 \pm 0.14\%$ at a mean energy of 33GeV.

Figure 8.9 has been taken from [6] and a point corresponding to the STAR measurement has been added.

It can be seen that, within the relatively large statistical uncertainties, the measured production rate of charmed mesons within STAR agrees well with the previous experiments.

### 8.4.6 Future Possibilities

An exciting opportunity for a STAR-like detector would exist at a neutrino factory. A neutrino factory is a proposed facility in which a very high number of muons (approximately $10^{20}$ per year) are created, accelerated and then allowed to decay in storage rings, producing two intense beams of neutrinos. In [66] an estimate is made for the flux of neutrinos at a near detector, placed 30 metres down-stream from one of the two 150 metre long straight sections

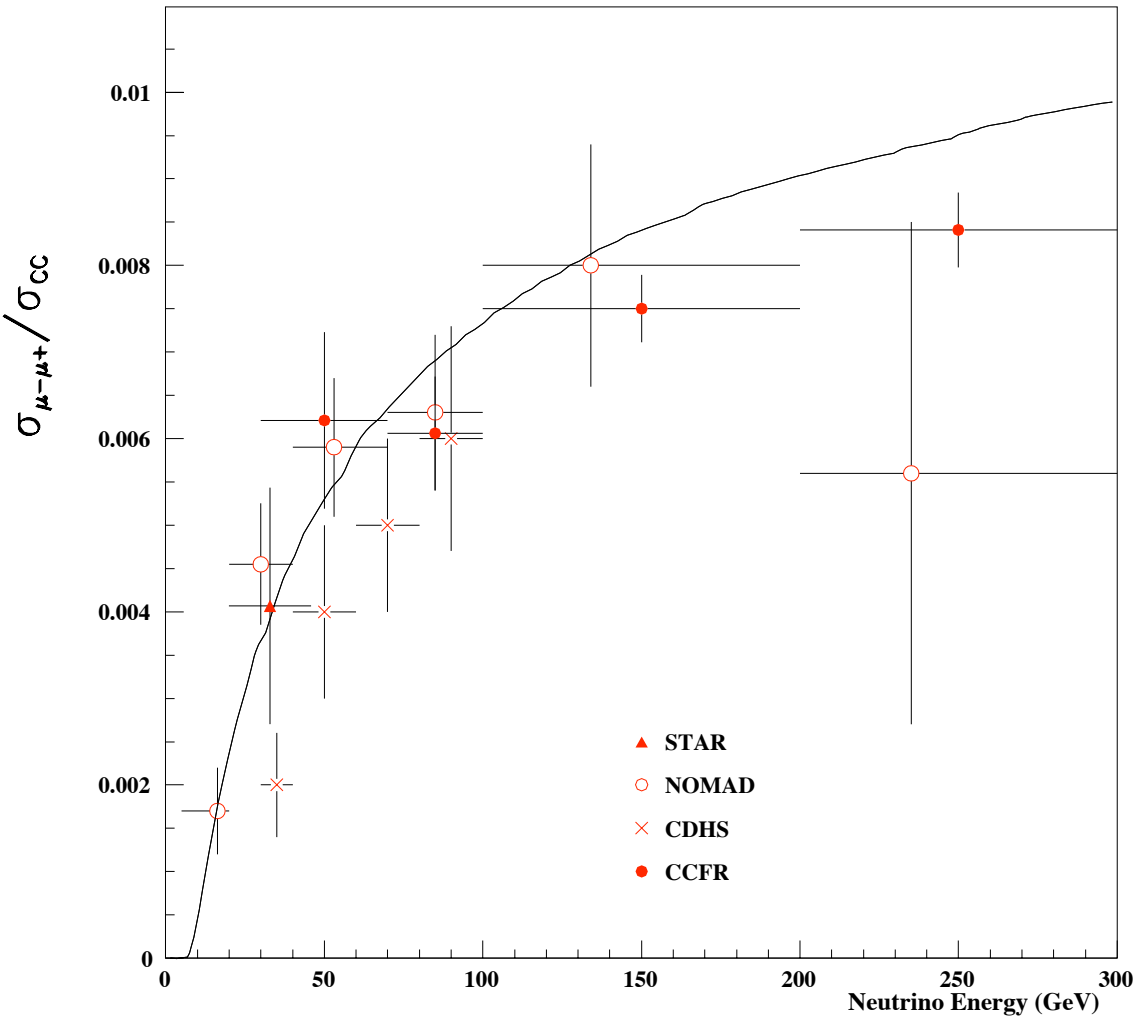


Figure 8.9: Neutrino-induced opposite sign dimuon rates corrected for acceptance and kinematic effects assuming a charm mass of 1.3 (GeV/$c^2$). This figure has been taken from [6] and a point added to represent the STAR data

.

of a 50 GeVmuon storage ring (see Figure 8.10). From this estimate, and using the measured efficiency of STAR, it can be determined that if the STAR detector was part of a near detector at a neutrino factory, it would record 200 million events per year, and would thus reconstruct approximately one million charm events per year!

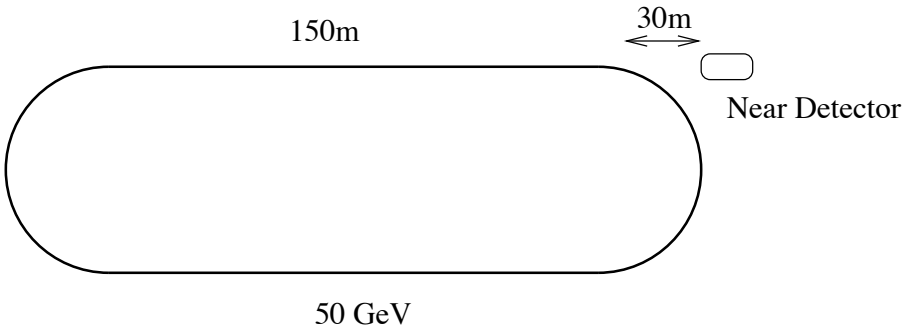


Figure 8.10: Schematic view of the muon storage ring and a near detector at a neutrino factory.

With such a high number of reconstructed charm events, the production cross-sections could be measured to high accuracy. In addition, the CKM parameter $V_{cd}$, currently known with a precision of approximately 5%, could be measured by comparing the rates of production of charm and anti-charm by neutrinos and anti-neutrinos. Lastly, a neutrino factory beam could be used to search for $D^0 - \overline{D^0}$ mixing, and CP violations in charm mesons as the beam produced at a neutrino factory consists of either $\nu_\mu$ and $\overline{\nu_e}$ or $\overline{\nu_\mu}$ and $\nu_e$. A charged current interaction, producing charm or anti-charm, can be labelled by the sign of the lepton produced at the primary vertex, and so the initial charmed particle can be tagged from the primary interaction, while a search is made for the decay of both $D^0$ and $\overline{D^0}$.

# Conclusion

This project aimed to reconstruct charmed mesons produced in the charged current interaction of neutrinos and thus to measure the capabilities of a NAUSICAA-like detector in order to demonstrate the ability of such a detector to measure $\nu_\mu(\nu_e) \leftrightarrow \nu_\tau$ oscillations.

The impact parameter resolution of the STAR detector was found to be $28\mu m$, agreeing well with Monte Carlo and indicating that STAR could be used to reconstruct the decay of a tau into a muon through the use of an impact parameter cut.

A search was performed for the production by neutrinos of $D^0$, $D^+$, $D_s^+$, $D^{0^*}$ and $D^{+^*}$ mesons. The search utilised both the tracking and high resolution vertexing capabilities of the silicon detector and the precision momentum measurement capabilities of the drift chambers. This search resulted in the reconstruction of 45 charm events, of which 22 were estimated to be background. The inclusive rate of production of charm in deep inelastic charged current $\nu_\mu$ interactions was determined to be $7.2 \pm 2.4$ %. The total production rate and relative fractions of charmed mesons produced were found to agree with previous experiments.

The measured impact parameter resolution and ability of STAR to reconstruct charm decays indicates that it would be possible to use a similar detector to reconstruct the decay of a $\tau^\pm$ and therefore could be used in an appearance search for $\nu_\mu(\nu_e) \leftrightarrow \nu_\tau$ oscillations.

It should be noted that as the STAR detector was only able to make precision measurements in the Y axis, the constrained fit and vertex separation were not able to separate signal from background as strongly as a full 3D tracker. In addition to performing an oscillation search, such a tracker would also be able to provide a significant contribution to the understanding of the production of charm by neutrinos.

Finally, it has been determined that even without modification, the STAR design would be able to make a significant contribution to neutrino, charm and CP physics at a future neutrino factory facility.

# Appendix A

# Images from the STAR version of matchgraph

The following figures are images taken from the NOMAD event display program (matchgraph) as modified to include the reconstruction of the STAR detector.

In the views showing the whole of NOMAD and the Drift Chambers, particles may be identified by the line style and colour. Muons are indicated by a solid green line, pions by a solid red line, and other tracks without definite particle identification by a solid blue line. Dashed lines indicate photons reconstructed from clusters in the calorimeter and are assumed to come from the primary vertex.

In the close-up views of STAR, a dark blue line indicates a track in the primary vertex, a green track indicates a track in the charm decay vertex and a light blue track indicates a track that has not been assigned to either vertex. Hits in the silicon are represented by a large cross, with the charge deposited in each strip represented by filled blu histograms.

The silicon vertices are surrounded by an ellipse, which is the ellipse of error determined from the kalman vertex fit. In addition, the primary vertex has a distance scale, the longer marks are spaced 100 $\mu m$ apart, to give an inidcation of scale.

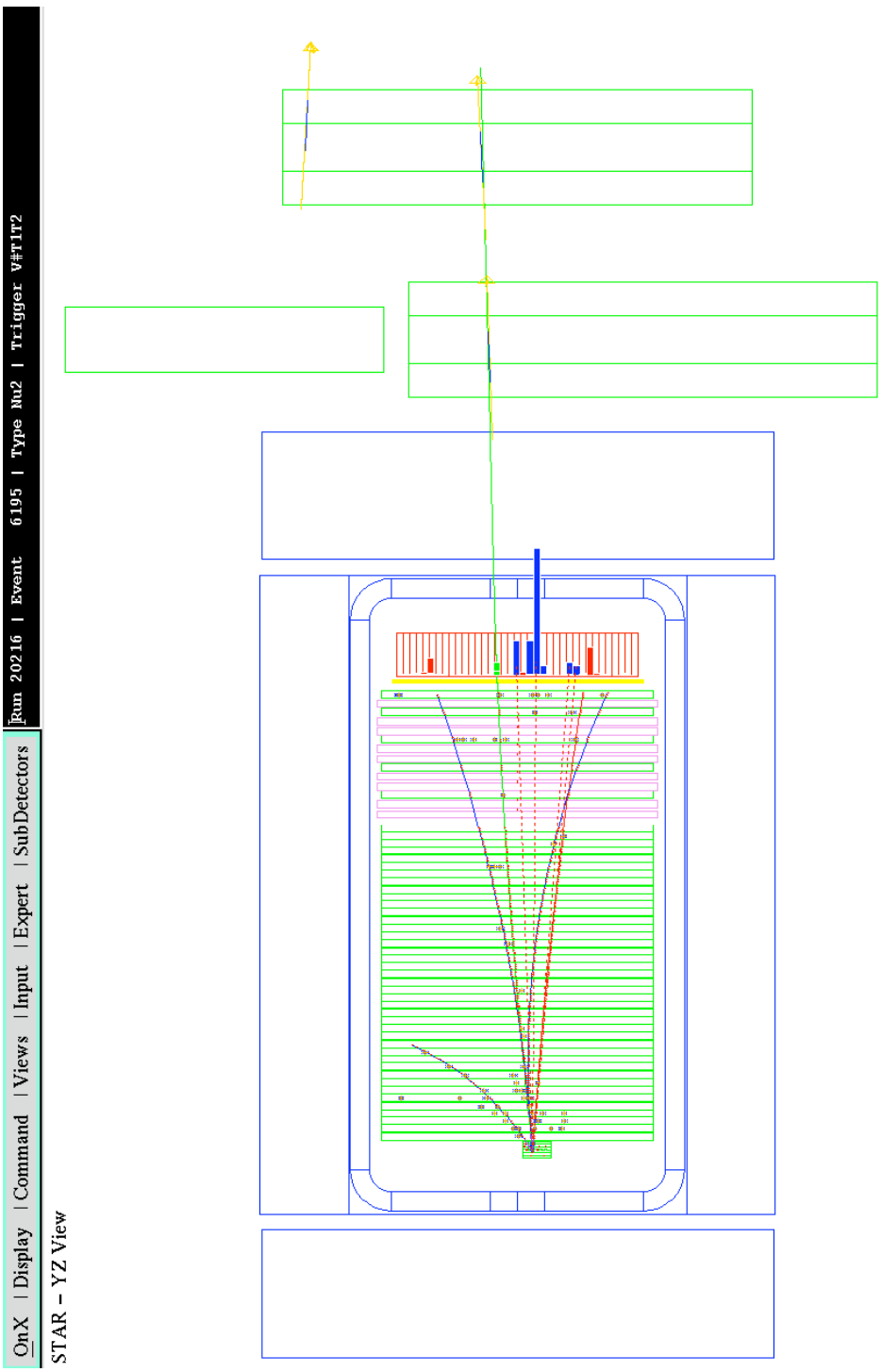


Figure A.1: View of a typical $\nu_\mu$ charged current interaction showing the full NOMAD experiment.

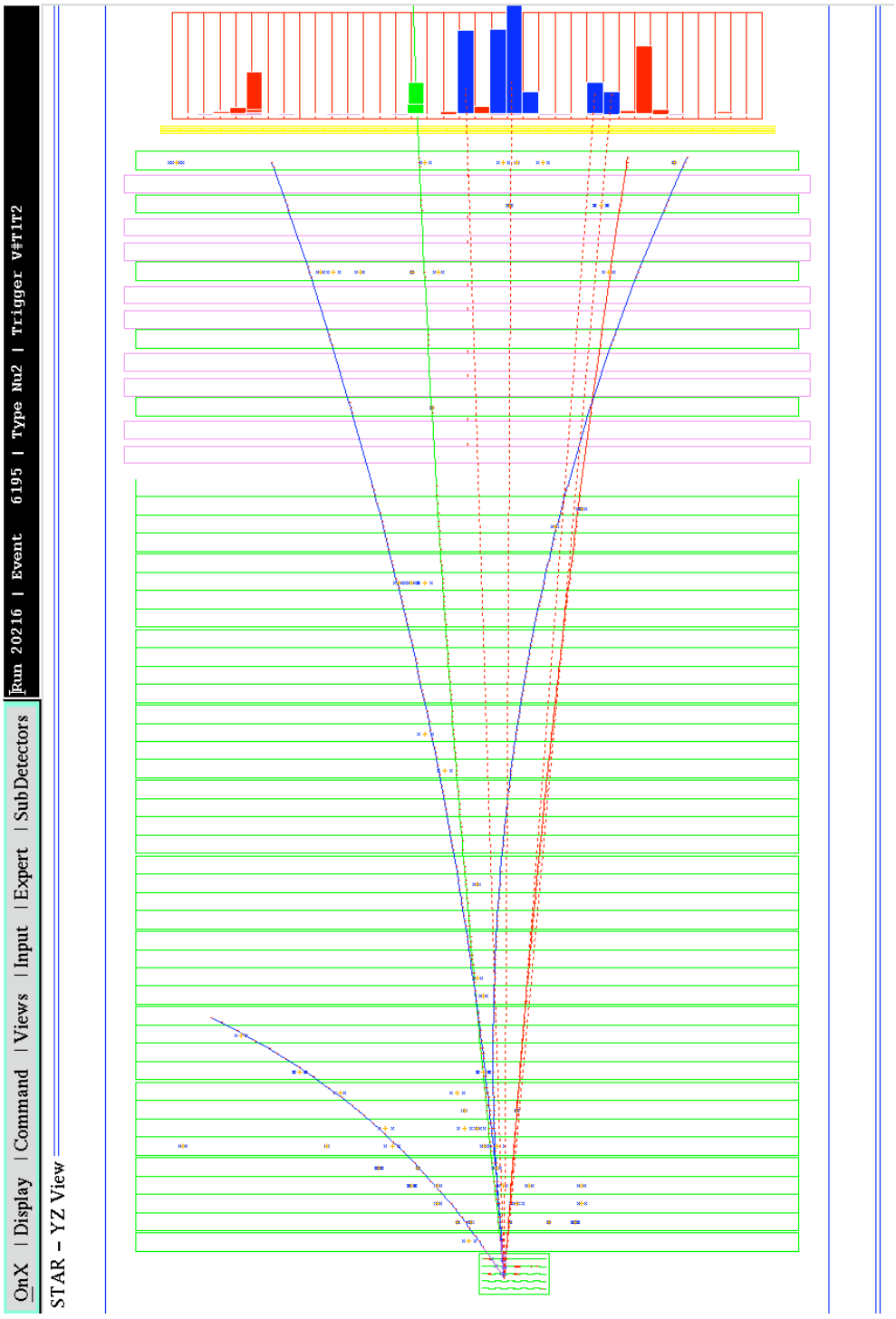


Figure A.2: View of a typical $\nu_\mu$ charged current interaction showing the full STAR detector and a section of the drift chambers.

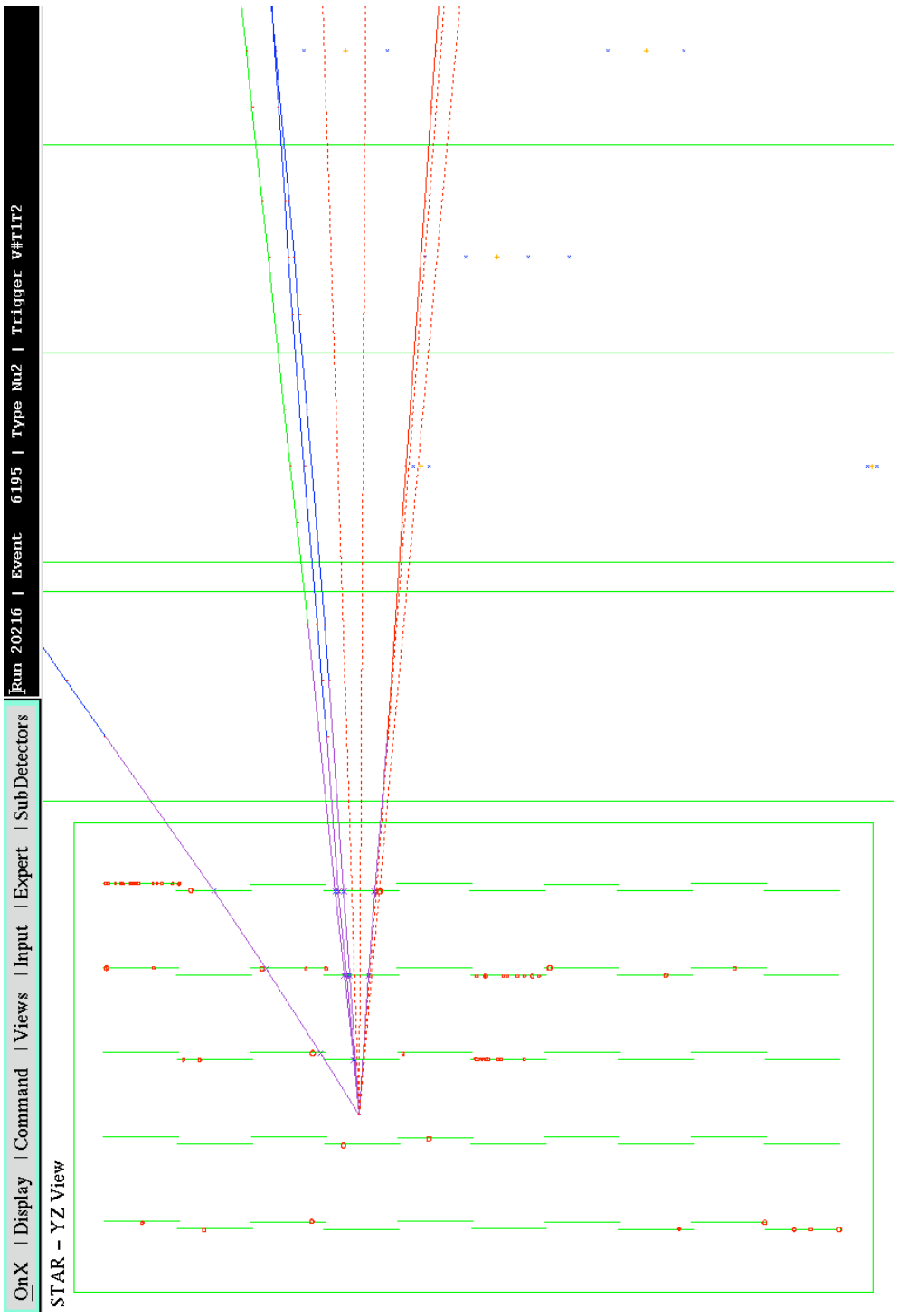


Figure A.3: View of a typical $\nu_\mu$ charged current interaction showing the reconstructed SiTracks and STAR primary vertex.

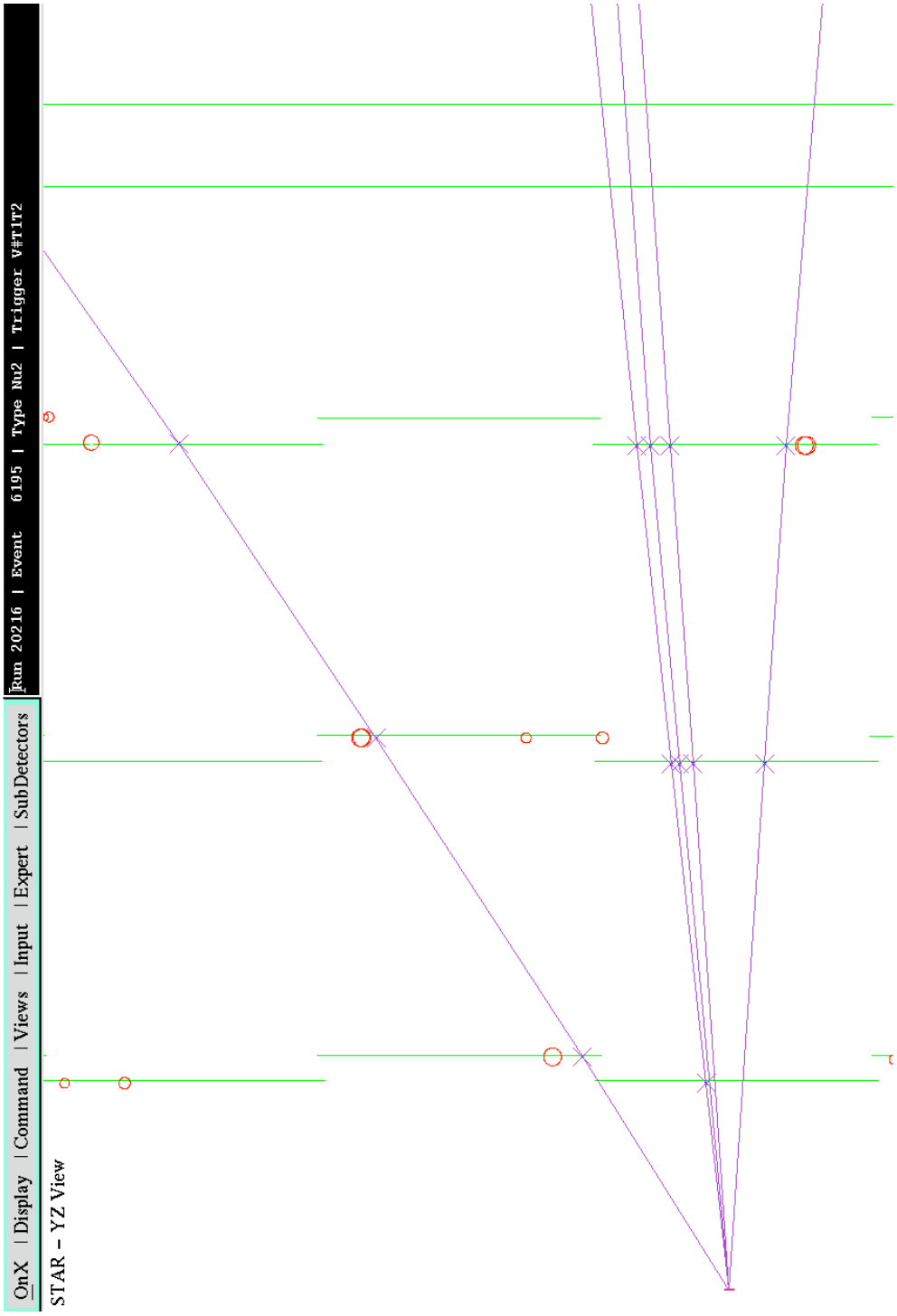


Figure A.4: Close-up view of a typical $\nu_\mu$ charged current interaction.

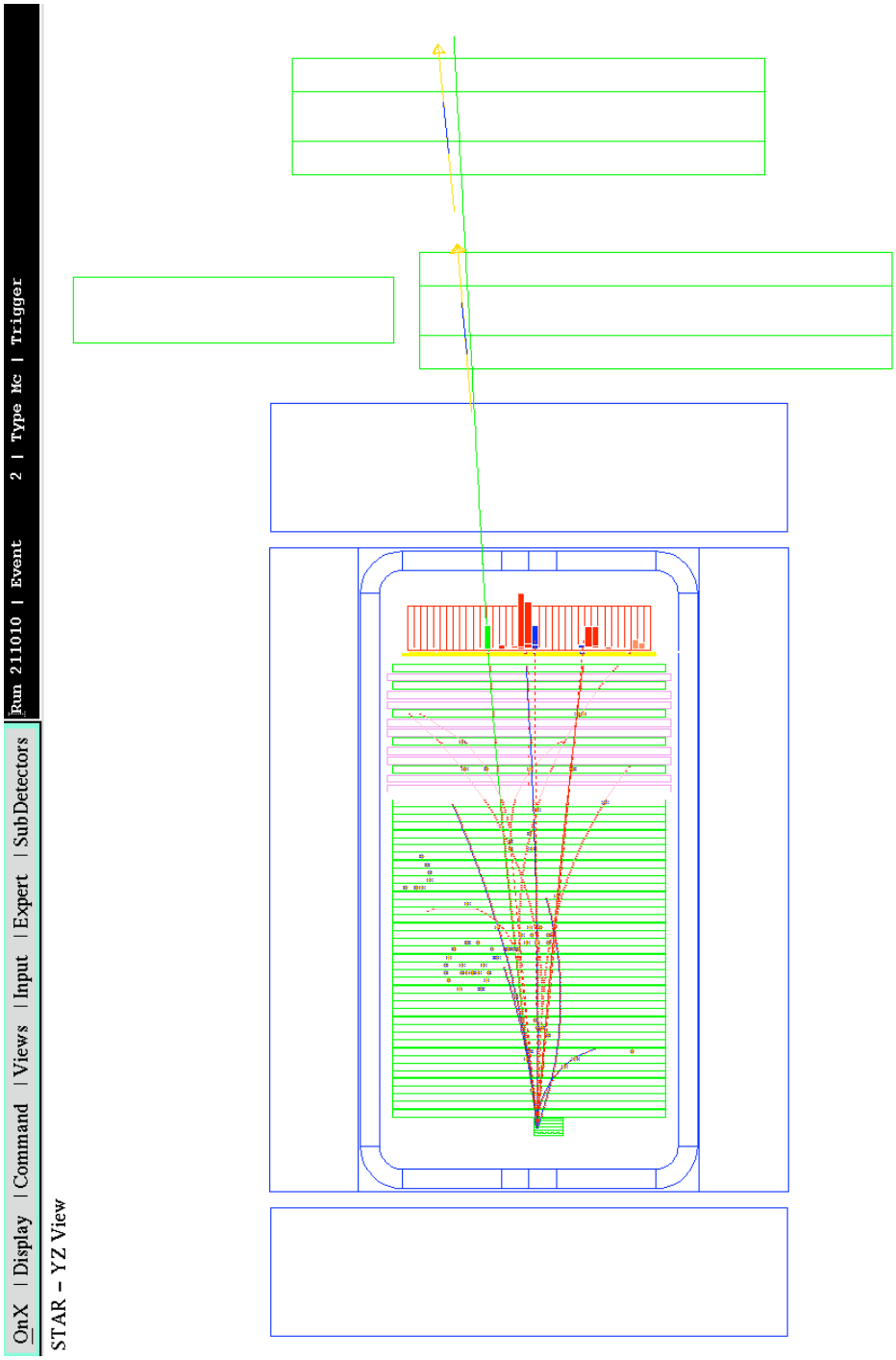


Figure A.5: View of a reconstructed Monte Carlo charm decay showing the full NOMAD experiment.

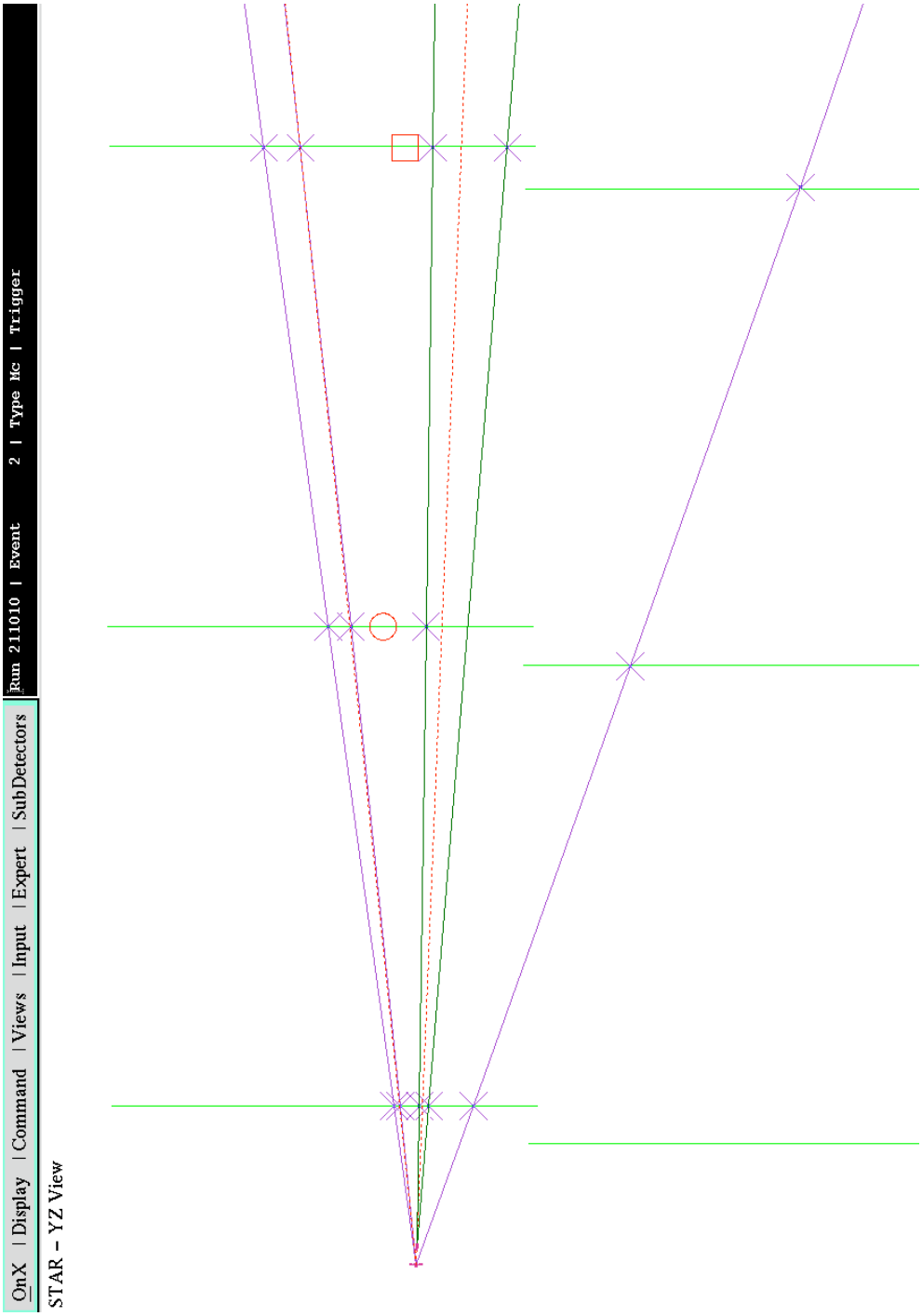


Figure A.6: View of a reconstructed Monte Carlo charm decay showing the full STAR detector.

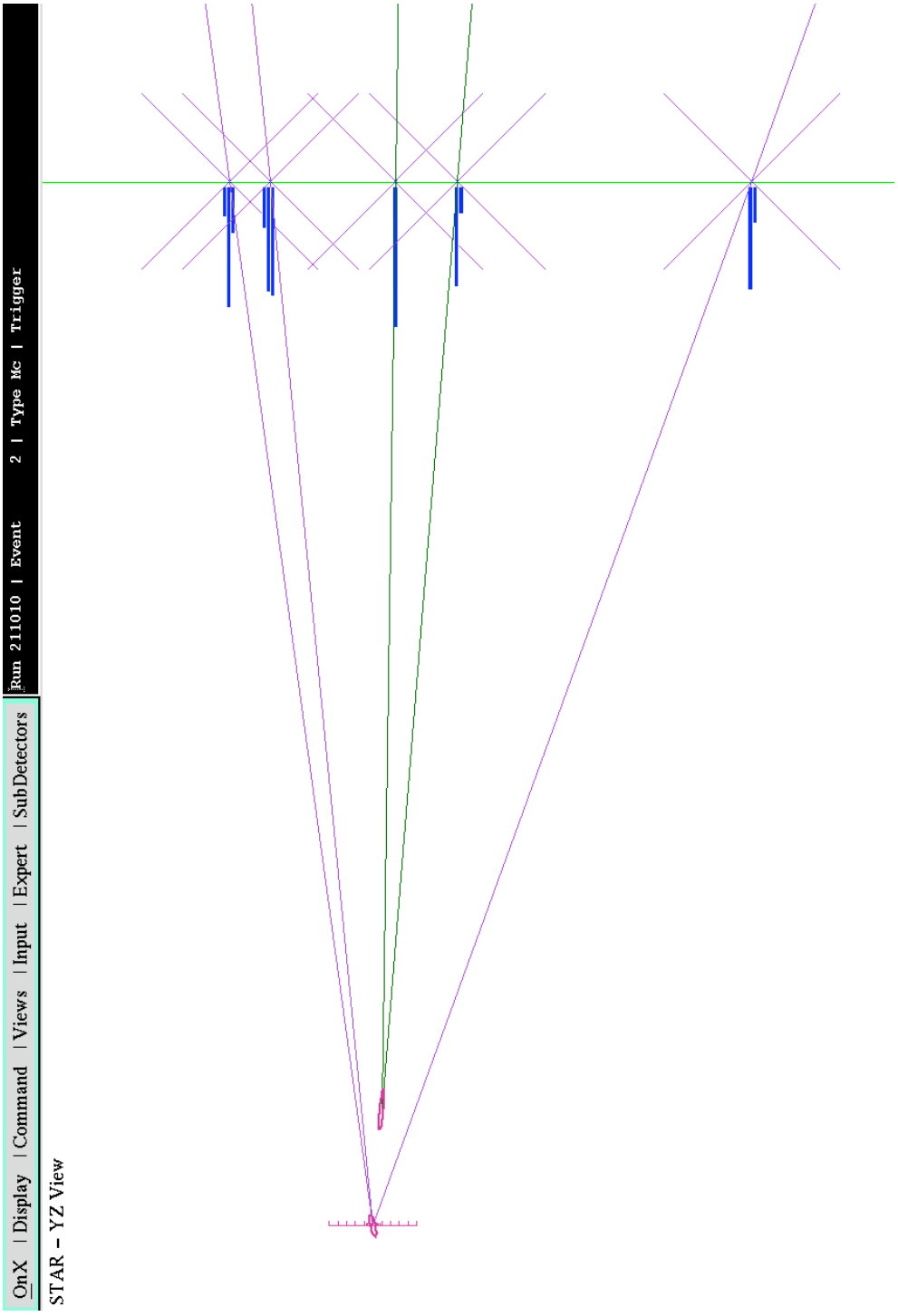


Figure A.7: View of a reconstructed Monte Carlo charm decay showing the reconstructed primary and secondary vertices.

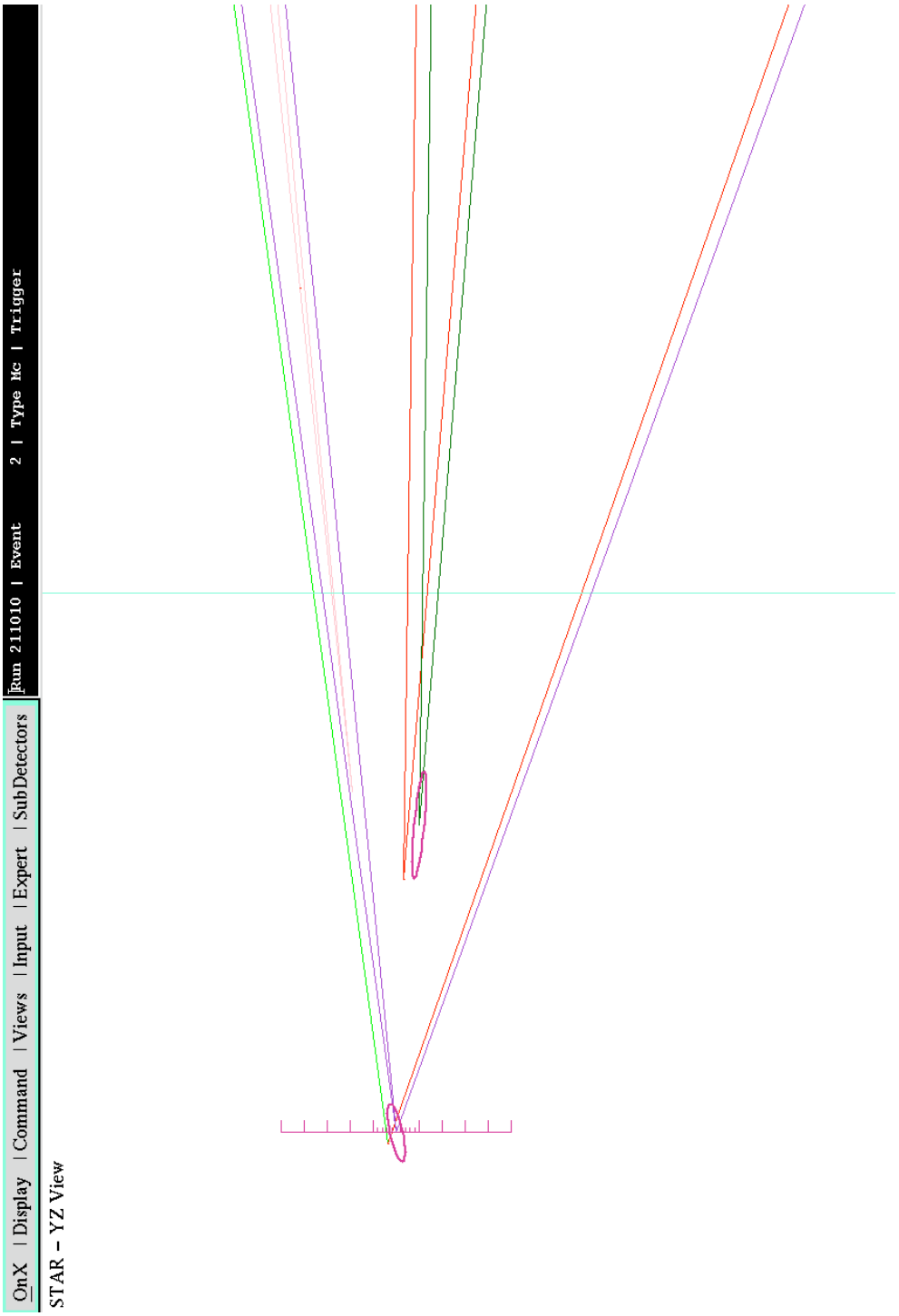


Figure A.8: View of a reconstructed Monte Carlo charm decay showing the reconstructed primary and secondary vertices overlayed with the Monte Carlo vertices.

# Appendix B

# Cuts used in the reconstruction of silicon hits

| Plane | Ladder | Seed Cut | Neighbour Cut | Cluster Cut |
|---|---|---|---|---|
| 1 | 1 | 4.1 | 0.5 | 4.8 |
| 1 | 2 | 4.1 | 0.5 | 5.0 |
| 1 | 3 | 4.0 | 0.5 | 4.3 |
| 1 | 4 | 4.1 | 0.5 | 4.8 |
| 1 | 5 | 4.0 | 0.5 | 4.8 |
| 1 | 6 | 3.5 | 0.5 | 4.4 |
| 1 | 7 | 3.8 | 0.5 | 4.1 |
| 1 | 8 | 3.6 | 0.5 | 4.5 |
| 1 | 9 | 3.9 | 0.5 | 5.0 |
| 1 | 10 | 4.0 | 0.5 | 5.0 |

Table B.1: Signal/Noise cuts used to reconstruct hits in Plane 1

| Plane | Ladder | Seed Cut | Neighbour Cut | Cluster Cut |
|---|---|---|---|---|
| 2 | 1 | 3.9 | 0.5 | 4.8 |
| 2 | 2 | 4.0 | 0.5 | 4.9 |
| 2 | 3 | 4.0 | 0.5 | 4.8 |
| 2 | 4 | 3.8 | 0.5 | 5.1 |
| 2 | 5 | 4.4 | 0.5 | 3.8 |
| 2 | 6 | 4.3 | 0.5 | 6.1 |
| 2 | 7 | 4.3 | 0.5 | 5.3 |
| 2 | 8 | 3.9 | 0.5 | 4.6 |
| 2 | 9 | 4.2 | 0.5 | 4.6 |
| 2 | 10 | 3.9 | 0.5 | 4.3 |

Table B.2: Signal/Noise cuts used to reconstruct hits in Plane 2

| Plane | Ladder | Seed Cut | Neighbour Cut | Cluster Cut |
|---|---|---|---|---|
| 3 | 1 | 4.4 | 0.5 | 5.4 |
| 3 | 2 | 3.7 | 0.5 | 4.9 |
| 3 | 3 | 3.7 | 0.5 | 4.4 |
| 3 | 4 | 3.8 | 0.5 | 4.5 |
| 3 | 5 | 3.8 | 0.5 | 4.4 |
| 3 | 6 | 3.5 | 0.5 | 4.0 |
| 3 | 7 | 3.7 | 0.5 | 4.3 |
| 3 | 8 | 3.9 | 0.5 | 4.9 |
| 3 | 9 | 3.9 | 0.5 | 4.6 |
| 3 | 10 | 3.9 | 0.5 | 5.0 |

Table B.3: Signal/Noise cuts used to reconstruct hits in Plane 3

| Plane | Ladder | Seed Cut | Neighbour Cut | Cluster Cut |
|---|---|---|---|---|
| 4 | 1 | 3.9 | 0.5 | 4.8 |
| 4 | 2 | 3.9 | 0.5 | 4.7 |
| 4 | 3 | 4.0 | 0.5 | 5.0 |
| 4 | 4 | 3.7 | 0.5 | 4.5 |
| 4 | 5 | 3.5 | 0.5 | 4.7 |
| 4 | 6 | 3.8 | 0.5 | 4.6 |
| 4 | 7 | 3.9 | 0.5 | 5.2 |
| 4 | 8 | 3.9 | 0.5 | 4.6 |
| 4 | 9 | 3.8 | 0.5 | 4.6 |
| 4 | 10 | 4.1 | 0.5 | 5.6 |

Table B.4: Signal/Noise cuts used to reconstruct hits in Plane 4

| Plane | Ladder | Seed Cut | Neighbour Cut | Cluster Cut |
|---|---|---|---|---|
| 5 | 1 | 4.3 | 0.5 | 5.0 |
| 5 | 2 | 3.8 | 0.5 | 4.6 |
| 5 | 3 | 3.9 | 0.5 | 4.6 |
| 5 | 4 | 3.9 | 0.5 | 5.2 |
| 5 | 5 | 3.4 | 0.5 | 4.8 |
| 5 | 6 | 3.7 | 0.5 | 4.6 |
| 5 | 7 | 4.0 | 0.5 | 4.8 |
| 5 | 8 | 4.4 | 0.5 | 5.2 |
| 5 | 9 | 4.2 | 0.5 | 5.1 |
| 5 | 10 | 3.4 | 0.5 | 3.8 |

Table B.5: Signal/Noise cuts used to reconstruct hits in Plane 5

# Bibliography


[1] G. Barichello et al. Performance of long modules of silicon microstrip detectors. *Nucl. Instr. and Meth. in Phys. Res. A*, 413:17–30, 1998.

[2] J. Altegoer et al. A search for $\nu_\mu \to \nu_\tau$ oscillations using the NOMAD detector. *Physics Letters B*, 431:219–236, 1998b.

[3] P. Astier et al. A more sensitive search for $\nu_\mu \to \nu_\tau$ oscillations in NOMAD. *Physics Letters B*, 453:169, 1999.

[4] P. Astier et al. Limit on $\nu_e \rightsquigarrow \nu_\tau$ oscillations from the NOMAD experiment. *Physics Letters B*, 471:406–410, 2000.

[5] S.B. Boyd. *Neutrino production of opposite sign dimuons in the NOMAD experiment.* PhD thesis, University of Sydney, sep 1998.

[6] P.Astier *et* al., NOMAD Collaboration, *Physics Letters B 486* 2000.

[7] E.Eskut *et* al., CHORUS Collaboration, Nucl. Instr. and Meth. A401 (1997), 352; E.Eskut *et* al., CHORUS Collaboration, Phys. Lett. B434 (1998) 205.

[8] J. Altegoer *et al.*, The NOMAD Collaboration, Nucl. Instr. and Meth. A404 (1998) 96; P. Astier *et al.*, The NOMAD Collaboration, Physics Letters B453 (1999) 169.

[9] J.J. Gómez-Cadenas, J.A. Hernando and A. Bueno, Nucl. Instr. and Meth. A378 (1996) 196-220.

[10] J.J. Gómez-Cadenas and J.A. Hernando, Nucl. Instr. and Meth. A381 (1996) 223-235.

[11] A.S. Ayan et al., CERN-SPSC/97-5,SPSC/I213, March, 1997.

[12] O. Toker, S. Masciocchi, E. Nygård, A. Rudge, P. Weilhammer, Nucl. Instr. and Meth. A340 (1994) 572.

[13] P.P. Allport *et al.*, Nucl. Instr. and Meth. A310 (1991) 155.

[14] G. Baricchello *et al.*, Nucl. Instr. and Meth. A419 (1998) 1.

[15] R.E. Kalman, J. Basic Eng. 82 (1960) 35; R.E. Kalman and R.S. Bucy, J. Basic Eng. 83 (1961) 95.

[16] R. Frühwirth, Nucl. Instr. and Meth. A262 (1987) 444.

[17] P. Billoir, Nucl. Instr. and Meth. 225 (1984) 352.

[18] P. Billoir, R. Frühwirth and M. Regler, Nucl. Instr. and Meth. A241 (1985) 115.

[19] L. Stanco, Computer Physics Communications 57 (1989) 380.

[20] P. Billoir and S. Qian, Nucl. Instr. and Meth. A294 (1990) 219; P. Billoir and S. Qian, Nucl. Instr. and Meth. A295 (1990) 492.

[21] P. Billoir and S. Qian, Nucl. Instr. and Meth. A311 (1992) 139.

[22] E. Calligarich, R. Dolfini, M. Genoni and A. Rotondi, Nucl. Instr. and Meth. A311 (1992) 151.

[23] V. Innocente and E. Nagy, Nucl. Instr. and Meth. A324 (1993) 297.

[24] E.J. Wolin and L.L. Ho, Nucl. Instr. and Meth. A329 (1993) 493.

[25] R. Luchsinger and C. Grab, Computer Physics Communications 76 (1993) 263.

[26] P. Astier *et al.*, Nucl. Instr. and Meth. A450 (2000) 138.

[27] V.E. Kuznetsov, Nucl. Phys. B (Proc. suppl.) 78 (1999) 287.

[28] G.Z. Molière, Z. Naturforsch. 2a (1947) 133; Z. Naturforsch. 3a (1948), 78.

[29] H.A. Bethe, Phys. Rev. 89 (1953), 1256.

[30] G.R. Lynch and O.I. Dahl, Nucl. Instr. and Meth. B58 (1991) 6.

[31] GEANT, CERN Program Library Long Writeup W5013, (1994), 234.

[32] Particle Data Group, Eur. Phys. J. C (2000) 163.

[33] A. Cervera-Villanueva, Nucl. Instr. and Meth. A447 (2000) 100.

[34] A. Cervera-Villanueva *et al.*, *Survey of the Frames for STAR*, NOMAD Internal Note, NOMAD-MEMO-97-48, 18 December 1997.

[35] J. Altegoer *et al.*, Nucl. Instr. and Meth. A428 (1999) 299.

[36] F.J.P. Soler, "Silicon Detectors for Neutrino Physics Experiments", 5th International Conference on Position Sensitive Detectors, University College, London, September 1999. To be published in Nuclear Instruments and Methods.

[37] H. Georgi and H. D. Politzer, *Phys. Rev.* **D14**, (1976) 1829.

[38] D.H.Perkins, *Introduction to High Energy Physics*, Addison-Wesley Publishing Company (1987).

[39] J. Altegoer et al. *NOMAD GEANT Offline Manual.* CERN, 5.11 edition, 1996.

[40] M. Goossens et al. *GEANT Detector description and simulation tool.* CERN, 1994.

[41] G. Ingelman. LEPTO version 6.1 — the Lund Monte Carlo for deep inelastic lepton-nucleon scattering. In W. Buchmüller and G. Ingelman, editors, *Physics at HERA*, pages 1366–1394, Hamburg, 1992. DESY.

[42] Torbjörn Sjöstrand. PYTHIA 5.7 and JETSET 7.4: Physics and manual. Technical Report CERN-TH.7112/93, CERN, 1994.

[43] J.P. Meyer and A. Rubbia. *NOMAD event generator offline manual.* CERN, 5.00 edition, 1994.

[44] D. Daniels and E. Tsesmelis, *NUBEAM Documentation*, NOMAD Internal Note (19 96).

[45] J. Altegoer et al. Search for a new gauge boson in $\pi^0$ decays. *Physics Letters B*, 428:197–205, 1998b.

[46] T. Weiße. *Comparison of Muonic and Electronic Final States in the NOMAD Experiment at the CERN Wide-band Neutrino Beam.* PhD thesis, Universität Dortmund, 1997.

[47] D. Steele. *A Search for Neutral, Heavy Particles Decaying to a Neutrino and a Single Photon at the SPS Wide-Band Neutrino Beam.* PhD thesis, Johns Hopkins University, Baltimore, 1996.

[48] Kevin Varvell. NOMAD DST package - version v7r2. NOMAD Memo 97-034. The v7r3 version of the documentation, and other relevant information, is available from the URL `http://pauli.physics.usyd.edu.au/Public/dst/dst.html`, 1997.

[49] J. Kokkonen, F.J.P. Soler, G. Vidal Sitjes. STAR Noise and Hit-Finding Efficiency. NOMAD Memo 2000-06.

[50] F. Juget D*+ identification in numuCC charged current interactions. NOMAD Memo 2000-03.

[51] Y. Fukuda *et al.* [Super-Kamiokande Collaboration], Phys. Rev. Lett. **81**, 1562 (1998) [hep-ex/9807003].

[52] A. Benvenuti *et al.*, *Phys. Rev. Lett.* **34**, (1975) 538.

[53] B. Strongin *et al.*, *Phys. Rev.* **D 43**, (1991) 2778.

[54] H. Abramowicz *et al.*, *Z. Phys.* **C15**, (1982) 19.

[55] A.O.Bazarko *et al.*, *Z. Phys.* **C65**, (1995) 189.

[56] N.J.Baker *et al.*, *Phys. Rev.* **D 43**, (1991) 2765.

[57] V. Jain *et al.*, *Phys. Rev.* **D 41**, (1990) 2057.

[58] N. Ushida *et al.*, *Phys. Lett.* **B 121**, (1983) 287.

[59] J. M. Vieira, *Production de quarks charmés et détermination de la mer étrange de quarks dans l'expérience NOMAD*, Ph.D Thesis, Université de Lausanne (1998).

[60] G. Bassompierre et al. A Large Area Transition Radiation Detector for the NOMAD experiment. *Nucl. Instr. and Meth. in Phys. Res. A*, 403: 363, 1998.

[61] G. Bassompierre et al. Performance of the NOMAD Transition Radiation Detector. *Nucl. Instr. and Meth. in Phys. Res. A*, 411:63, 1998.

[62] D. Autiero et al Test beam Performance of the Electromagnetic Calorimeter of the NOMAD Experiment. *Nucl. Instr. and Meth. in Phys. Res. A*, 387:352, 1997.

[63] J. Altegoer *et al.* The Trigger system of the NOMAD experiment. *Nucl. Instr. and Meth. in Phys. Res. A*, 428:299, 1999.

[64] N. Ushida *et al.*, Production characteristics of charmed particles in neutrino interactions. *Phys. Lett.*, **B 206**, (1988) 380

[65] N. Ushida *et al.*, Cross-sections for neutrino production of charmed particles. *Phys. Lett.*, **B 206**, (1988) 375

[66] K. S. McFarland, Short-baseline opportunities and challenges at a neutrino factory. *Nucl. Instr. and Meth. in Phys. Res. A*, 451:218, 2000.